Automated Ultrasound In-process NDE of Wire + Arc Additive Manufacture

Rastislav Zimermann

Department of Electronic and Electrical Engineering

Centre for Ultrasonic Engineering

University of Strathclyde

A thesis submitted for the degree of

Doctor of Philosophy

May 2022

Copyright

This thesis is the result of the author's original research. It has been composed by the author and has not been previously submitted for the examination which has led to the award of a degree.

The copyright of this thesis belongs to the author under the terms of the United Kingdom Copyright Acts as qualified by the University of Strathclyde Regulation 3.50. The due acknowledgment must always be made of the use of any material contained in, or derived from, this thesis.

Signed: 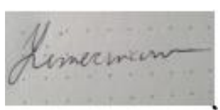

Date: April 2022

Acknowledgements

First of all, I would like to thank my supervisors Dr. Charles MacLeod and Dr. Ehsan Mohseni for supporting and encouraging me throughout this journey. Their help, mentorship and positive attitude along my journey have been invaluable. Furthermore, I'd want to express my gratitude to Professor Stephen Gareth Pierce for his unwavering support over the past four years, ensuring that the research work proceeded as smoothly as possible.

I would like to express my sincere thanks to my partner, Zuzana, for supporting me during my student life as both an undergraduate and Ph.D. student. My academic and professional success would be incredibly tough if she did not stand by me for all these years.

I would also like to express my gratitude to my family, particularly my parents Slavka and Rastislav, who have been supporting and pushing me to pursue technical courses since I was a youngster, and whose positive attitude toward my aspirations and interests has enabled me to become a successful researcher.

Abstract

The global metal Additive Manufacturing (AM) market was valued at € 2.02 billion in 2019 and is expected to increase at a rate of up to 27.9% annually until 2024. In the latest industrial revolution, Industry 4.0, where smart factories capable of creating high-quality customized items at a low cost are in high demand, AM technology plays a key role. This demand can be satisfied by research of metal AM techniques such as Wire + Arc Additive Manufacturing (WAAM). WAAM utilizes industrial robotics and arc-based welding processes to produce components on a layer-by-layer basis. This enables automated, time and material-efficient production of high-value and geometrically complex metal parts. To strengthen these benefits, the demand for robotically deployed in-process Non-Destructive Evaluation (NDE) has risen, intending to eventually replace convectional manually deployed inspection procedures after the whole part completion.

This thesis presents novel research that contributes to the field of automated in-process inspection of as-built WAAM components. By deployment of a novel automated high-temperature dry-coupled ultrasound roller-probe, the challenges of coupling to an as-built WAAM in-process, are solved. However, the inspection approach lacks suitable imaging techniques to accommodate for multiple refractions through unknown arbitrary interfaces. Therefore, in this thesis, a novel Synthetic Aperture Focusing Technique (SAFT) based surface finding linked to the three-layer adaptive Total Focusing Method (TFM) package is developed to process the acquired ultrasound Full Raw Data (FRD) called Full Matrix Capture (FMC). The developed system is then deployed in-process, delivering, for the first

time, ultrasound in-process inspection of as-built titanium WAAM components. Lastly, realizing the drawbacks limiting the NDE deployment, the advanced FRD technique, called Virtual Source Aperture (VSA), is linked to the SAFT-TFM imaging package to increase the maximum inspection speed, reduce the size of the data and increase the energy levels retrieved from the sample.

Contents

List of Figures

List of Tables

Abbreviations

3D	Three-dimensional
AM	Additive manufacturing
BDH	Bottom-Drilled Holes
CPU	Central Processing Unit
DAS	Delay-And-Sum
DeD	Directed-energy Deposition
DoF	Degrees of Freedom
ECT	Eddy Current Testing
FMC	Full Matrix Capture
FRD	Full Raw Data
FT	Force-Torque
GMAW	Gas Metal Arc Welding
GPU	Graphical Processing Unit
GTAW	Gas Tungsten Arc Welding
GUI	Graphical User Interface

HVM	High Value Manufacturing
IR	Inspection Robot
KRC	KUKA Robot Controller
LIPA	Laser Induced Phased Arrays
LMD	Laser Metal Deposition
LoF	Lack of Fusion
NDE	Non-Destructive Evaluation
NDT	Non-Destructive Testing
PAUT	Phased Array Ultrasound Transducers
PAW	Plasma Arc Welding
RSI	Robot System Interface
SAFT	Synthetic Aperture Focusing Technique
SNR	Signal-to-Noise Ratio
TFM	Total Focusing Method
ToF	Time of Flight
UT	Ultrasound Testing
VS	Virtual Source

VSA	Virtual Source Aperture
WAAM	Wire + Arc Additive Manufacturing
XCT	X-ray Computed Tomography

Chapter 1

Introduction

1.1. Context of Research

In 2019, the global metal Additive Manufacturing (AM) market size was valued at an estimated 2.02 billion € and was forecasted to expand by up to 27.9% annually until 2024 [1]. AM technology plays a significant role in the ongoing industrial revolution, Industry 4.0, where there exists a demand for smart and flexible production lines effective in fabricating high-quality customized components [2].

Such a one AM technology, called Wire + Arc Additive Manufacturing (WAAM), is a fast-emerging metal AM technology, based on a directed energy deposition process [3], which pledges to achieve automated fabrication of geometrically complicated three-dimensional (3D) near-net shaped components [4]. WAAM has attracted the attention of industries such as aerospace, defense, and transportation due to the promise to deliver cost-effectiveness achieved by reduced material waste and energy consumption, decreased production time and increased design flexibility when producing large and geometrically complex components [4].

A clear example has been demonstrated, where the [4] has reported a material saving of approximately 220 kg to manufacture a 24 kg titanium Ti-6AL-4V landing gear assembly with a deposition speed of 0.8kg/hour. In this instance, the landing gear geometry consisted of complex features such as tiled walls and T-junctions, proving the technique as a reliable alternative for convectional subtractive techniques, where the time taken for milling operations and waste would make the process extremely inefficient [5].

WAAM components are typically produced using automated positioning platforms, eg. robotic arms or gantries, featuring an electric arc welder employed as a heat source, to which the feedstock is fed similarly to robotic welding [4, 5]. The component geometry is mainly a series of deposited walls with parallel or single oscillating beads [6]. When depositing materials that could suffer from oxidation and subsequently induced defects during deposition, additional shielding is deployed. In [8], WAAM deposition of large titanium components was enabled through the deployment of a local shielding device that supplied the build area with shielding gas, such as argon or helium, and reduced the potential for contamination. Alternatively, WAAM deposition utilizes tent-like structures, fully enclosing the deposition apparatus and filled with shielding gas to avoid the component's contact with oxygen [7].

Despite, the shielding system protecting the molten pool from oxidation, reducing the potential for porosity and inclusions, like many welding processes, for example Lack of Fusion (LoF) and keyholes defects may be generated between the layers, diminishing the structural integrity and fitness-for-service of the part [8]. These undesired deposition flaws predominantly originate from the mediocre quality of the wire, inappropriate definition of the production parameters, and contamination introduced by the environment [4]. Thus, it is a vital step to assure the integrity of WAAM components through Non-Destructive Evaluation (NDE) before they can be certified and enter their aimed service application.

NDE has an important role in ensuring the quality and fitness-for-purpose of components, especially, in safety-critical industries such as aerospace or transportation where a failure of the component can cause a catastrophe [9]. The current NDE of WAAM is traditionally carried out separately after the full component competition and often after full or partial machining of the part [10-12]. In case of a flaw discovery within the built volume, the part is either scrapped or sent back for extensive and time-consuming repair. Thus, the production process suffers from a bottleneck caused by the time inefficiency of the NDE which results in low production throughput and overall decreased competitiveness of the WAAM process as a whole.

The opportunity exists to perform layer-specific volumetric NDE in-situ just after the deposition is finished or when the robot is depositing elsewhere. This can be accomplished by an automatically deployed and flexible NDE approach, which can detect defects at the point of their creation or when the inspection is due in service [13]. By integrating a novel ultrasound-based NDE roller-probe into the manufacturing process, the early detection of the defects can be made possible, enabling early in-process repair or scrappage of the part [14]. This is especially important given that only a little amount of material would be required to be removed or scrapped since the component is created on a layer-by-layer basis. Moreover, the automated NDE systems would remove the safety concerns, as they can be deployed under hazardous conditions where human access is not permitted [15]. A further advantage of the in-process NDE can be realized by the simplified production time estimation which is a result of a highly integrated and smart manufacturing system.

1.2. Problem Statement

Wire + Arc Additive Manufacturing is a rapidly growing sector of automated part production; however, the deployment is limited by a lack of suitable NDE approaches that would replace traditional, often manual, NDE. Despite the recent automation advancement in in-process ultrasound NDE deployed on welding [13, 16, 17], the ultrasound NDE of WAAM components is still conducted after the full deposition either through a machined surface using contact ultrasound transducers or in immersion using a gantry. This is a limiting factor considering a potential full scrappage or expensive re-work is required if a defect is detected.

The automation and integration of ultrasound NDE into the WAAM process can significantly shorten the time between the defect formation and its detection and could be further proposed for industrial application.

However, the deployment of the conventional ultrasound sensor, in-process, faces challenges caused by the WAAM surface temperatures (above 150 °C) just after the deposition, where the convectional ultrasound array can only sustain up to 60 °C, while commercial delay lines can push this limit only up to around 150°C for a limited period

[18]. Further, the transducer coupling with an as-built nonflat surface, featured by WAAM, creates another challenge. Commercial arrays are designed fixed solidly (flat or curved with a fixed radius) in the case which makes them non-adaptable to the surface of the geometrically complex components such as WAAM. Therefore, an alternative approach capable of accommodating continuous transmission of the ultrasound wave into the component at speed is highly desirable.

Novel dry-coupled ultrasound WAAM roller-probes can accommodate uneven and hot coupling conditions at speed. However, the ultrasound refraction at the interface between internal components (Delay line/ rubber tyre) and the interface between the rubber tyre/WAAM must be accounted for. Convectional data acquisition techniques such as Full Matrix Capture (FMC), offer great potential to overcome the challenges associated with coupling through interfaces present between the components of the novel roller-probe as well as the unknown non-flat interface of WAAM. However, a gap exists in the lack of research investigating suitable post-processing algorithms that can subsequently compensate for unknown non-flat surfaces and the refraction occurring on multiple interfaces intercepting the ultrasound wave propagation path.

Further, the FMC's drawbacks can be realized by large data size, low emitted ultrasound energy due to single element excitation, and subsequently lower scanning speeds associated with many sequential element firings required for a single frame of data. Therefore, the deployment of alternative advanced Full Raw Data (FRD) techniques, such as virtual sources, is desired. By utilizing such FRD techniques, the reduction in data size, increase in inspection speed and higher energy level at reception can be achieved. All without sacrificing the sensitivity to the defects. However, these have not yet been investigated for WAAM roller-probe applications.

1.3. Research Goals

Based on the aforementioned problem statement, the research goals of the work in this thesis are:

1. Review the NDE techniques evaluated on metallic additive manufacture components and establish the state-of-the-art in the field of in-situ ultrasound WAAM NDE.
2. Present the concept of in-process dry-coupled high-temperature WAAM roller-probe for inspection of components through an as-built surface.
3. Develop an ultrasound post-processing algorithm package for novel roller-probe inspection of as-built WAAM components accommodating for the unknown surface of WAAM and ultrasound refraction at multiple interfaces.
4. Design a multi-robot cell for automated sensor-enabled and in-process NDE of WAAM components.
5. For the first time, demonstrate the in-process ultrasound NDE of as-built WAAM using a dry-coupled high-temperature WAAM roller-probe.
6. Adopt, optimize and investigate the alternative data acquisition technique to increase the speed of inspection and reduce the data size all while not compromising on ultrasound imaging performance.

1.4. Contribution to Knowledge

This thesis presents the following novel contribution to the fields of automated and in-process NDE of metal AM components using ultrasound as follows:

1. Utilizing a data acquisition technique called, Full Matrix Capture, a novel Synthetic Aperture Focusing Technique (SAFT) based surface reconstruction of the roller-probe/WAAM interface is developed and presented.
2. The Total Focusing Method (TFM) imaging algorithm is developed for the UT ray-tracing through 3 media with the second interface being arbitrary, which enabled the formation of a fully focused WAAM interior.
3. A novel concept of the multi-robot cell for WAAM and NDE is presented where the plasma-arc welding process was used to build components while automated sensor-driven dry-coupled NDE was conducted via an as-built WAAM surface using a novel phased array WAAM roller-probe.
4. For the first time, the in-process NDE is demonstrated on titanium WAAM wall with embedded artificial reflectors, enabling the possibility to detect defects just after their creation which opens the door to the possibility of local in-process repair integration in the future.
5. The advanced ultrasound data acquisition technique, called Virtual Source Aperture, is adopted and optimized for the roller-probe WAAM inspection using the SAFT-TFM package showing a possibility to reduce the size of the data and increase the inspection speed without compromising on interior imaging

performance. Increased signal strength at the reception and the imaging stage is achieved as well.

6. The work presented in this thesis has directly supported research programs, with the aim to produce right-first-time WAAM components – NEWAM and RoboWAAM projects.

1.5. Thesis Structure

In this thesis, Chapter 2 introduces and presents the theoretical background, upon which the research is built. The background into WAAM is given, explaining the process, and stating the common defects this thesis is aiming to inspect. Further, the literature review into the NDT&E techniques evaluated on metallic additive manufacture components is presented, aiming to justify the chosen research direction. The fundamentals of Ultrasound Testing (UT) and its relationship to automation are also presented. The literature review is summarized by an introduction of a novel dry-coupled high-temperature WAAM roller-probe which is the subject of deployment in this thesis.

Chapter 3 presents a concept of the Synthetic Aperture Focusing Technique & Total Focusing Method (SAFT & TFM) package developed for the roller-probe inspection of as-built WAAM components featuring arbitrary interface. The development is evaluated on two WAAM samples with artificial and intentionally induced defects.

The research presented in Chapter 4 introduces an architecture of the multi-robot WAAM & NDE cell featuring a plasma arc welding process and sensor-enabled automated ultrasound inspection using a dry-coupled roller-probe. Moreover, for the first time, the ultrasound in-process NDE of WAAM is presented and its performance evaluated.

Chapter 5 explores an alternative acquisition technique called, Virtual Source Aperture, which is adapted for the roller-probe inspection using the SAFT-TFM package, and its performance is evaluated by an inspection modeling and an experimental inspection of the custom-designed WAAM calibration sample. Further, the technique is evaluated by inspection of an as-built WAAM component with artificial reflectors. The advantages of this acquisition approach is summarized in a hypothetical WAAM in-process inspection scenario.

Lastly, Chapter 6 summarizes the research undertaken throughout this thesis and introduces future developments and directions where this research can lead to.

1.6. Publications as Lead Author

1.6.1. Journal Papers

- Zimermann, Ehsan Mohseni, David Lines, Randika KW Vithanage, Charles N MacLeod, Stephen G Pierce, Anthony Gachagan, Yashar Javadi, Stewart Williams, Jialuo Ding, Multi-layer imaging of as-built Wire+Arc Additive Manufactured components, 2021, Additive Manufacturing, Volume 48, Elsevier

- Rastislav Zimermann, Ehsan Mohseni, Randika KW Vithanage, David Lines, Euan Foster, Charles N. Macleod, S. Gareth Pierce, Gianrocco Marinelli, Stewart Williams, Jialuo Ding, *Increasing the speed of automated ultrasonic inspection* *of as-built WAAM components by the adoption of Virtual Source Aperture*, 2022, Materials & Design, Elsevier - Under review (April 2022)

- Rastislav Zimermann, Ehsan Mohseni, Momchil Vasilev, Charalampos Loukas, Randika KW Vithanage, Charles Macleod, David Lines, Misael Pimentel, Stephen Fitzpatrick, Steven Halavage, Scott McKegney, Gareth Pierce, Stewart Williams, Jialuo Ding, *Multi-Robot cell for wire + arc additive manufacture and sensor-enabled in-process ultrasound non-destructive evaluation*, Sensors, MDPI, - Under review (April 2022)

1.6.2. Conference contribution

- R. Zimermann, E. Mohseni, Randika KW Vithanage, D. Lines, C. N. MacLeod, S. G. Pierce, A. Gachagan, *Implementation of Ultrasonic Total Focusing Method for multi-interface inspection of components with non-planar surfaces manufactured using Wire+Arc Additive Manufacture,* Scottish Ultrasound 2020, Glasgow, UK

- R. Zimermann, E. Mohseni, Randika KW Vithanage, D. Lines, C. N. Macleod, S. G. Pierce1, A. Gachagan, S. Williams, J. Ding2, M. Gianrocco, *Implementation of an ultrasonic Total Focusing Method for inspection of unmachined Wire+Arc Additive Manufacturing components through multiple interfaces*, 2020 ASME Quantitative Nondestructive Evaluation QNDE2020, Minneapolis, MN, USA

- R. Zimermann, E. Mohseni, Randika KW Vithanage, D. Lines, C. N. Macleod, S. G. Pierce1, A. Gachagan, S. Williams, J. Ding, *Optimization of Virtual Source Aperture Imaging for Dry-Coupled Roller-Probe Inspection of As-Built WAAM components*, 2021 ASME Quantitative Nondestructive Evaluation QNDE2021, Online

1.7. Publications as a Co-Author

1.7.1. Journal Papers

- Ehsan Mohseni, Charles Macleod, Yashar Javadi, Randika KW Vithanage, Zhen Qiu, David Lines, Euan Foster, Peter Lukacs, Momchil Vasilev, Rastislav Zimermann, S Gareth Pierce, Anthony Gachagan, *A model-based study of transmit-receive longitudinal arrays for inspection of subsurface defects,* 2020/8/1, Journal of Nondestructive Evaluation, Diagnostics and Prognostics of Engineering Systems

- David I Lines, Yashar Javadi, Ehsan Mohseni, Momchil Vasilev, Charles N MacLeod, Carmelo Mineo, Randika KW Vithanage, Zhen Qiu, Rastislav Zimermann, Charalampos Loukas, Euan Foster, SG Pierce, Anthony Gachagan, *A flexible robotic cell for in-process inspection of multi-pass welds*, 2020/9/1, Insight-Non-Destructive Testing and Condition Monitoring

1.4.2. Conference Contribution

- Ehsan Mohseni, Yashar Javadi, David Lines, Randika KW Vithanage, Euan Foster, Zhen Qiu, Rastislav Zimermann, Charles Norman MacLeod, Stephen Pierce, Anthony Gachagan, Gianrocco Marinelli, Jialuo Ding, Stewart Williams, U*ltrasonic phased array inspection of wire plus arc additive manufactured (WAAM) titanium samples*, *2019*, 58th Annual British Conference on Non-Destructive Testing

- Yashar Javadi, Charles Macleod, David Lines, Momchil Vasilev, Ehsan Mohseni, Euan Foster, Zhen Qiu, Randika KW Vithanage, Rastislav Zimermann, Charalampos Loukas, Gareth Pierce, Anthony Gachagan, *In-process inspection of multi-pass robotic welding*, 2019, Review of Progress in Quantitative Nondestructive Evaluation

- Charles Macleod, Zhen Qiu, Ehsan Mohseni, Randika KW Vithanage, Yashar Javadi, Rastislav Zimermann, Momchil Vasilev, David Lines, Gareth Pierce, Anthony Gachagan, Stewart Williams, Jialou Ding, Filomeno Martina, *Dry Coupled automated inspection for wire+arc additive manufacture*, *2019*, Review of Progress in Quantitative Nondestructive Evaluation

- David Lines, Ehsan Mohseni, Rastislav Zimermann, Carmelo Mineo, Charles Norman MacLeod, Gareth Pierce, Anthony Gachagan, *Modelling of Echo amplitude fidelity for transducer bandwidth and TFM pixel resolution*, 2020, 47th Annual Review of Progress in Quantitative Nondestructive Evaluation

- Ehsan Mohseni, Randika KW Vithanage, Zhen Qiu, Yashar Javadi, Momchil Vasilev, Charles N MacLeod, David Lines, Rastislav Zimermann, Stephen G Pierce, Anthony Gachagan, Jialuo Ding, Stewart Williams, *Laser-assisted surface adaptive ultrasound (SAUL) inspection of samples with complex surface profiles using a phased array roller-probe*, 2020, 59th Annual British Conference on Non-Destructive Testing

- Ehsan Mohseni, Randika KW Vithanage, Zhen Qiu, Charles Norman MacLeod, Yashar Javadi, David Lines, Rastislav Zimermann, Gareth Pierce, Anthony Gachagan, Jialuo Ding, Stewart Williams, *A high temperature phased array ultrasonic roller probe designed for dry-coupled in-process inspection of wire+arc additive manufacturing*, 2020, 47th Annual Review of Progress in Quantitative Nondestructive Evaluation

Chapter 2

Research Background

2.1. Metal Additive Manufacturing

AM is a manufacturing process using which components are produced from 3D model data on a layer upon layer basis [19]. Metal AM is becoming a suitable substitute for traditional manufacturing methods where components are either subtracted by milling processes or formed in molds [20]. Moreover, AM enables an option to produce complex components that would otherwise be assembled from multiple sub-components.

Fundamentally, metal AM components are produced by an energy source melting either wire or powder-based feedstock. Powder bed fusion processes such as laser beam melting, or electron beam melting are used to build components in closed chambers by fusing the powder to create a layer of the final structure. The bed, on which the layer is deposited, is then lowered and the process is repeated until the full component is completed. Such processes are typically utilized to produce parts with high geometric precision, however, the process is traditionally time-consuming and the parts produced are predominantly small [21-23].

To produce geometrically large-scale components, e.g. on the order of meters, research has focused on the development of Directed-energy Deposition (DeD) processes, such as Laser Metal Deposition (LMD) or Wire+Arc Additive Manufacturing (WAAM), where a laser, an electron beam or an electric arc is employed to produce a melt pool into which the wire or a powder feedstock is delivered to produce a bead or layer. The dimensional accuracy of these processes is often traded for the increased size of the final component and the deposition rate [4, 24, 25].

2.2. WAAM

2.2.1. Process of WAAM

WAAM is an AM technique that has received significant interest in research and industry over the past decades, despite the fact, that the first patent was filed in 1925 [4]. The process utilizes industrial robotics and arc-based heat input, commonly off-the-shelf welding equipment, to melt a wire feedstock into a desired shape and height. Hence, this combination enables the production of medium to large, near net-shaped components featuring complex geometrical features, such as the as-built component [26], seen in Figure 2.1(a).

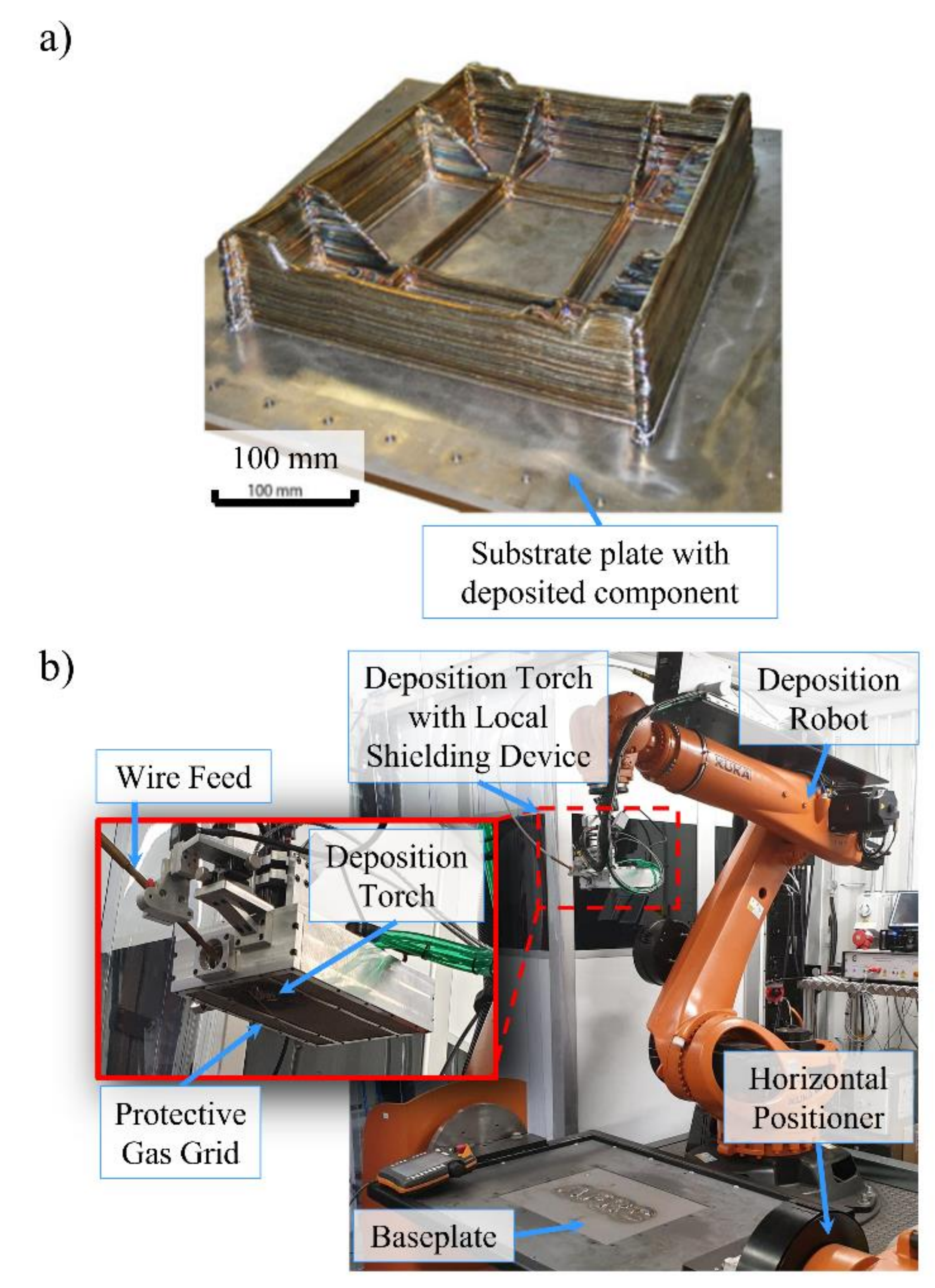

Figure 2.1 WAAM landing gear rib component, and (b) WAAM robotic deposition setup based in Light Weight Manufacturing centre (Renfrew, UK)

2.2.1.1. Processes & Materials

Common welding processes found to be employed in WAAM include Gas Metal Arc Welding (GMAW), Gas Tungsten Arc Welding (GTAW) or Plasma Arc Welding (PAW), where the process is selected based on the application [1]. For Example, (GMAW) is primarily used for high deposition rates while GTAW or PAW are used for higher precision parts [27].

Due to the laboratory availability of the process, much of the work in this thesis has been associated with the PAW process. PAW enables higher energy density causing lower distortion of welds while achieving smaller beads and higher speeds [28].

The PAW – WAAM process is depicted in Figure 2.1(b) where the arc is formed by an electrode positioned higher in the body of the torch. The plasma then exits through the nozzle of the torch as illustrated in Figure 2.2. The wire is then fed into the melt pool externally via a wire feeder [29]. The shielding gas, typically argon or helium is forced on the weld pool to protect the bead from oxidation. Since oxidation can occur after the solidification of some materials, the gas is also supplied to protect the WAAM components by either a local shielding device or a tent-like structure enclosing the whole setup [30, 31].

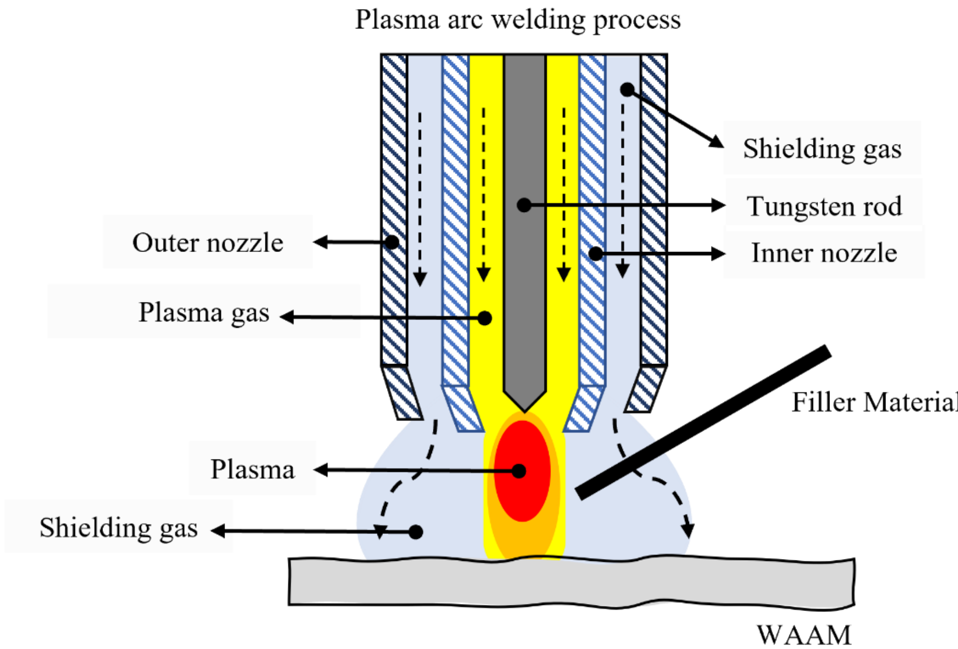

Figure 2.2 Illustration of the PAW process

Metals used in the WAAM process are often commercially available wires produced for the welding industry [8]. The Titanium alloys, used throughout this thesis, have been extensively researched for sectors such as aerospace due to their high strength-to-weight ratio. It is noteworthy, that these alloys suffered from high costs when combined with traditional subtractive manufacturing methods[4]. Further materials studied for WAAM application include aluminium alloys, and steel or nickel-based superalloys [8].

2.2.1.2. WAAM Process

During the WAAM process, the beads are commonly deposited on a substrate plate into desired shapes and heights using an industrial axial manipulator, such as gantry systems or robotic arms. Figure 2.3 shows a WAAM process diagram, where at first, the paths are automatically generated from the 3D model of the component. Subsequently, the deposition parameters, such as wire feed speed, and current or robot deposition speed, are set by an operator. The software, then, generates the files containing information about the deposition trajectory, robot speed or welder on/off command. This stage is followed by a deposition process, which is typically initiated by a dry run to make sure the robot moves as desired without any collisions with the environment. Once the deposition of the near-net-shape component is completed, the part is machined into a final size by removing the excess material accumulated on the edges of the walls. Smaller features, such as threaded holes, chamfers or rounds are produced at this stage as well. Lastly, the components are quality assured and sent into service.

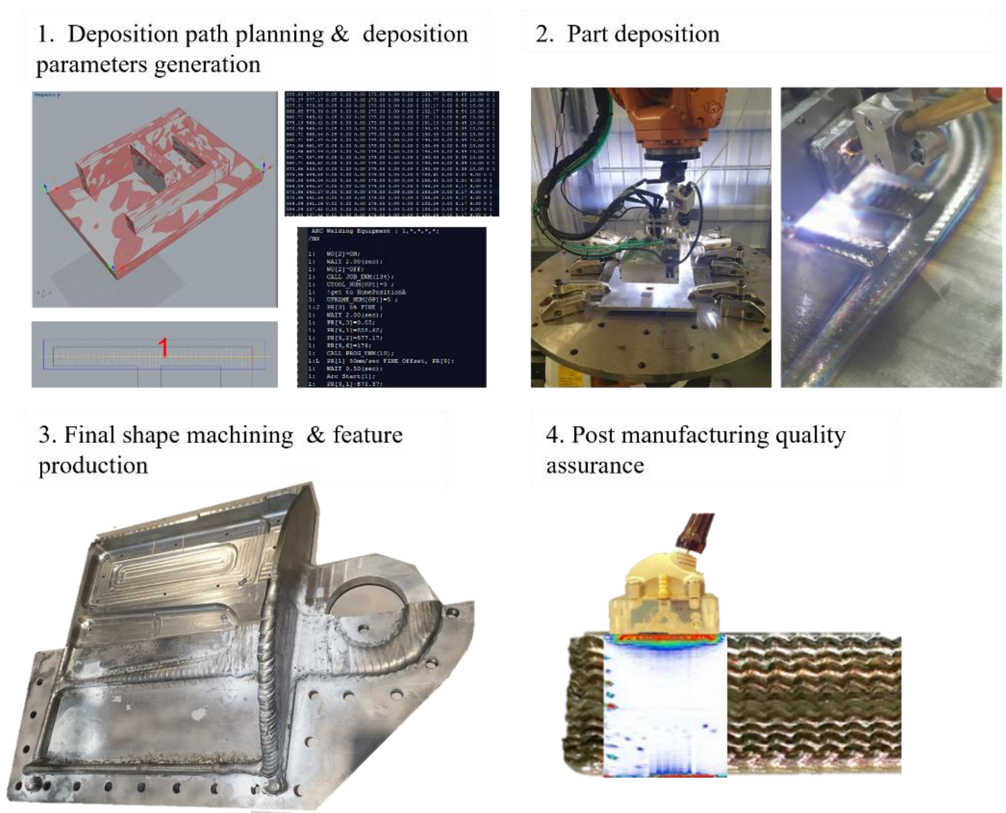

Figure 2.3 Diagram showing a typical process of WAAM component production

2.2.2. Defects Occurring in WAAM Process

Although the shielding system protects the molten pool from oxidation which reduces the potential for the creation of porosity and inclusions, similar to many welding or manufacturing processes, defects such as Lack of Fusion (LoF) or keyhole defects, as seen in Figure 2.4, may occur in the components affecting the structural integrity and fitness for service [8]. These undesirable deposition defects, predominantly originate from poor quality wire, incorrect definition of the process parameters and contamination introduced by the environment [4]. Moreover, delamination defects can be caused by insufficient remelting of the previous layer during the subsequent deposition. Cracks can also be created within the WAAM component, either by unfavourable solidification conditions or at grain boundaries due to morphology differences [8].

In light of the aforementioned flaws common for WAAM, it is essential to assess the quality and integrity of manufactured components through Non-Destructive Evaluation (NDE) before they can be certified and enter their intended service application. Further, the detection of defects can enable repair of the built or scrap the part in case repair is no longer viable.

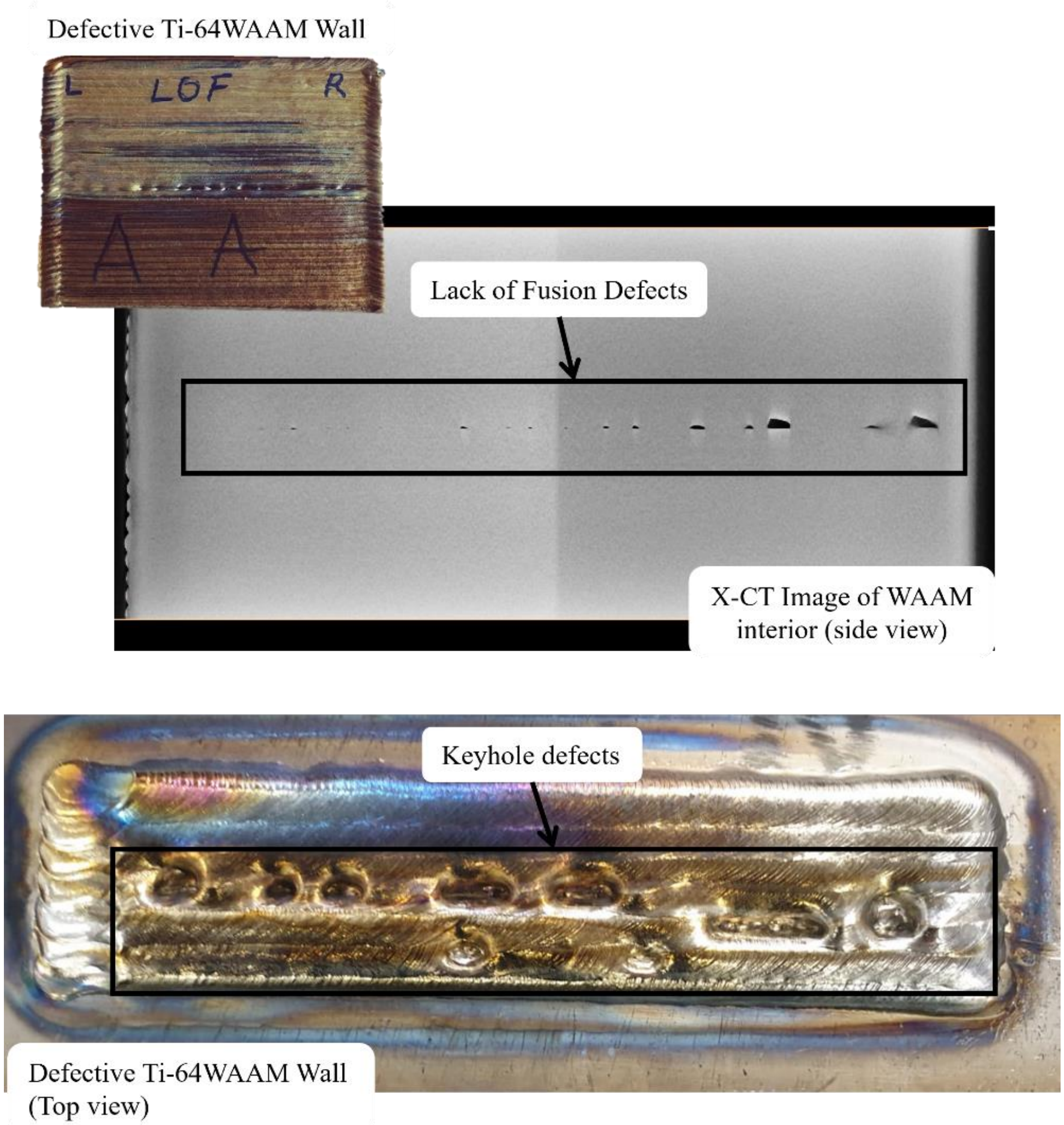

Figure 2.4 WAAM defects

2.3. NDE of Additive Manufactured Components

2.3.1. Mapping NDE Techniques Evaluated on Metal AM Components

Non-Destructive Testing (NDT) is the name for a group of methods and techniques that enable the assessment of the structural integrity of components without affecting the fitness-for-service of the part. If a defect is discovered, NDE focuses on the characterization of the defect by investigating its size, location and nature to help decide on acceptance or rejection and whether the final component qualifies for service [9]. This section aims to introduce various NDT techniques that have been used and evaluated for the detection and characterization of internal defects within the metal components manufactured using AM techniques.

X-ray imaging techniques such as radiography have already been successfully deployed and the performance evaluated on AM, achieving detection of porosities, inclusions, and lack of fusion defects in fully-built WAAM components [10]. X-ray testing is based on X-radiation being excited by a source, transmitted through the test piece and captured by an analog or digital photosensitive reception medium. The image is, therefore, formed by displaying inconsistencies of the penetrated energy caused by density discontinuities within the part. The application of this technique has a significant disadvantage of low time efficiency, high cost and it is a potential hazard to a human operator [32].

A more advanced X-ray-based technique is called X-ray Computed Tomography (XCT) and it has also been associated with NDE of AM components. In XCT, normally a series of X-ray images are taken from a large set of different angles surrounding a test object, after which, an interior visualization in form of a 3D model is constructed via computing the amount of X-ray exposure of constituent cubic elements of the 3D volume [33]. The technique demonstrated high sensitivity to detect and the ability to characterize defects deep within AM components, without the need for surface pre-processing. Detection of defects as small as 0.6 mm in titanium components produced using electron beam techniques has been demonstrated [34]. The technique has significant downsides associated with the high-cost equipment needed to test the component and analyze the data, along with a space requirement making it impractical to be implemented for in-situ or in-process inspection of WAAM [35].

Further, Eddy Current Testing (ECT) is an electromagnetic-based inspection technique where the current flows in closed loops within the conductor, in planes perpendicular to the magnetic field. The shape of the loop is dependent on the shape of the conductor. The currents are generated in a conductive material by a coil connected to a current generator. The defects within a tested volume are then highlighted on an image as perturbations in the current flow [36].

For example, ECT was shown to be capable of detecting side-drilled holes of 0.35 mm at the depth of 2 mm below the surface and 3 mm at the depth of 5 mm below the surface within the aluminum WAAM sample [37]. This was achieved by a customized spatial coil design, with a shape matched to the as-built curved surface of a WAAM component.

Despite the high surface/near-surface sensitivity of the ECT, the limiting factor for deployment, as compared to for example ultrasound, is the penetration depth which is often in the order of a few millimeters. This phenomenon responsible for the decreased penetration depth is called the skin effect, and it is created by the magnetic field opposing the primary field which decreases the magnetic flux [38]. The penetration depth is also constrained by variables such as coil design, test frequency or test-piece material properties [36]. Further, it may not be possible to detect subsurface defects when inspecting materials such as ferromagnetic steel, due to extreme loss of penetration depth due to high permeability[39]. Hence defects such on locations such as interlayer bonds in WAAM (Lack of Fusion defects) may remain undiscovered.

Therefore, while it offers a great potential for the NDE of freshly deposited layers [10], it is not well-suited for deeper volumetric inspection of WAAM components and multi-layers, or the in-process inspection of preceding layers for defects such as delayed cracking [40, 41].

Among other NDE methods deployed for the AM inspection, thermography has also been considered and utilized to inspect for defects [34]. The hardware was located at a safe distance, at least 60 cm from the sample, searching for thermal variations indicating the flaws in the AM component [42]. This technique, however, suffers from low detection sensitivity below the surface caused by the roughness and also may require an external heat input to induce heat into the specimen, which can be time-consuming and not practical in a busy environment [43].

Conventional Ultrasound Testing (UT) or modern phased array technology is often the preferred inspection technique for volumetric examination of metallic welded components [44]. This inspection method offers high sensitivity to small defects (approximately a fraction of a millimeter) and is capable of pinpointing, characterizing, and sizing different shapes and orientations of voids within the part [45]. Additionally, considering the advances in phased array technology, signal processing, and robotics, the technique is feasible to integrate within automated robotic systems for the inspection of welds and AM components efficiently and safely [13, 46]. Typically, in weld inspection, angled wedges mounted alongside the joint on the parent material, are normally required to guide the wave towards the weld at a certain defined angle or the emerging use of novel conformable liquid-filled delay lines allows inspection directly on top of the filled weld cap [13].

Laser ultrasound, as another method of generating ultrasonic waves, is a non-contact method capable of detecting subsurface defects as small as 0.2 mm in diameter in aluminum AM components produced using laser powder bed fusion [47] and on WAAM components detecting surface cracks, flat bottom holes and through holes [48]. However, laser ultrasonic setups have historically featured very high initial costs, slow generation, acquisition, and data processing times, while also being sensitive to surface finish [49] and having safety considerations.

Lastly, the deployment of gas or air-coupled UT is inherently limited by the large acoustic impedance mismatch between the air and solid inspection medium, resulting in a large loss of energy (< 140 dB) and hence sensitivity, therefore not endearing this method for the inspection of AM components [50].

Considering the capabilities of NDE techniques previously trialed on AM components and summarized above, ultrasonic techniques offer strong potential for in-situ as-built WAAM volumetric inspection and therefore are the core research subject of this thesis. However, challenges remain related to suitable coupling between the ultrasound probe and the potentially hot as-built WAAM surface, along with imaging of the component through the irregular non-planar as-built surface.

2.4. Fundamentals of Ultrasonic Testing

Portability of equipment, low cost, non-hazardous operation, and high accuracy of ultrasonic have made this technique well-established for NDE of processes such as welding [51] and more recently additive manufacturing, especially WAAM [10, 52, 53]. The ultrasonic wave is considered typically above the frequency of 20 kHz and is used in many applications including medical imaging and surgery (sonography) [54], automotive ultrasonic sensors (car parking sensors) [55] or accelerating chemical processes [56].

In the field of NDE, typical short pulse waves with a centre frequency ranging between 0.1 – 15 MHz are deployed. Higher frequencies, typically used to inspect metals [11, 12], allow the detection of smaller defects due to shorter wavelengths, however, the ultrasonic wave won't propagate as far due to the attenuation. Lower frequencies suffer from attenuation less and therefore allow inspection deep within the test piece, for example in concrete structures [57]. However, this parameter is traded for lower sensitivity to smaller defects. In terms of inspection of WAAM, the research has been mainly published on inspection using frequencies between 5-10 MHz [10, 12, 53, 58], where the attenuation of the ultrasound wave was leveraged with a detectability of defects as small as 0.5 mm in diameter [53].

2.4.1. Ultrasonic Wave Modes

Ultrasound waves can be best described as mechanical vibrations. Longitudinal (Compression) ultrasonic waves oscillate the particles parallel to the propagation direction, while the traverse (shear) waves oscillate the particles in a direction perpendicular to the direction of the propagation direction as illustrated in figure 2.5. Longitudinal waves can propagate through solids, gases or liquid media while the utilization of shear waves is limited to solid components since liquids nor gasses have a shear strength to facilitate the propagation of the shear waves. In this thesis, only the use of longitudinal waves is considered and explored.

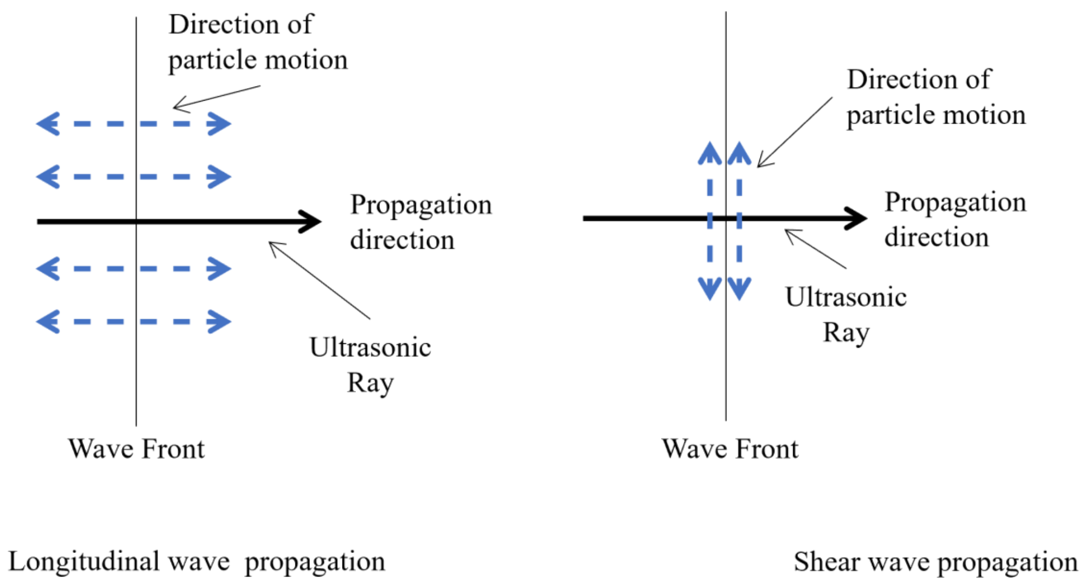

Figure 2.5 Ultrasound wave propagation in solid medium showing a longitudinal and a shear wave

2.4.2. Acoustic Impedance

When an ultrasound wave approaches the interface between two materials with different acoustic properties, such as impedance, a portion of the wave is transmitted inside the component while the rest of the wave energy is reflected. The acoustic impedance Z (kg/m^2 s or Rayl) for ultrasound waves propagating in lossless isotropic material given by:

$$Z = \rho.v \tag{2.1}$$

Where ρ is the density of the material (kg/m^3) and v is the velocity of sound in the material (m/s). The acoustic transmission/reflection coefficient for normal incidence of ultrasound wave can be calculated by:

$$RE = (\frac{z_1 - z_2}{z_1 + z_2})^2 \qquad 2.2$$

Where *RE* is the reflected energy coefficient, the z_1 and z_2 are the acoustic impedance of the first and the second medium respectively.

2.4.3. Wave Refraction and Mode Conversion

When the ultrasound wave intercepts an interface between two media with different speeds of sound, the refraction occurs. The larger the difference in speed of sound between the two materials, the higher the refraction angles. Therefore, the refraction angle can be described by Snell's law:

$$\frac{Sin(\theta_i)}{v_1} = \frac{Sin(\theta_r)}{v_2} \qquad (2.3)$$

where the v_1 and v_2 are the velocities in the first and second medium while $Sin(\theta_i)$ and $Sin(\theta_r)$ are the angle of incidence and refraction respectively.

Mode conversion is the ability of the ultrasonic wave to convert from one wave mode into another, for example when a longitudinal wave can convert into a shear when refracting at the interface between two materials with different acoustic velocities. Figure 2.6 shows an example where the longitudinal wave incoming under an angle θ_1 is refracted at the interface into two components: I) θ_{2s} is a shear wave and II) θ_{2l} is a longitudinal wave.

The two critical angles can occur when considering refraction: I) θ_{2l} reaches 90 degrees, the longitudinal wave is no longer refracted into the sample but exists as a rapidly decaying creep wave [59], II) At the same time, if the θ_{2s} reaches 90 degrees no significant energy is penetrating the component either.

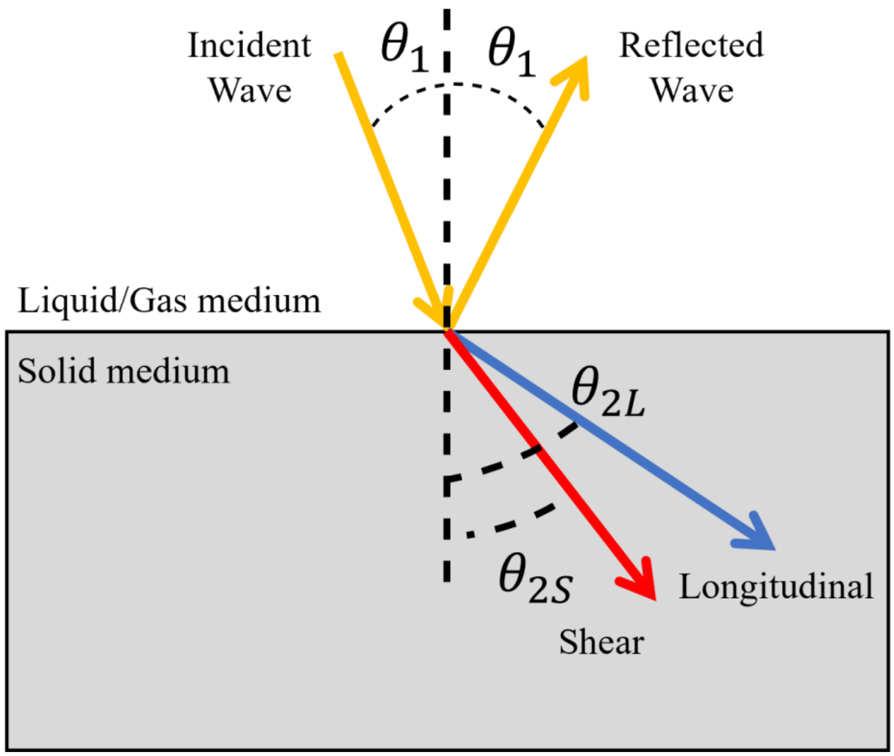

Figure 2.6 Wave refraction at the interface

2.4.4. Conventional Ultrasonic Testing

Traditionally, the ultrasound NDT is performed through contact with a specimen using UT transducers. A commercial UT transducer is a piece of equipment commonly made of a piezoelectric ceramic crystal in protective housing. The ultrasonic waves are generated by conversion of the electrical energy into mechanical energy. Retrospectively, the reception is achieved by a conversion of the mechanical vibration applied to these crystals which generates the voltage that is then measured as a signal [60].

Further, to maximize the energy transmitted into the test piece, a thin layer of liquid coupling is applied to the interface between the probe and a sample to remove any air gaps between the probe and the targeted material.

Figure 2.7 shows a single element pulse-echo configuration where a single pulse is excited into the component and received by the same probe. If the sample is defect-free, a back wall reflection can be observed on the A-scan (Scenario 1), which is the simplest visualization showing a signal amplitude as a function of time. However, when a defect is present between the transducer and the back wall, part of the energy is reflected back to the transducer and an additional echo can be observed (Scenario 2). Using the known material acoustic velocity and the depth at which this flaw exists can be measured. The pulse-echo approach is further utilized in this thesis where due to access restrictions given by the restrictive nature WAAM process itself, the robotic in-process ultrasound inspection can only be deployed through an as-built surface of the component to assess the structural integrity of the built volume.

Further, an alternative inspection configuration consists of a pair of transducers. In this configuration, one transducer is employed to transmit the ultrasound wave while the second transducer is set as a receiver. This configuration is known as through transmission or pitch-catch. Assuming an inspection of the defect-free component (Scenario 3), a high amplitude signal is retrieved. However, as soon as a flaw is present, the retrieved amplitude drop is visible, which indicates a disturbance in wave propagation (Scenario 4).

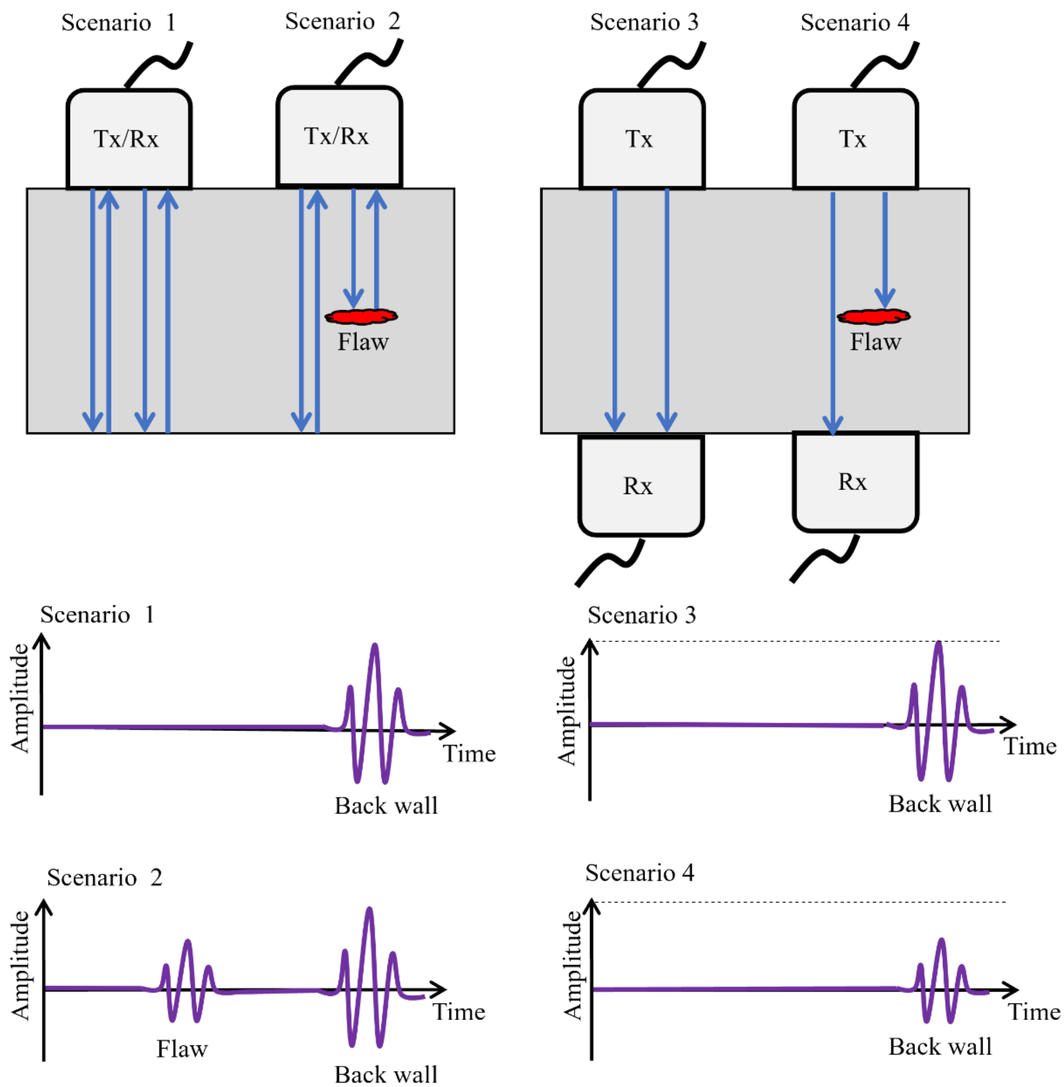

Figure 2.7 Most common ultrasound inspection configuration: pulse-echo and pitch-catch

2.4.5. Phased Array Ultrasound

Commercial Phased Array Ultrasound Transducers (PAUT) are devices containing a number of independently incorporated piezoelectric crystals (elements) housed in a single case either in a linear (1D) or two-dimensional planar configuration [61]. These sensors offer a higher degree of flexibility as compared to a single element or split crystal transducers, given that transmission and reception can be achieved by a combination of many active elements. Moreover, parameters such as voltage, delay or pulse width can be controlled for each PAUT element individually.

The approach of selectively transmitting the sup-aperture of elements is called beamforming and the technique enables a range of inspection modes to be performed from one location using a single PAUT. For example, a sub-aperture of elements can be excited, without a variation in delays, producing a plane wave (Figure 2.8 (a)) [62]. When inspecting a specific location within a targeted volume, focused imaging (Figure 2.8 (b)) can be utilized to focus the beam on a single point (depth) directly under the transducer. Alternatively, the ultrasound beam can be steered towards the targeted location under the angle (Figure 2.8 (c)) [63].

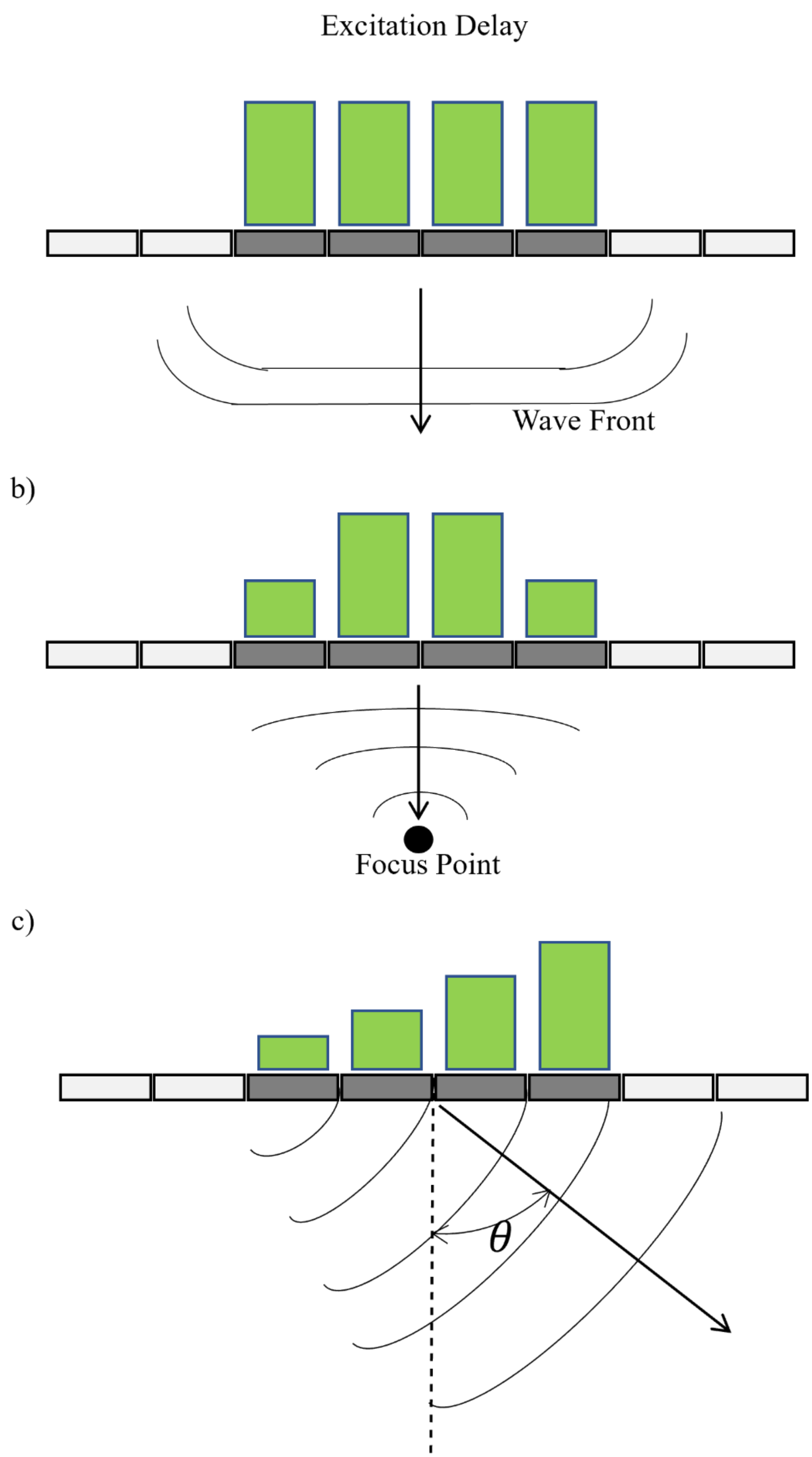

Figure 2.8 Phased array pulse generation applications

2.4.6. Convectional Phased Array Imaging

Received signals from the ultrasonic waves returning into the transducer can be processed and visualized through many different imaging methods. As mentioned in section 2.4.4, the simplest form of visualizing the received ultrasound signals is an A-scan. However, by utilizing the advantages of the PAUT probes, returning more than a single A-scan in beamforming scenarios such as focused linear or angled inspection, the results of the inspection can be visualized on 2-dimensional plots called B-scan (Figure 2.9 (a)). This enables visualization of the interior of the specimen as a function of depth (time) where the lateral dimension is defined by a total number of retrieved A-scans. Given an example scenario where a component is tested using a 64-element PAUT and a single sub-aperture is formed using 32 elements while the aperture is shifted across the whole PAUT with an increment of 1 element, the total number of A-scans forming a B-scan is 33.

Further, another technique used throughout this thesis is called C-scan. This method is commonly associated with inspection scenarios where a large number of B-scans frames are acquired, such as robotic inspection of an aircraft wing cover [64]. The C-scan image is formed by stacking the acquired (encoded) B-scan frames together. Subsequently, the maximum amplitudes are extracted from a predefined window (gate) and a top-plane view over the component can be obtained, as visualized in Figure 2.9 (b).

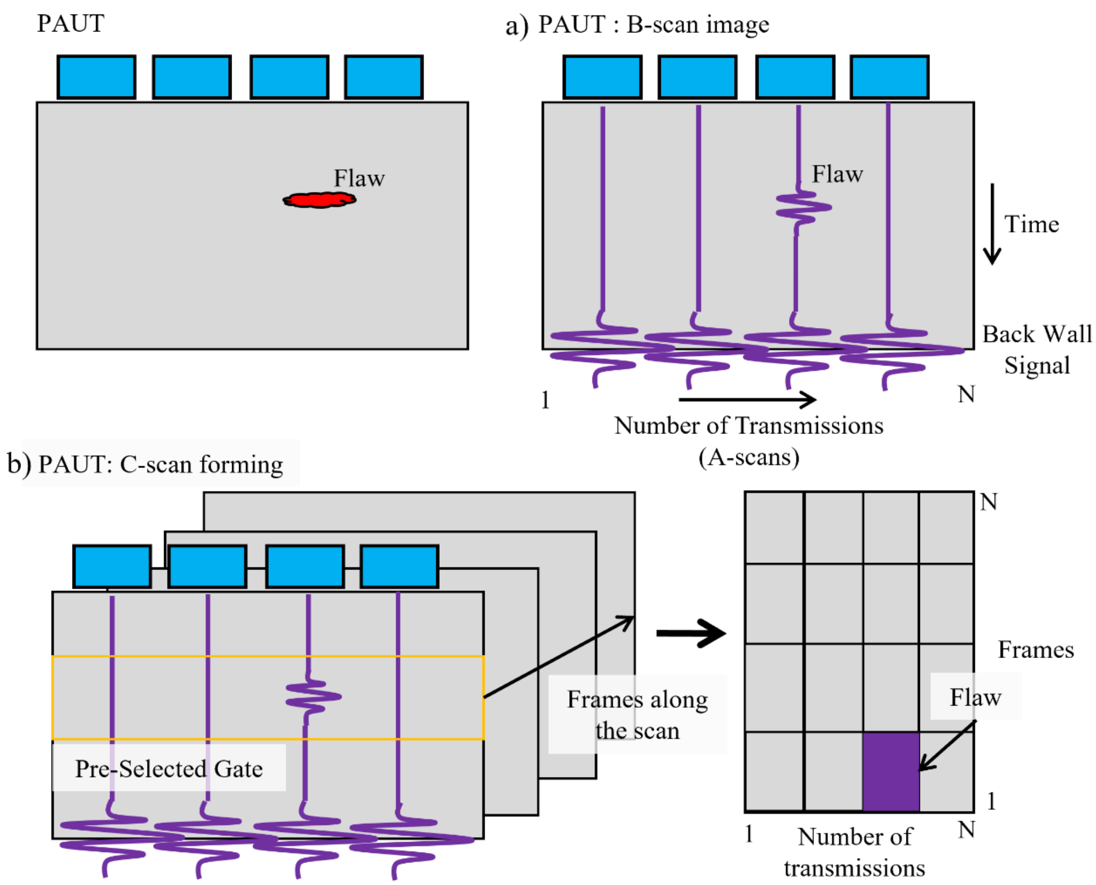

Figure 2.9 Conventional imaging techniques showing a B-scan image and C-scan image formation

2.4.7. Ultrasound Full Raw Data Acquisition & Post-Processing Algorithms

Having numerous elements that can be activated individually in a PAUT enable the acquisition of ultrasonic Full Raw Data (FRD), where the whole set of ultrasound data in the time domain is collected, using a technique such as Full Matrix Capture (FMC). In this method, the data is acquired by firing a single element in sequence while the whole aperture is set to receive as seen in Figure 2.10 (a) [65]. The acquired FMC data are stored as N^2 matrix of A-scans with a pre-specified length.

Following a post-processing algorithm are applied to form an interior image of a targeted volume. One such algorithm, used throughout this thesis, is called Total Focusing Method (TFM), which retrospectively forms an image by summing amplitudes from all transmit-receive combinations to every pixel (figure 2.10 (b)) [66]. This is conducted on a Delay-And-Sum (DAS) basis where at first the Time of Flight (ToF) between the transmitting element, pixel and receiving element is calculated. Based on these ToFs, the corresponding amplitude value is summed into the final image. Hence, the formation of a fully focused interior image of the component is achieved, enabling a superior resolution and sensitivity to smaller defects as compared to conventional electronic beamforming [66].

Further, the FMC data acquisition can be linked with a DAS algorithm called Synthetic Aperture Focusing Technique (SAFT), which is similar to the TFM image technique with the difference that the SAFT enables selectively limiting the number of contributing transmitting or receiving aperture to each image pixel [67]. The limit can be a for example vertical angle between the pixel and PAUT's element. This is utilized and further explored in Chapter 3, where the technique is employed for surface reconstruction of the test piece's top interface.

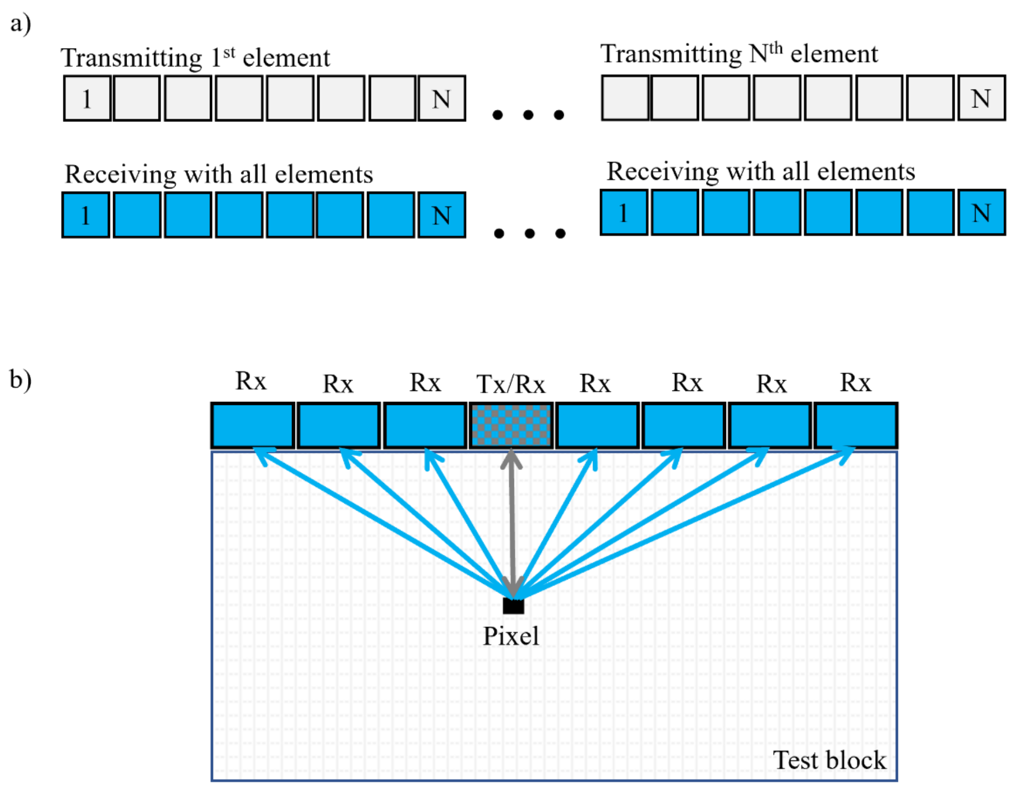

Figure 2.10 (a) Full Matrix Capture and (b) Total Focusing Method

Additional FRD collection technique, employed in this thesis (Chapter 5), utilizes the advantage of creating a sub-aperture of elements focused to form a larger beam. The technique is called Virtual Source Aperture (VSA) and the data are acquired by exciting a group of elements with pre-calculated delays. The ultrasound beam profile is created from a virtual point above the physical array, as illustrated in Figure 2.11. Typically, the point is placed above the centre of the sub-aperture with a height equal to the distance from the first element to the centre of the sub-aperture [68]. The sub-aperture is then excited by applying delays to its elements individually which resulted in a newly formed large beam profile. The signal returning to the array is received by every element within the array forming a matrix of A-scans similar to that for convectional FMC.

Subsequently, the data post-processing is accomplished using the DAS algorithm in the same approach as FMC data. The difference exists where the transmit locations corresponding to the virtual source point of transmitting sub-apertures are used for the ray-tracing computations.

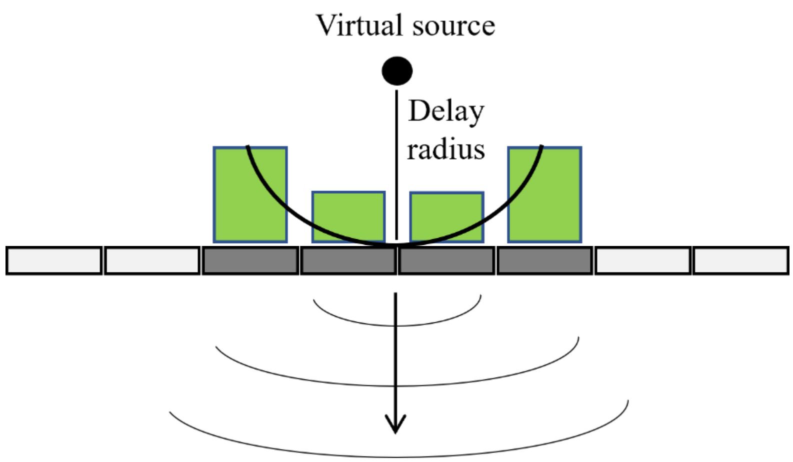

Figure 2.11 Illustration of the creation of the virtual source aperture

2.5. Automated Coupled Ultrasound In-process WAAM Inspection

2.5.1. Automated NDE

Automated deployment of the NDE into the industrial environment enables the option to increase the inspection accuracy in terms of positioning and to achieve higher scanning speeds as compared to the manual deployment of the NDE [69]. Further, automation allows sensor deployment in inhospitable environments such as the WAAM build process, removing any risk of human injuries and harmful conditions.

In fields of welding, joining and large-scale manufacturing, automated NDE is typically deployed by axial manipulators such as gantries or robotic arms, both depicted in Figure 2.12. These devices often operate in a cartesian coordinate system where more primitive gantries allow planar positioning of the NDE setup and while robotic arms can deliver sensors anywhere within a spherical working envelope, due to the 6 Degrees of Freedom (DoF) coupled with high pose repeatability and speed [70]. 6 DoF robotic arms can also be integrated with a track system, which extends its reach to inspect large structures such as aircraft wings [64]. The robotic arms are widely used in industries owing to their flexibility and programmability, where the operation can be conditioned by additional sensors such as force/torque sensors which increase their inspection precision by maintaining correct force/torque and orientation across components. Further, the safety features can be implemented making an automated manufacturing environment hazard-free.

Figure 2.12 Axial manipulators suitable for automated NDE delivery

2.5.2. Ultrasound In-Situ Inspection of As-Built WAAM Components

Traditionally, WAAM component manufacturing and NDE tend to be separate operations and usually sequential within the WAAM process. Incorporating these processes together, by implementing NDE within the WAAM manufacturing process, seeks to decrease: I) time of transfer between cells, II) costly deposition over defective layers and III) expensive repairs or scrappage [13]. Present-day ultrasonic inspection approaches, executed on these AM components are either: (a) inspection inside water immersion tanks using gantry or robotic systems, or (b) tested by hand after the WAAM's surface is machined flat for contact ultrasonic inspection [11, 12, 53, 71]. However, immersion testing of large WAAM components on the order of meters, is very difficult and sometimes unserviceable, and even in such a configuration, machining the coupling interface is favored to prevent the ultrasonic wave from refracting and scattering at the surface. Moreover, to perform an immersion test, the component is almost always carried to a different dedicated NDT station further prolonging the full build process.

For the conventional ultrasonic testing to be conducted on a WAAM component, often a milling operation is sought to be implemented into the manufacturing cycle [72], again to prevent ultrasound wave refraction and scattering at the surface/couplant interface. Such surface machining amplifies the component processing time and cost, while creating a bottleneck that lowers the production throughput. In [53], the WAAM components were tested by an ultrasound probe from below the bottom substrate plate [53] and despite this method abolishing the need for a top surface machining operation, it is not a viable approach due to the increasingly more popular WAAM deposition process which utilize double-sided deposition strategies to diminish the effect of residual stresses and avoid part distortion [73]. Moreover, manually performed ultrasound NDE of large-scale WAAM components is extremely time-consuming which further generates bottlenecks in the production process. Additionally, conventional ultrasound transducers are typically only operational up to 60 °C, and with the WAAM as-built surface potentially being at hundreds of degrees Celsius just after the deposition [18] further long dwelling times and delays are necessary to be put in place within the production process.

The acoustic coupling in ultrasonic inspections is usually created by an acoustic liquid gel, where a thin layer eliminates any air gaps between the transducer and the surface due to material roughness or small-scale geometrical discrepancy; thus, enabling transmission of the ultrasound pulse into the targeted component. The use of such a liquid gel is however not permitted for in-situ NDE of WAAM components since it would require a constant supply of the liquid to the probe and WAAM surface, which would also contaminate the WAAM during a subsequent deposition. Despite emerging novel liquid-filled wedges [74], that are capable of conforming to the rough upper surface of WAAM components, these often still require an acoustic gel to provide coupling and allow smooth frictionless motion without constant wear of the wedge's surface.

Non-contact ultrasound inspection techniques such as Laser Induced Phased Arrays (LIPA) [6] and air-coupled UT could bypass these surface coupling challenges, and LIPA has shown great potential for detecting small defects in AM components. However, among its critical shortcomings is the requirement for a polished surface [75], which is inconsistent with the as-built surface condition of the WAAM process.

Dry-contact approaches, that facilitate the transmission of ultrasonic energy into a WAAM component without the utilization of liquid couplants, offer great potential for dry-coupling and reduced surface contamination. Such dry-coupling can be accommodated by acoustically matched polymers, which offer low attenuation and ultrasound velocities similar to water [76] and [77]. When the polymer gets placed between the transducer and the WAAM specimen and suitable force is applied, the air between the two mating surfaces is pushed out and the acoustic energy is transferred in a similar fashion to liquid coupled approaches. However, when automated deployment and surface scanning get considered, excessive and damaging shear forces can be introduced from dragging these polymers across the surface which could have a significant damaging effect and therefore reduce the life of the polymer.

Based on all aforementioned constraints, a coupled ultrasound inspection approach, suitable for automation and capable of withstanding high temperatures, is required.

2.5.3. Automated Contact-based In-process WAAM NDE Using Ultrasound Roller-probe

When considering the architecture and the delivery of an ultrasound probe for an automated in-situ deployment on as-built WAAM components, two main challenges emerge: (1) Acoustic wave transmission into the component through the as-built surface, and (2) Withstanding the hostile elevated surface temperatures of the as-built component.

These challenges can be overcome using a dry-coupled ultrasonic roller-probe. Conventionally, a roller-probe is a device with either a single element or a phased array transducer encompassed with an acoustically optimized rubber wheel allowing for faster manual inspection of geometrically larger components [77, 78]. Due to the design adaptability and ease of use, roller-probe technology has been also employed for the needs of automated inspection of large structures [64, 79]. Recent developments have also shown the deployment of the high-temperature liquid-filled roller-probe on in-process inspection of multi-pass welds [80]. In this thesis, a roller-probe is introduced for the dry-coupled inspection of large-scale WAAM components in order of meters [58] but has the potential to be adapted to a variety of large-scale additive manufacturing techniques or large structures. The WAAM roller-probe [58], depicted in Figure 2.13, is equipped with a watertight rotary rubber tire (6 mm thick, made of high temperature resistant silicone rubber) and a delay-line (26 mm thick, made of Polyetherimide polymer) through which the ultrasonic wave generated by the ultrasonic array can propagate. A solid delay line enables conformance of the rubber to the surface of WAAM by a sufficient amount of force. The roller-probe is also filled with liquid (for example water) to enable possible active cooling. However, the mechanical design and the configuration of the roller-probe were outside of the scope of this thesis and the cooling was not implemented into the setup. The ultrasonic array is mounted in the center of the roller-probe on the delay line. A key advantage of this design can be realized in automated inspection setups, where the rotary design directly facilitates automated delivery and smooth manipulation over varying profile surfaces at speed. Additionally, the roller-probe is designed to withstand surface temperatures of up to 350℃, meaning it can be deployed on the WAAM surface just after deposition when the sample is still at elevated temperatures, either in-situ or after the full built is completed. Moreover, the advantage of the roller-probe can be also realized by the ability to curtail the configuration of the internal components (e.g. thickness of delay line or rubber), which would result in changes to the operational envelope of the roller-probe by changing the maximum depth of inspection or length of duty cycles under high temperatures.

It is worth noting, that the roller-probe presented in this thesis was developed and built in-house at the University of Strathclyde (Centre for Ultrasonic Engineering) by the team working in the field of automated and in-process inspection of welding processes and WAAM [58]. It is worth noting that the development of the roller-probe device was not a concern of this thesis and the author is a user of the device for the research purposes.

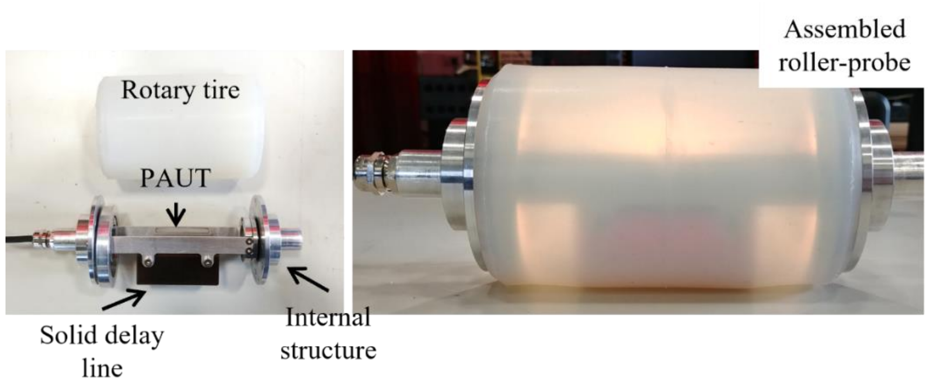

Figure 2.13 Visualisation of internal roller probe structure and an assembled roller-probe

Chapter 3

Multi-Layer Ultrasonic Imaging of As-Built Wire + Arc Additive Manufactured Components

3.1. Introduction

When considering a novel ultrasound WAAM roller-probe for inspection of as-built WAAM components, the challenge of ultrasound beam refraction arises. This is due to the internal structure of the sensor, which is based on a solid delay line encompassed by the outer rotary tyre, which is in contact with a non-flat interface of the WAAM component, as illustrated on Figure 3.1. As described in chapter 2, when the ultrasound wave hits the interface between two materials with different acoustic properties, the wave refracts at a different angle. Therefore, this phenomenon must be accounted for during the inspection.

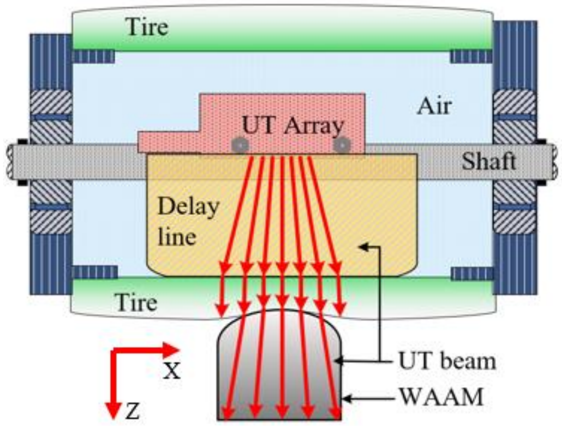

Material	Acoustic Velocity (m/s)	Thickness (mm)
Delay line	2480	26
Tire	1006	6
WAAM	5800 - 6300	

Figure 3.1 Interal structure of the roller-probe with illustrated refractions at the interfaces between internal components and WAAM

Precise ultrasonic imaging of the specific volume and beam tracing through two refractive arbitrary interfaces between three layers are challenging to overcome using conventional ultrasonic methods such as electronic beamforming [81]. When employing conventional electronic beamforming (focusing) imaging, the phased array delay laws are calculated for each element prior to the scan to focus the beam at a specific location in the targeted material through the anticipated knowledge of the component’s surface profiles at the interfaces. Then, the array is excited using these focal laws and a stack of A-scans, to form a (depth) focused B-scan image with the fixed limited horizontal resolution, is returned. However, anytime the curved profile of the interface changes during the scan, in this case, the WAAM as-built surface, the focal laws must be recomputed for an accurate beam focus and an enhanced Signal-to-Noise Ratio (SNR).

In order to deploy such an approach, the perpetual online acquisition of the surface profile is necessary to re-generate correct focal laws for the variations which can greatly affect scanning rates and likely require additional hardware (eg. Optical scanning systems). In view of these challenging constraints, alternative fully focused imaging processes that can accommodate high scan speeds and can offer the potential to automatically detect surface profiles from a single dataset should be sought for automated inspection applications.

Such a task can be delivered through a combination of real-time data acquisition and subsequent processing initiated as soon as the first frame of data is acquired. As introduced in Chapter 2, FMC data allows the implementation of a wide range of post-processing algorithms [65], that seek to address the challenges mentioned above.

The collected FMC data can be used to form images using post-processing algorithms, such as the TFM. When considering multiple media inspections, current post-processing TFM-based inspection practices, however, have been mainly developed and utilized for two-media inspection. For example, welds are traditionally tested using shear wedges positioned on the top flat surface of parent materials, where the beam is steered into the weld under angle [82]. In the matter of ultrasonic imaging of components with complex surface geometries, the main research focus has been addressed by the development of two-media adaptive TFM imaging for immersion (water/sample) setups or water-filled conformable delay lines used in contact with complex surfaces [83]. Such two-media algorithms are, however, application-specific and are not suitable when considering the three-media inspection of as-built WAAM components using the roller-probe transducers introduced above.

Moreover, to be able to form TFM images of the WAAM components after the FMC acquisition, the geometry of the unknown interfaces should be identified. Given the known and flat delay-line/tyre interface, illustrated on Figure 3.1, it is necessary to include a stage to reconstruct Tyre/WAAM interface surface profile. The surface profile reconstruction algorithm developed for this work is based on dual-medium Synthetic Aperture Focusing Technique (SAFT) imaging, an algorithm studied and proven effective for the reconstruction of the interfaces using ultrasound [67]. The technique is based similarly to TFM on DaS computational logic with a difference in the limitation on how many receiving elements are contributing to each pixel. This limit is typically set by a vertical angle between a targeted pixel and an array element.

Based on the advantages of the approaches introduced above, the body of this chapter introduces the SAFT-TFM package based on SAFT surface reconstruction and 3-layer adaptive TFM for roller-probe inspection of a-built WAAM. The presented approach is described, and its performance is evaluated on two WAAM test components inspected from their as-built surface with artificial calibration reflectors and realistic LoF defects.

3.2. Background

3.2.1. The Full Matrix Capture and Total Focusing Method

Ultrasonic phased array transducers were designated for the data acquisition process, where time-domain signals from every pair of the transmit (Tx) -receive (Rx) elements were acquired to form the FMC data frame in real-time. For a linear array with N elements, a total number N^2 A-scans were recorded and stored. The illustrations of

Figure 3.2 (a) depict the sequence of transmit-receive elements activated in an FMC acquisition mode where a single transmit element was stepped by 1 between 1 to *N*, and for each transmission, all the *N* elements were used in the reception.

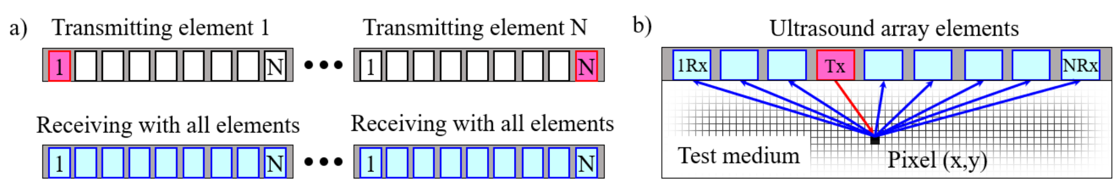

Figure 3.2 Diagram showing a) FMC and b) TFM

The FMC dataset embodied the input to the imaging stage that was accomplished using a DAS algorithms package. In the TFM algorithm introduced in this chapter, the complete aperture of the phased array transducer was employed to synthesize a focus on every single image pixel of the B-scan at both the transmission and the reception, as illustrated in Figure 3.2 (b), allowing fully focused dense resolution across the whole image, and therefore, increased sensitivity to smaller defects within the image volume. For every image pixel *P* within the inspection range, the image intensity *I(P)* for each transmit-receive combination was calculated through:

$$I(P) = \sum_{i=1}^{N} S_{Tx,Rx}\left(T_{Tx(i,j)} + T_{Rx(i,j)}\right) \tag{3.1}$$

where, $S_{Tx,Rx}$ is the time-trace associated with the A-scan of every Tx-Rx combination, $T_{Tx(i,j)}$ represents a ToF from the transmitted element to the pixel (i, j), and $T_{Rx(i,j)}$ stands for the return journey from the pixel to the element. A TFM image frame ($I_{(i,j)}$), with grid point indexes (*i*, *j*), was computed using the elementary A-scans within the FMC dataset, while a secondary one ($I'_{(i,j)}$) was also obtained through a Hilbert transform of the A-scans with the application of the same delays. Consequently, the TFM envelope ($I_{envelope}$) was calculated using the following formula:

$$I_{envelope} = \sqrt{(I_{(i,j)})^2 + (I'_{(i,j)})^2} \tag{3.2}$$

Therefore, the resulting image was composed of two TFM images: (I) one produced from the real component of the elementary A-scans, and (II) the other from the imaginary component of the elementary A-scans. The main advantage of the enveloped image lies in the possibility of increasing the grid pixel size, hence, curtailing the computation time needed to compute the image without losing the intensity of the signal [84]. Finally, to present the pixels in a dB scale with reference to the maximum amplitude of the image, the pixel amplitude I_{amp} values were normalized by the maximum amplitude I_{amp_max} present in the image as shown in Equation 3.3.

$$I_{amp\_norm} = 20 \times log_{10}(\frac{I_{amp}}{I_{amp\_max}}) \tag{3.3}$$

3.2.2. Focusing Through Multiple Media

This chapter aims to implement a TFM algorithm for imaging WAAM components through three mediums and across two interfaces present during a roller-probe inspection. When the ultrasound wave is transmitted from the transducer it firstly gets refracted at the fixed planar delay-line/tyre interface inside the PAUT probe and then the wave refracts the non-planar tyre/WAAM arbitrary contour interface on the as-built

WAAM surface. This process must also be accounted for on reflected ultrasound waves from the interior WAAM as it propagates to the component and back into the transducer. The focus calculations were carried out according to the minimum ToF principle, which is also known as Fermat's principle [85]. In the case of homogeneous media, a straight line connecting an element and an image pixel best describes the path along which an ultrasonic wave generated by the element traverses to reach a specific image pixel. However, when a media existing as a set of multiple materials with different acoustic properties is considered, the ultrasonic waves generated by the elements refract at the interfaces before reaching the image pixel in the target medium; hence, the orientation of the wave traveling path is different in each medium. To this end, the ToF's should be calculated individually in each medium as illustrated in Figure 3.3 (a). In the cartesian coordinates, the algorithm for ToF $T_{(i,j)}$ for both Tx and Rx array elements to pixel (i, j) in the WAAM component can be formulated as:

$$T_{(i,j)} = \frac{\sqrt{(x_{i1} - x_t)^2 + (y_{i1} - y_t)^2}}{v_1} + \frac{\sqrt{(x_{i2} - x_{i1})^2 + (y_{i2} - y_{i1})^2}}{v_2} + \frac{\sqrt{\left(x_p - x_{i2}\right)^2 + \left(y_p - y_{i2}\right)^2}}{v_3} \tag{3.4}$$

where the $(x_t\ , y_t)$, the $(x_{i1}\ , y_{i1})$, the $(x_{i2}\ , y_{i2})$, and $(x_p\ , y_p)$ are respectively, the coordinates of the array elements, the incidence point of the ultrasound ray to the first interface, the incidence point of the ultrasound ray to the second interface, and the targeted pixel. The (v_1), (v_2) and (v_3) are the velocities in the first, second and third medium.

The wave refraction angles at the interfaces were also calculated using Snell's law which is presented in its most common form in Equation 3.5, where θ_i and θ_r represent the angles of the incidence and the refraction, respectively, as illustrated in Figure 3.3 (a). It should be noted that the refraction angle at the incidence point on the arbitrary profile was also calculated with respect to the normal of the surface at the point illustrated in Figure 3.3 (a).

$$\frac{Sin(\theta_i)}{v_1} = \frac{Sin(\theta_r)}{v_2} \tag{3.5}$$

In this work, a root-finding algorithm based on a bisection method was developed and used to trace the ultrasound ray path between the array elements and the image pixels to a precision defined by the user. Clearly, higher precision demands a longer algorithm runtime due to the increased number of iterations required to converge to a solution. The ray-tracing workflow used within the algorithm is shown in Figure 3.4 and demonstrated in Figure 3.3 (b), and can be summarized in the following steps:

1. Initially, a finite number of equally spaced nodes (i'_n) are produced at the first interface (delay-line/tire).
2. The ray (Tx_n), with *(n=Node number on the first interface),* transmitted from an element is connected to each of the nodes with the straight lines and the refracted angles calculated at the first interface and at each node.

3. The point coordinates at which the rays refracted from the first interface impinge the second interface are located, and the resulting refraction angles from the second interface are calculated.
4. The $T_0,\ldots,T_n$ points where the rays refracted from the second interface ($i2$) approach the pixel's *y* coordinate are indicated and the positional error of the rays in the *x*-direction with the reference to the target pixel is assessed. Following that, the two coordinates closest to the targeted pixel are chosen, while the rest are discarded.
5. If the error is larger than the maximum allowed distance between an incoming ray and the pixel point, a new i' is selected. Otherwise, the path with the lower error is stored and a new pixel-element pair calculated.
6. To select a new i'_n, the error coefficient (c) is obtained as an absolute value of the division of the two errors between T_0 , T_1 and targeted pixel. It is necessary to make sure that $0 \leq c \leq 1$, thus a larger error is always divided by a smaller value.
7. The coefficients are then applied, where the distance between two previously used i'_n and i'_{n-1} are subtracted and multiplied by the coefficient, giving a new offset. Subsequently, this offset is added or subtracted from the latest i'_n depending on whether the T_n is larger or smaller than a targeted pixel.
8. The process is iterated until the distance measured between the T_n and the pixel becomes smaller than the error indicated. This yields the ray path (Tx) and the ToF from an element to a pixel in the image.
9. The process is repeated until the ToF's for all the combinations of elements and pixels is reached.

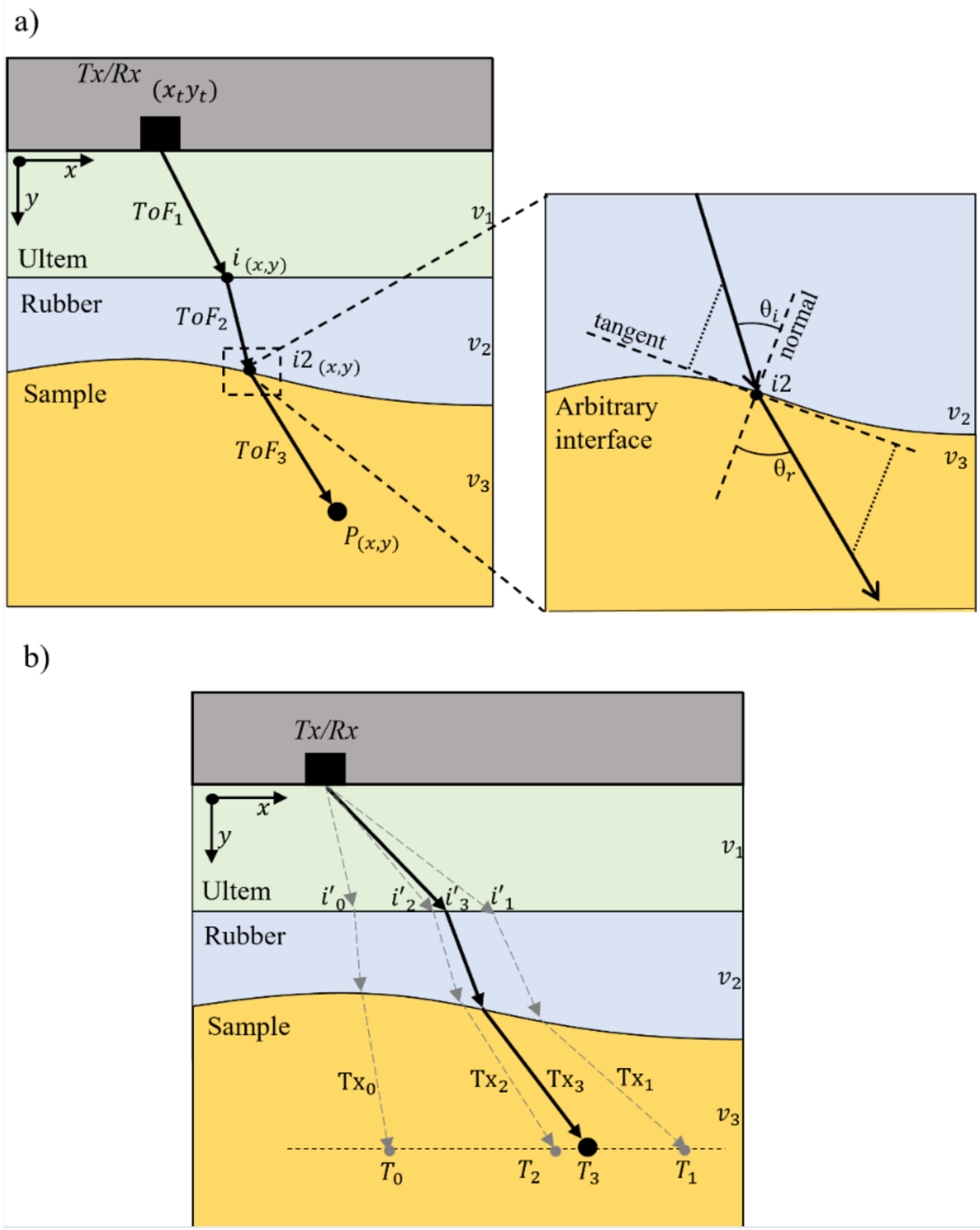

Figure 3.3 Schematic diagram showing a) ray-tracing and time of flight calculations between an array element and a target pixel through three media with refractions on planar (delay-line/tyre) and non-planar (tyre/WAAM) interfaces, and b) iterative process and convergence to a target pixel using the search algorithm.

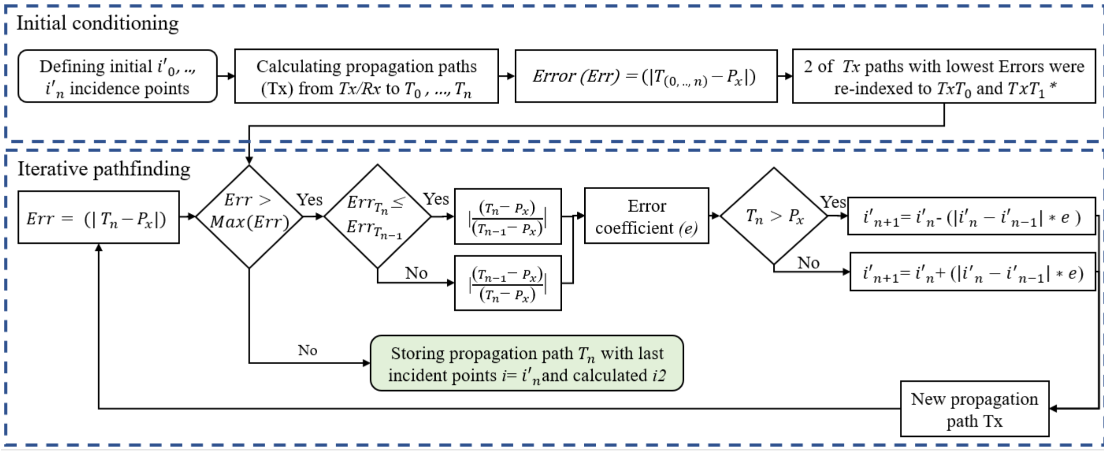

Figure 3.4 Diagram explaining the search algorithm developed for ultrasonic ray-tracing

3.2.3. Ultrasonic Driven WAAM Surface Reconstruction

The first step taken in the imaging process is to estimate the surface profile of the WAAM component. Assuming the planar interface of the delay line/tyre does not vary, the WAAM surface interface region can then be directly imaged. To accomplish this, a dual-medium (*i.e.* ultrasound ray travel through the delay-line towards the bottom of the rubber interface) DAS SAFT algorithm with angular aperture limit was developed. The limitation was established by $-\alpha$ and α angles located between the outmost rays focused on each pixel and the normal of the first interface, as depicted in Figure 3.5. The intensity of each pixel in the image was computed using the velocity of the first (v_1) and second (v_2) media only, and given by:

$$I_{rubber}(P) = \sum_{i=1}^{N} \sum_{j=\alpha}^{\beta} S_{Tx,Rx} \left(T_{Tx(x,y)} + T_{Rx(x,y)}\right) \tag{3.6}$$

Where, $T_{(x,y)}$ was given by:

$$T_{(x,y)} = \frac{\sqrt{(x_1 - x_t)^2 + (y_{i1} - y_t)^2}}{v_1} + \frac{\sqrt{(x_{i2} - x_{i1})^2 + (y_{i2} - y_{i1})^2}}{v_2} \tag{3.7}$$

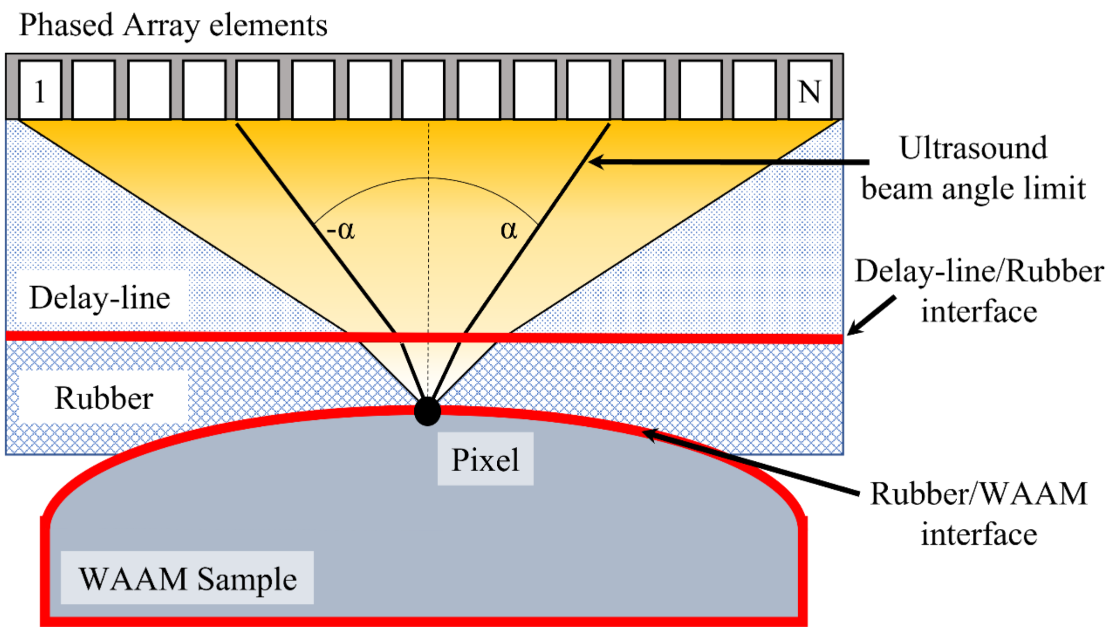

Figure 3.5 Diagram illustrating the phased array elements contribute to the pixel of the SAFT image targeting the tyre/WAAM interface, and limited by the angles -α and α

The surface points are extracted using global thresholding once the surface image has been created. The approach is intended for column-by-column automatic surface reconstruction sweeps of the image to locate the pixels with the greatest intensity value above a preset threshold. The method keeps the pixel with the lowest *y* coordinate if two identical values occur in the same column. This was added to avoid inaccuracies caused by greater signals received from the inside of the specimen or signals ascribed to the second reflection. The extracted pixels were sufficiently defined with a 4th order polynomial curve, smoothed by the local polynomial regression, knowing the characteristic surface finish of WAAM builds deposited with common deposition strategies, which typically represent a semi-elliptical shape with waviness. Smoothing the curve was also required to eliminate potential curve distortions induced by dislocated surface points in the presence of a false echo in the surface image.

It is worth noting, that this work only considers surface reconstruction in two dimensions from a single FMC frame, given a full TFM computation occurs on a single FMC frame to assure the image computation can be initiated as soon as the FMC frame is acquired. Further, it is outsides of the scope of this project to link all the surface frames into the 3d model given it would not have a high impact on the image quality obtained on the studied samples featuring a smooth surface finish in the deposition direction.

3.3. Experimental work

3.3.1. Phased Array Ultrasonic Inspection Configuration

Table 3.1 presents the parameters of an ultrasound phased array transducer employed in the WAAM roller-probe throughout the experimental work.

Table 3.1 Phased array probe parameters

Array Parameters	***Value***
Element Count	64
Element Pitch	0.5 mm
Element Elevation	10 mm
Element Spacing	0.1 mm
Centre Frequency	5 MHz

The roller-probe featured a 26 mm high delay line with an acoustic velocity of 2480 ms^{-1}. The assembled roller-probe was filled with a liquid gel as a couplant at the interfaces of the array/delay-line and the delay-line/tyre. Moreover, a silicone rubber tyre with high-temperature compliance of up to 350°C constituted the exterior layer of the roller-probe. Figure 3.6 depicts the setup used for the experimental work, where the roller-probe was mounted on a 7-axis KUKA LBR robotic arm that featured embedded force-torque sensors in its joints. The robot facilitated the measurement and steadiness of the set force and torque values of the end effector. This feature was utilized to maintain a safe constant contact force of 50 N between the roller-probe and the tested WAAM component. FMC data was acquired and stored at 12-bit resolution using a Peak NDT LTPA phased array controller. The excitation voltage was set to 200 V and a fixed hardware gain was set to 65 dB. The obtained time-domain matrix of the A-scans corresponding to the signals from the individual transmit-receive combinations contained 8000 data samples per A-scan acquired at the sampling frequency of 50 MHz.

The SAFT surface finding and TFM imaging algorithms were programmed within a MATLAB 2020a environment. The processing time performance was assessed on an AMD Ryzen Threadripper 3960 24 core Processor with a clock speed of 3.79 GHz and 128 6Gb of Random-Access Memory. The elapsed time for the SAFT to output the surface profile curvature was 3.1 seconds, and the convergence for the complex ray-tracing calculation and the TFM image forming was 30 seconds.

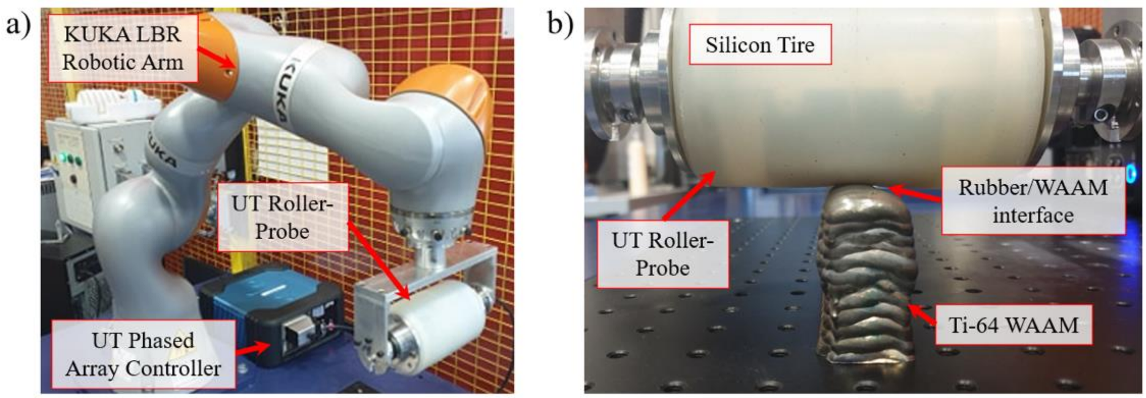

Figure 3.6 Robotic ultrasonic inspection set-up consisting of (a) a KUKA robotic arm, ultrasound phased array controller, and (b) an ultrasonic roller-probe placed on a titanium WAAM sample

3.3.2. Imaging Process Flow

Figure 3.7 shows a flow diagram where the SAFT surface images, from which the surface profiles were found, were built to have 10 pixels per image millimeter of the image generating a grid of 320×50 pixels. The height of this imaging volume was selected as 5 mm, to enclose the entire span of the tyre/WAAM interface, where the surface profile was expected to exist. The final adaptive TFM images were computed using 6 pixels per image millimeter, thus the verification sample was imaged using a grid of 192×90 pixels and the defective titanium wall was imaged using 120×60 pixels, optimized from coarser larger area scans.

The SAFT images were processed with consideration of constant longitudinal wave velocities of 2480 ms^{-1} for the delay-line and 1006 ms^{-1} for the rubber, both measured experimentally using the pulse-echo technique. Once the tyre/WAAM interface was identified via the SAFT algorithm, the ToF's through the three mediums were computed to construct the adaptive TFM images with the additional longitudinal velocity of the titanium (6100 ms^{-1}). The velocity values of titanium were found constant without significant variations after the measurements in pulse-echo mode at room temperature using single element transducers.

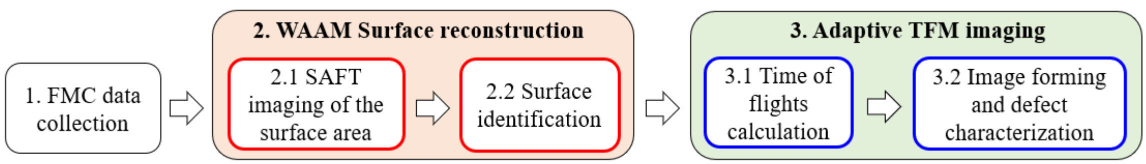

Figure 3.7 Diagram illustrating the SAFT surface finding and TFM imaging processing of the collected FMC data

3.4. Results and discussion

3.4.1. Inspection of WAAM Calibration Block with Artificial Defects

Initial experimental verification of the proposed imaging approach was conducted on a Ti-6V-4Al test specimen manufactured using the plasma arc WAAM process and oscillation deposition strategy. The sample was deposited, reaching a height of around

2.5 mm per layer with a width of approximately 35 mm. The 12.0 mm thick titanium plate was used as a substrate on which the sample was built. To introduce reflectors for the inspection, two artificial defects were fabricated in the form of Bottom-Drilled Holes (BDH) with diameters of 1.0 mm and 2.0 mm respectively, where the reflectors were drilled extending up by approximately 14 mm into the sample through the base plate, as shown in Figure 3.8.

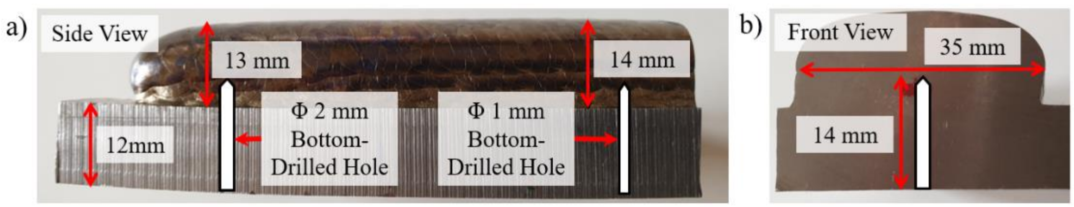

Figure 3.8 (a) Side view and (b) front view of a WAAM Ti-6Al-4V component deposited using oscillation strategy and containing fabricated calibration bottom-drilled holes of 1 mm and 2 mm in diameter

3.4.2. Results of Surface Reconstruction

To validate and analyze the ability to reconstruct the surface using ultrasound waves during a roller-probe inspection, the FMC dataset corresponding to the sample with 2.0 mm BDH was chosen to be analyzed. For the SAFT processes used in this work, the SAFT images were calculated using an angle limitation $\alpha = -7.5^{\circ}$ at reception. This limit was found to be the most accurate during initial trials. The image dB scale was set to 0 to -30 to best visualize individual features of the image without background noise disturbance.

A distinguishable presence of the contour of the WAAM surface (dashed green box) was observed on the SAFT image in Figure 3.9 (a). Furthermore, a strong signal indicating the end of the coupling area between the roller-probe's tyre and the WAAM surface (*i.e.*, decoupling points) are also visible and marked (dashed red box). Below the surface contour in the image, the repeated signal of the tyre/sample interface can also be seen (dashed yellow box).

Prior to proceeding to the WAAM surface finding stage, the decoupling points, where the roller-probe is no longer in contact with WAAM, were necessary to be recognized. The coupled width of the tyre/WAAM interface was measured to be around 30 mm, obtained from measuring the distance between the decoupling points and used to determine the maximum length over which the curve fitting was done.

Signal amplitudes found to be lower than -10 dB of the maximum image amplitude were then filtered to remove any background noise from the image volume. Owing to the thresholding, the image pixels with the strongest signal amplitudes were successfully identified and a curve was fitted through them to represent the WAAM surface, as shown in Figure 3.9 (b). The SAFT surface finding performance was evaluated by comparing the reconstructed surface against surface profiles obtained via a non-contact metrology laser scan with a y-axis resolution of 12 µm [86] (Figure 3.9 (c)). The total number of surface points along the x-axis for the surface profile reconstructed by the laser was 300, giving a dense spatial sampling of 0.1 mm. To measure the discrepancy, the average error between the two profiles was calculated through:

$$\Delta_{average} = \frac{1}{k} \sum_{k=1}^{k=n} |Y_{True}^{k} - Y_{UT}^{k}| \qquad (3.8)$$

where *n* is the total number of points used in the curve fitting (*n*= 300), *k* is the point number along the *x*-axis of both the true surface profile and the SAFT estimated surface profile, and *Y* stands for the *y*-axis position of points. The calculation was only conducted within an *x*-axis interval where both surfaces exist. The average error between the profiles (visualized in Figure 3.9 (d)) was calculated using Equation 8 as 0.06 mm. It is worth noting, that given the phased array sampling frequency of 50 MHz and the longitudinal wave velocity of Ti-6V-4Al (velocity = 6100 ms^{-1}) results in a distance resolution of a minimum of 0.12 mm within the Ti-6Al-4V medium; double the developed SAFT surface reconstruction algorithm resolution.

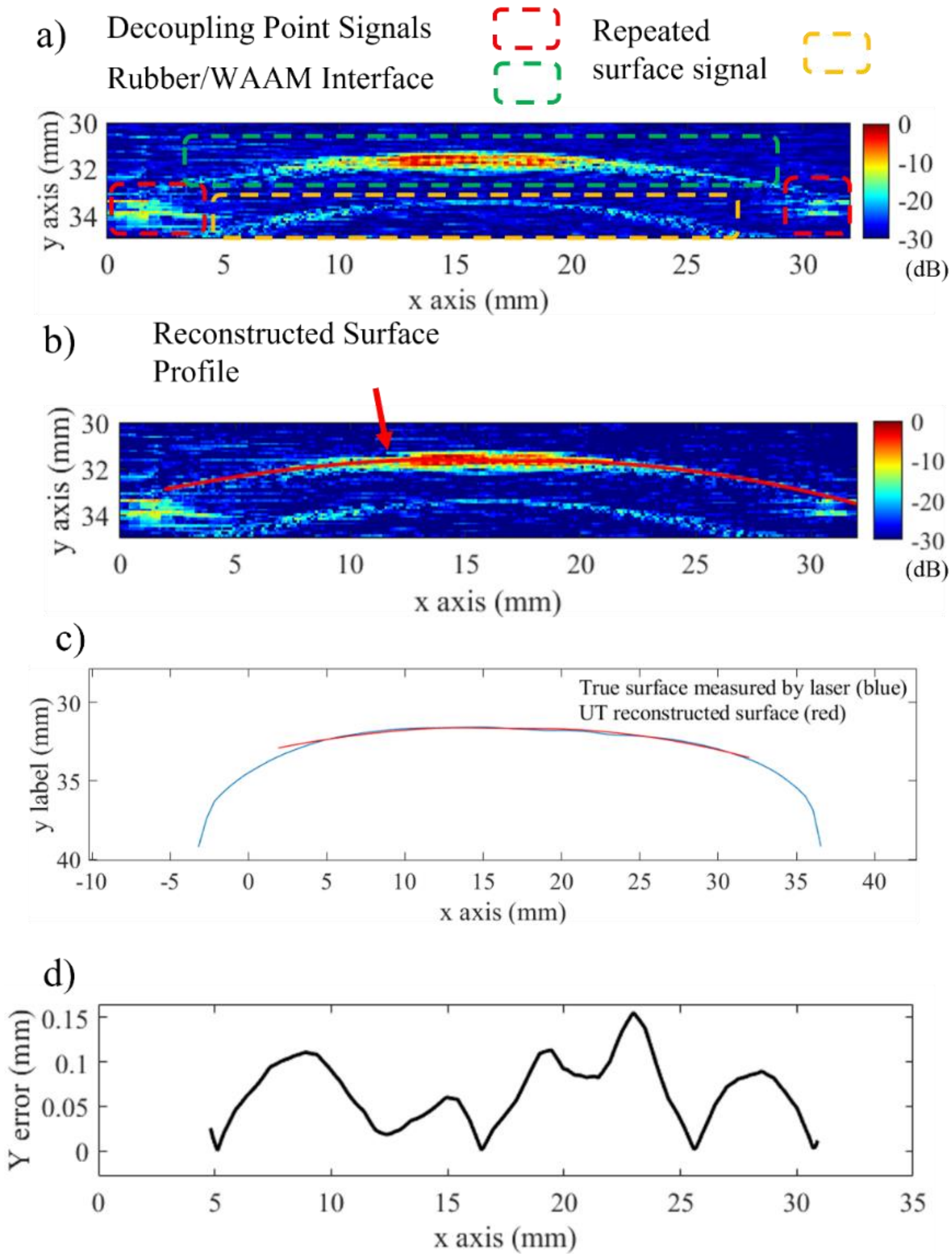

Figure 3.9 (a) An image of the WAAM surface formed using the dual-medium SAFT algorithm, (b) fitted curve to the extracted high-intensity surface points of the SAFT image after filtering and denoising, (c) comparison between the laser-scanned surface profile and the SAFT reconstructed profile, and (d) measured error between the surface profile acquired by laser and through SAFT reconstruction of the Ti-6Al-4V WAAM with bottom-drilled holes

To further evaluate the accuracy of the SAFT surface reconstruction and strengthen the confidence in the approach, the experiment was conducted on the machined mock-WAAM sample made of aluminum (Figure 3.10 (a)) [87]. The sample featured a characteristic semi-elliptical curve and a varying thickness (x-axis). The experiment was conducted at 3 locations along the sample to assess the accuracy of the surface reconstruction by comparison with the surface profile obtained by CAD. The results (Figure 3.10 (b)) showed that depside lower compliance of the roller-probe to the mock-WAAM sample, the algorithm was found sufficiently accurate to detect the location of the Tyre/WAAM interface and accurately reconstruct the polynomial curve.

Moreover, at the points where the coupling of the roller-probe with the sample co-existed the results of this experiment showed a possibility to detect a surface curvature with high accuracy and a total average error of only 0.0401 mm across all measuring points (True surface – SAFT surface).

These findings complement the objectives of this research task, and further strengthened the confidence in the development of a well-suited technique to provide an interface for the reconstruction of the interior of the WAAM samples in the upcoming sections of this thesis.

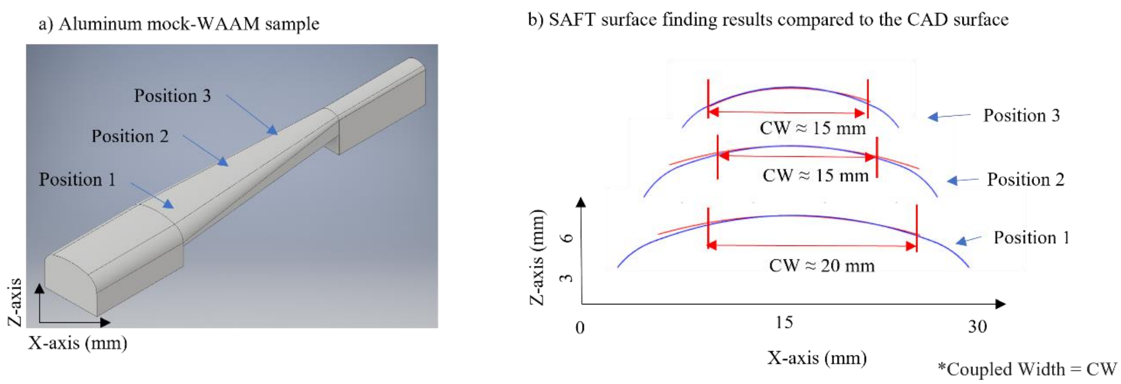

Figure 3.10 Additional surface reconstruction experiment on a) aluminium mock-WAAM sample with b) Results from SAFT surface finding compared to the CAD surface

3.4.3. TFM Image Reconstruction

Figure 3.11 depicts the results of the TFM imaging for the two BDHs in the Ti-6Al-4V WAAM sample, after incorporating the reconstructed WAAM surface profile estimated in Section 3.4.2. This figure displays the two imaged sections of the WAAM component located immediately beneath the roller-probe and the two BDHs. The TFM images reconstructed from this data are shown in the green box in Figures 3.10 (a) and (b) for BDHs of 2.0 mm and 1.0 mm, respectively. As seen in the presented figure, both, the 1.0 mm and 2.0 mm BHs defects were detected, and their indications were evident in the reconstructed adaptive TFM images. To facilitate the visual detectability of the defects, the area in the close vicinity of the defect was windowed to exclude the surface signal and its effect from the computation.

In order to size and characterize the defects, a horizontal line parallel to the *x*-axis and passing through the pixel with the highest defect signal was selected in each of the TFM images, and the pixel values along this line were plotted in Figure 3.12. The analysis was conducted using the -6 dB drop technique, recognized as a conventional flaw sizing methodology in ultrasound inspections [88]. This was achieved by superimposing a horizontal line through the intensity plots at a level where the amplitude reduces by 6dB from the maximum signal amplitude of the defect and measuring the distance between the intersection points. The lengths measured were 1.3 mm and 1.9 mm for 1.0mm and 2.0 mm defects, respectively.

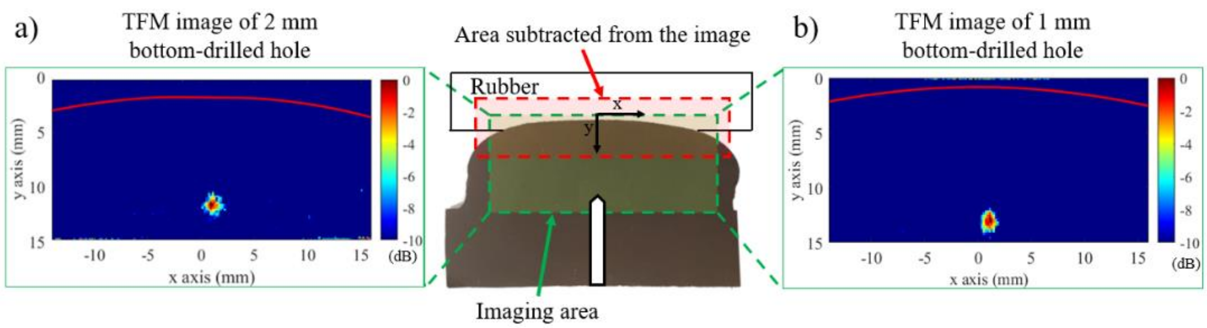

Figure 3.11 TFM image reconstructions for bottom-drilled holes of: (a) 2 mm, and (b) 1 mm in diameter inside a Ti-6Al-4V WAAM component

For the images in Figure 3.11, SNR was calculated to assess the overall image quality and detection capability of the inspection configuration. To this end, the root-mean-square of the noise data presented in the plots of Figure 3.11, excluding the signal of the defect, was calculated to indicate the noise level. Subsequently, the SNR was obtained as the ratio of the maximum defect amplitude to the average noise level. In this experiment, the SNR of at least 15 dB was achieved for the smallest defect.

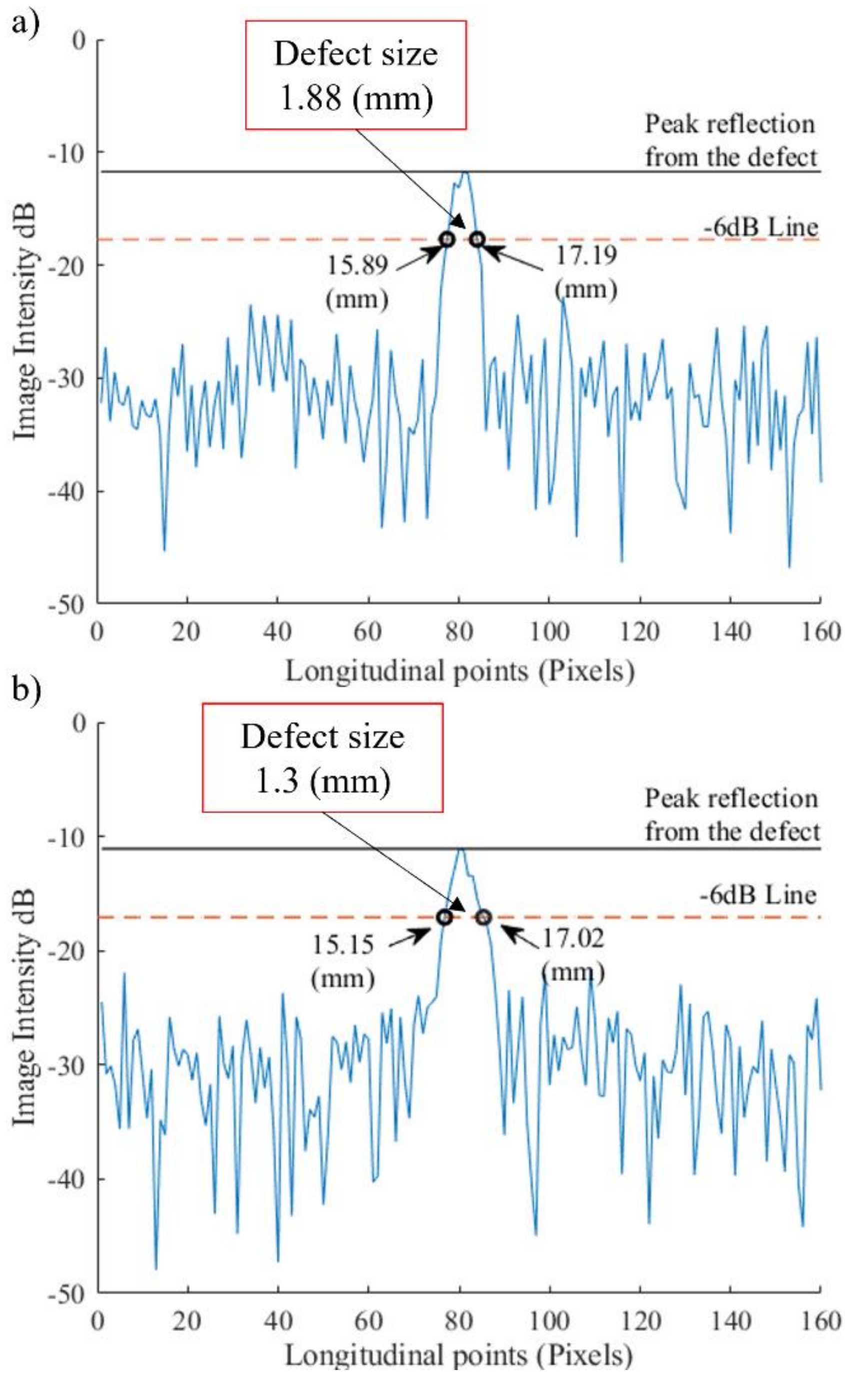

Figure 3.12 Pixel intensity values plotted alongside horizontal lines at -6 dB of the maximum image amplitudes passing through the maximum signals of a) 2 mm and b) 1 mm defects to size defects indications

3.4.4. Inspection of WAAM Titanium Wall with Real Lack of Fusion Defects

After successful verification on the above sample with artificial defects, experiments were also carried out on a Ti-6Al-4V WAAM wall (Figure 3.13), deposited with an oscillation strategy containing intentionally induced defects. The component (300 × 45 × 25 mm (L × H × W)) had intentional LoF defects introduced during the process at layer 6, located approximately 30 mm high from the baseplate, by lowering the arc current from 100% to 70% and increasing the travel speed from 100% to 125%. For the subsequent layer, the welding current was set back to 100% again, but the travel and the wire feeding speeds were lowered from 100% to 70% to restore the morphology of the previous defective layer. This process was important to smoothen the discontinuities achieved within the previous layer and to maintain the desired shape of the final component, however, despite the repair process employed, some LoF defects were expected to be produced within the built volume. To verify the existence of these defects, reference XCT tests were conducted using a Nikon XT H 225/320 LC X-ray computer tomography system fitted with a 225kV X-ray source. A maximum resolution of 100 µm was achieved, given the dimensions of the Ti-6Al-4V component, its placement within the XCT chamber, and its distance from the X-ray source. The wall was then inspected using the PAUT roller-probe and FMC data collected to compare with the XCT data.

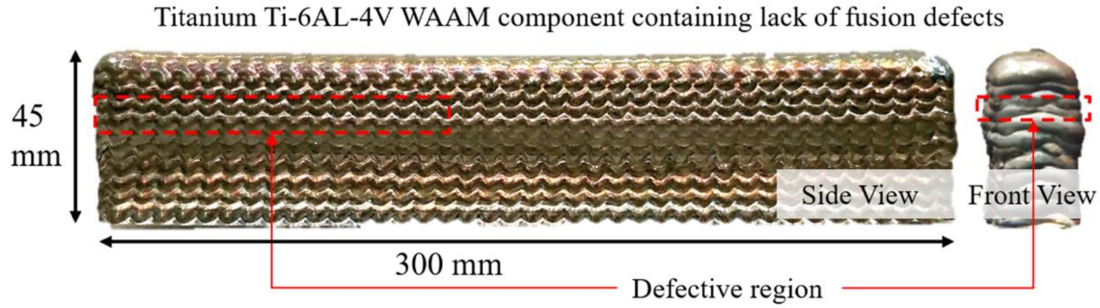

Figure 3.13 Ti-6Al-4V WAAM specimen deposited by oscillation strategy and containing process-induced intentional deposition lack of fusion defects spread over the marked area

3.4.5. Results of Surface Reconstruction

The FMC dataset from a single inspection frame acquired was also analyzed using the SAFT algorithm to generate the surface contour and the results are presented in Figure 14. A strong indication of the WAAM surface, as well as reflections of the decoupling points, were clearly distinguishable (Figure 3.14 (a)). Subsequently, the same approach is presented in Section 3.4.2. for the SAFT images, the width of the contact area was determined (approximately 15 mm), and the image was filtered for amplitudes lower than -10 dB from maximum, below which background noise would interfere with the curve reconstruction. The curve, depicted in Figure 3.14 (b), was stored in 4th order polynomial, similarly to in the first inspection scenario.

Again, the SAFT surface finding performance was evaluated by comparing the reconstructed surface against surface profiles obtained via a non-contact metrology laser scan [86] and the average surface error, presented in Figure 3.14 (c), was calculated to be 0.04 mm. Moreover, it can be seen in Figure 3.14 (d) that a lower surface mismatch was observed at the center of the two profiles where the tyre was fully coupled to the peak of the WAAM surface. This may indicate the better performance of the algorithm for the surface points closer to the center of the array. Despite the error value continuing to grow towards the corners of the WAAM, reaching up to 0.09 mm, it was still much smaller than the ultrasound spatial resolution permissible at the fixed sampling frequency.

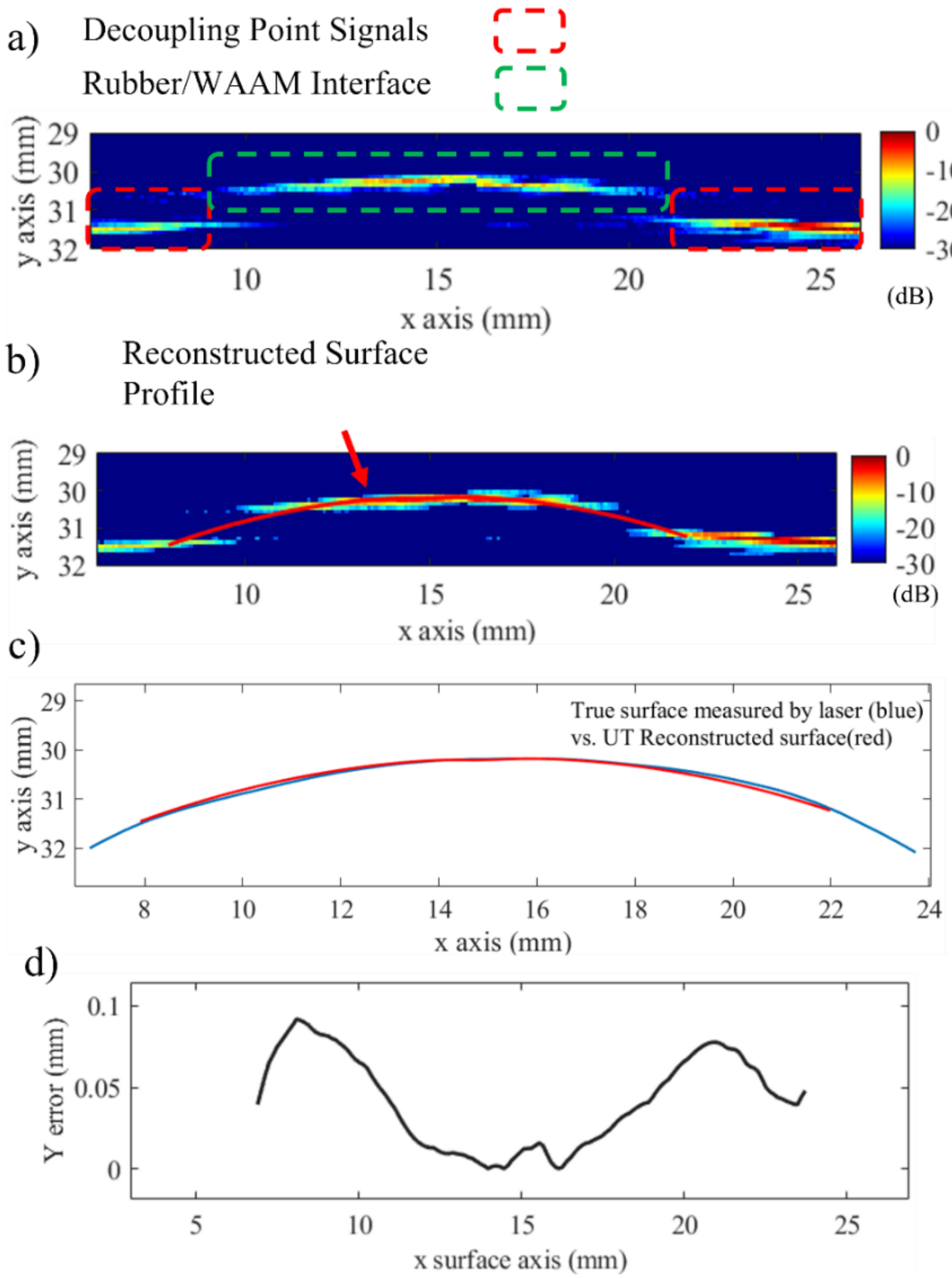

Figure 3.14 (a) An image of the WAAM surface formed using the dual-medium SAFT algorithm, (b) fitted curve to the extracted high-intensity surface points of the SAFT image after filtering and denoising, (c) comparison between the laser-scanned surface profile and the SAFT reconstructed profile, and (d) measured error between the surface profile acquired by laser and through SAFT reconstruction of the Ti-6Al-4V WAAM with intentional defects

3.4.6. TFM Image Reconstruction

Figure 3.15 (a) shows three inspection positions (TFM frames), appropriately aligned to their corresponding areas with induced process-driven defects and which possessed the highest signal amplitude in the acquired ultrasonic data stream. The surface profiles were calculated at these points and the TFM images were computed for a rectangular area of 10 mm by 20 mm across the *y* and *x*-axes, respectively. The images were normalized by the maximum signal amplitude and plotted on a 10 dB scale in Figure 3.15.

Figures 3.15 (b), (c), and (d) depict that the ultrasonically obtained proofs of these three LoF defects, located at different positions along the Ti-6Al-4V WAAM wall were visually detectable in the presented TFM images. A full 3D model of the WAAM component was reconstructed from the XCT images. The model was then sliced at the corresponding TFM image location along the z-axis, and a 2D grayscale representation of the defect was processed and presented. The TFM results were, then, compared with those obtained from the XCT analysis in the same location within the built volume of WAAM. To facilitate the readability of the results, the TFM images corresponding to each of the defects on the XCT image frames were presented in a green rectangular box beside their XCT image counterpart. The dimensions of the targeted defects, analyzed in this work, were measured from the XCT images to be in the average of 5 × 0.5 × 0.5 mm (W × H × L). The SNR of the images was evaluated to be approximately 10 dB which is deemed acceptable, given the coupling method, surface profile and attenuation within the roller-probe's tyre. Moreover, it is important to mention that the defects themselves were not simple cavities, such as artificially drilled holes. The defect found within this WAAM wall are fragmented, varying in shape and thus, the signal retrieved must therefore be considered adequate. In terms of the position of the defects within a WAAM, satisfying agreement was found for the depth and the horizontal position of the defects measured from the TFM images when compared to those from the XCT images.

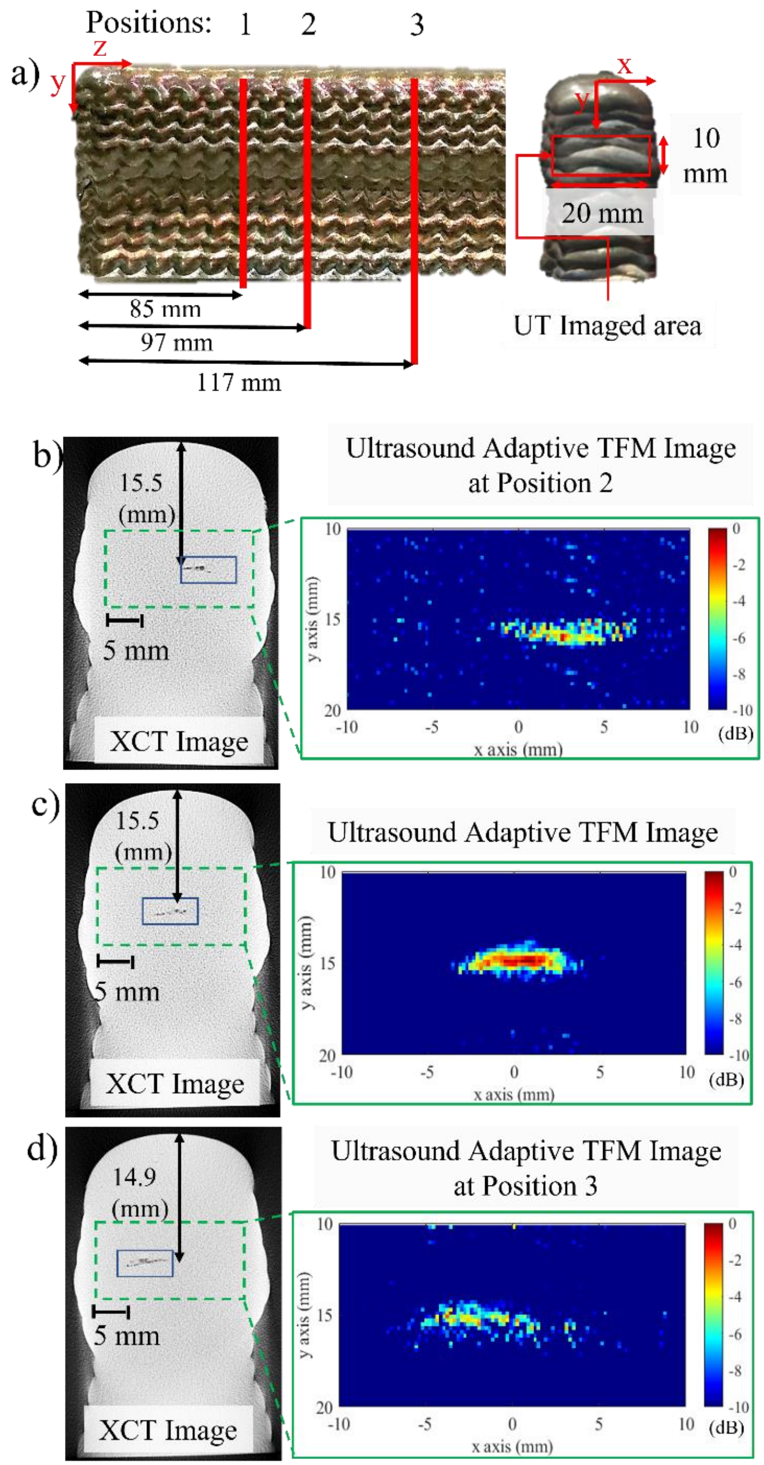

Figure 3.15 Roller-probe Ti-6Al-4V WAAM inspection positions where FMC data sets were collected, and a comparison between the results of adaptive TFM imaging and those obtained by XCT tests for the defects at positions (b) 1, (c) 2, and (d) 3

3.4.7. Automated As-built WAAM Components Ultrasonic Volumetric Coverage Considerations

One further advantage of the DAS TFM algorithm proposed in this study can be summarized by acknowledgment of the ray-tracing example path presented for the last element of the array in Figure 3.16. As the Figure suggests, the waves emitted by the array elements located at the corners of the active aperture have a contribution to the final TFM image. This is particularly compelling when tracing the ray from element 64 to the lateral pixels (Figure 3.16 (a)) and bottom pixels located 40 mm inside the sample (Figure 3.16 (b)), showing that the refraction angles across the interfaces facilitate for the rays to arrive these image pixels. This observation emphasizes that despite the not very large contact area produced between the rubber tyre and WAAM surface, the natural as-built component surface convexity works in advantage of the raytracing approach allowing for the WAAM internal structure to be accessible by the ultrasound energy, even if it is generated by the corner elements. One distinct benefit of this imaging method is in that it allows inspection of a wider area than the coupled surface without the otherwise necessary reduction of the number of contributing n^2 elements and therefore employing the whole FMC dataset. The high acoustic mismatch between the tyre rubber (1.12 MRayls) and Ti-6Al-4V WAAM (27.48 MRayls) components guides the high refraction angles; therefore, redirecting the ultrasound pulse toward the corners of the test piece. However, it should be noted that the large acoustic mismatch also negatively impacts the signal amplitude transmitted into the component by increasing the reflected wave energy at the interface of the rubber tyre and WAAM surface.

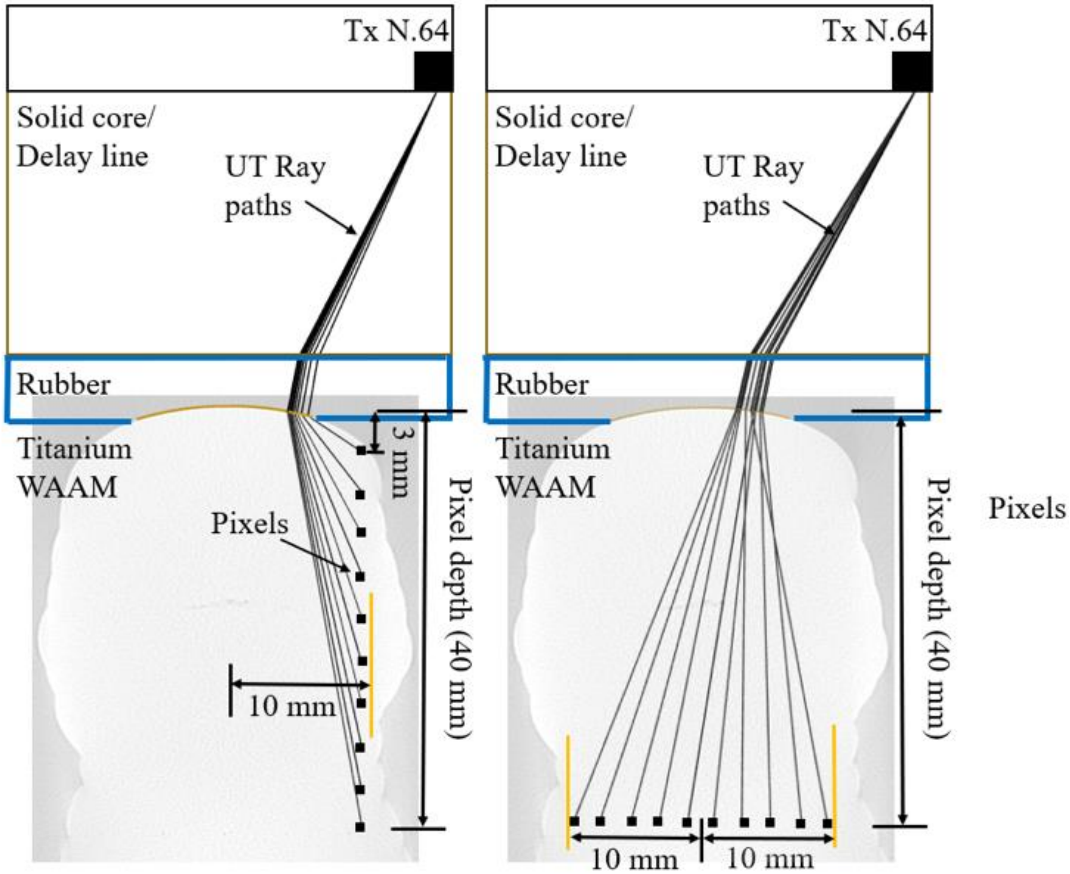

Figure 3.16 Ray-tracing from corner element number 64 to the TFM image (a) lateral pixels extending from 3 mm to 40 mm below the WAAM surface, and (b) bottom pixels at the depth of 40 mm spread across the width of the Ti-6Al-4V WAAM component

3.5. Summary of the Chapter

This chapter presented the concept of a three-layer adaptive ultrasound TFM imaging algorithm for the NDE of WAAM components. This was achieved from their non-planar as-built surface, removing the requirement for a post-manufacturing machining processing. An integrated SAFT-based imaging algorithm detects the as-built surface and interfaces when using the novel ultrasound dry-coupled WAAM roller-probe. The benefits and performance of the inspection approach were demonstrated on two varying

Ti-6Al-4V WAAM components, one with bottom drilled holes of 2 mm and 1 mm in the diameter and the other containing intentionally induced LoF defects as small as 5 × 0.5 × 0.5 mm (H × W × L). The following summarizes developments and the conclusions of this chapter:

- Employing the collected FMC data, the as-built non-planar tyre/WAAM interface was detected using the SAFT algorithm. Because of the distinct surface profiles visible on the SAFT images, an automated surface finding approach based on thresholding and curve fitting was able to be included, allowing precise reconstruction of the WAAM surface curvature.
- The SAFT surface finding of the as-built WAAM component was compared with a reference scan produced using a non-contact metrology laser scan and the average relative error was found to be as low as 0.04 mm.
- The ultrasonic reconstruction of the non-planar as-built surface geometry of WAAM components and ToFs of the ultrasonic rays propagating between the array and every pixel of the image was computed accounting for refractions at two interfaces existing between delay-line/rubber tyre and rubber tyre /WAAM sample.
- Despite the limited contact area of as low as 15 mm between the rubber tyre and the WAAM surface, the ray-tracing algorithm demonstrated the advantages of the approach. When using the roller-probe on WAAM walls, the coverage of interior volume, even by corner elements, was achieved.

- A fully focused image of Ti-6Al-4V WAAM, with BDHs and LoF defects induced at selected locations inside the WAAM components, was produced and formed using the adaptive TFM algorithm. The defects were detected with an SNR greater than 10dB.
- The formed TFM images of the real induced LoF defects were analyzed by comparison to the XCT results. A strong agreement between the results was observed in terms of the defect location and extension, confirming the competency of the novel imaging approach.

Chapter 4

Collaborative sensor-enabled cell for Wire + Arc Additive Manufacture and Ultrasound NDE

4.1. Introduction

The detection of defects, in-process, during WAAM manufacture, unlocks the possibility of real-time and rapid restoration work or alternative prompt scrapping of the defective part, saving the manufacturer from time-taking deposition of costly material over defective layers. Moreover, the deployment of automated inspection approaches offers greater advantages such as much higher positional accuracy, repeatability, and high rates of inspection as compared to manual practices performed by trained human operators [89].

Recently published research has presented important and valuable advancements in the field of automated in-process NDE of arc-based welding processes [13, 17, 46], in which the detection of defects in-situ was achieved. It is worth noting, that robotic welding is a manufacturing method with similar applicable attributes and challenges to WAAM such as the high temperature of contact surfaces, high level of automation and it is a hazardous environment for human operators. The development of a multi-robot welding cell demonstrated the possibility of integrating robotic welding and automated ultrasound NDE [16]. Full automation was accomplished by a novel sensor-enabled robotic system based around a real-time embedded controller which enabled: a) real-time communication between different hardware, b) data acquisition from all sensors and c) full control of the processes occurring within the cell. Furthermore, sensor-based motion corrections were accomplished by the communication protocol established through the Robot System Interface (RSI) [90], created by industrial robot manufacturer KUKA, enabling an impact of the sensor on a pre-programmed robot's path. The motion corrections were executed through a sensor input in real-time intervals (4 milliseconds intervals for KUKA robot Controller (KRC) 4). This opened an opportunity to pre-define the robot's target pose and pose corrections through the program based on environments e.g., LabVIEW, MATLAB, or Python and direct these updates to the robot via ethernet connection. Therefore, it was made possible to employ the multi-robot cell for automated ultrasound NDE inspection: I) post-process continuous inspection (for example: repeated for 96 hours assessing cracks while creation), II) inter-pass in-process inspection between layers (beads) or III) live-arc in-process inspection.

Furthermore, the deployment of the Force-Torque (FT) sensor-driven robotic motion for automated NDE of geometrically complex and unpredictable geometries was explored in [79]. The FT sensor supported the inspection by facilitating the robot’s path correction necessary for contact-based inspection of the aircraft wing cover with a surface geometry that was inconsistent with the geometry obtained from the original CAD model. Therefore, the presented research dealt with indistinguishable automation challenges, associated with transducer deployment on the approximate pre-programmed path, which was applicable to possible automated NDE deployment on near net-shaped WAAM presented throughout this thesis.

The previous chapter (Chapter 3) described the ultrasound NDE approach enabling accurate imaging of WAAM components through their as-built surfaces using a novel roller-probe. However, the research has only been presented on the static inspection of the components in experiments and has not yet been deployed on as-deposited hot WAAM components. To enable this possibility, such a manufacturing environment supporting in-process NDE must be developed.

Therefore, this chapter aims to present a novel concept of the multi-robot cell developed and designed for WAAM part building and automated in-process NDE using a novel dry-coupled high-temperature ultrasonic WAAM roller-probe. Figure 4.1 shows a process conducted in the cell, where at first, the plasma-arc WAAM process is employed and controlled by the deposition software while a full external control of the NDE process is achieved by the sensor-enabled adaptive kinematics control package adapted to in-process WAAM NDE. The automated high-temperature WAAM roller-probe is deployed within a dwell time, set for inter-layer cooling as depicted on the diagram (Figure 4.1). The sufficient contact with the as-built surface of WAAM during the inspection is assured by the FT sensor.

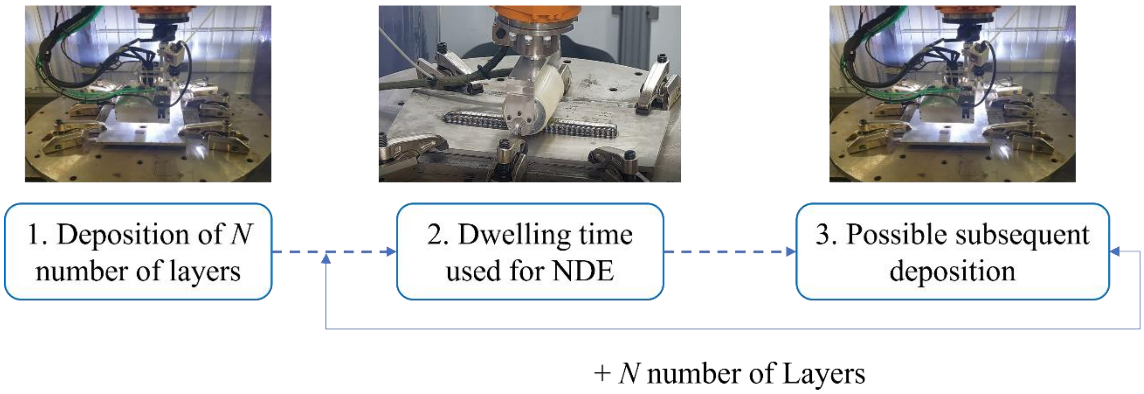

Figure 4.1Diagram showing the process of WAAM deposition and in-process NDE

In this in-process NDE performance demonstration, a Ti-6Al-4V WAAM wall with embedded tungsten reflectors is deposited to evaluate the performance of the in-process NDE approach. The use of tungsten tubes as artificial reflectors for ultrasound inspection technique calibration and evaluation has found its application in the fields of in-process welding inspection [13, 17] as well as ultrasound inspection of WAAM [53]. An advantage of the tungsten can be realized by the possibility to manufacture inclusions with known sizes, shapes, and at the desired location. During the in-process NDE, the position encoded FMC data are acquired using a high-speed ultrasound phased array controller. The SAFT-TFM package, presented in Chapter 3, enables the highly accurate detection of artificial reflectors presented on an amplitude C-Scan image of the WAAM component's interior.

Hence, this chapter directly supports industry-oriented research on manufacturing first-time-right AM components.

4.2. WAAM + NDT Cell Concept

4.2.1. Hardware

The automated robotic WAAM and NDE system featured in Figure 4.2 was designed to employ 2 x 6 Degrees of Freedom (DoF) industrial robotic manipulators (KR90 R3100, KUKA), utilized for the WAAM deposition process and the in-process NDE. Moreover, as an integral part of the WAAM deposition robot, a horizontal rotary positioner (DKP-400V3, KUKA) was also positioned within this cell as a rotational tooling mainframe and a clamping mechanism for substrate plates on which the WAAM wall is built. The deposition hardware, physically mounted on a deposition robot's end-effector, featured a water-cooled plasma-arc welding torch, powered by an EWM-TETRIX 552 AC/DC SYNERGIC PLASMA power source, fitted inside the deposition device (head) with a local shielding [6], as seen in Figure 4.2 (a). The local shielding device was an aluminum box-shaped enclosure with multiple gas outlet channels fitted, that provide a continuous supply of argon shielding gas to the deposited WAAM surface just after solidification of the material, preventing atmospheric contamination that would lead to oxidation of the freshly deposited component. Further, a wire-feed mechanism with adjustable height was fitted on the deposition device, positioned to supply wire feedstock into the melt pool. The wire supply was controlled by an automatic wire feeder (EWM T drive 4 Rob 3 Li, EWM) that was mounted directly to the deposition robot's arm as well. Finally, the deposition head was equipped with a welding camera (Xiris XVC-1000) used to remotely assess the deposition quality and adjust welding parameters in real-time.

An inspection robot, seen in Figure 4.2 (b) was equipped with an FT sensor (FTN-GAMMA-IP65 SI-130-10, Schunk) mounted on the end effector. A WAAM roller-probe was, then, attached to an FT sensor serving as an extended robot's end effector. The roller-probe was driven by a high-speed phased array ultrasound controller LTPA (PEAK, NDT) mounted directly on the robot arm. Further, communication between all inspection hardware was accomplished by a network switch (Zyxel Gigabit ethernet switch) enabling control of the WAAM process and NDE via a single ethernet connection plugged into the PC.

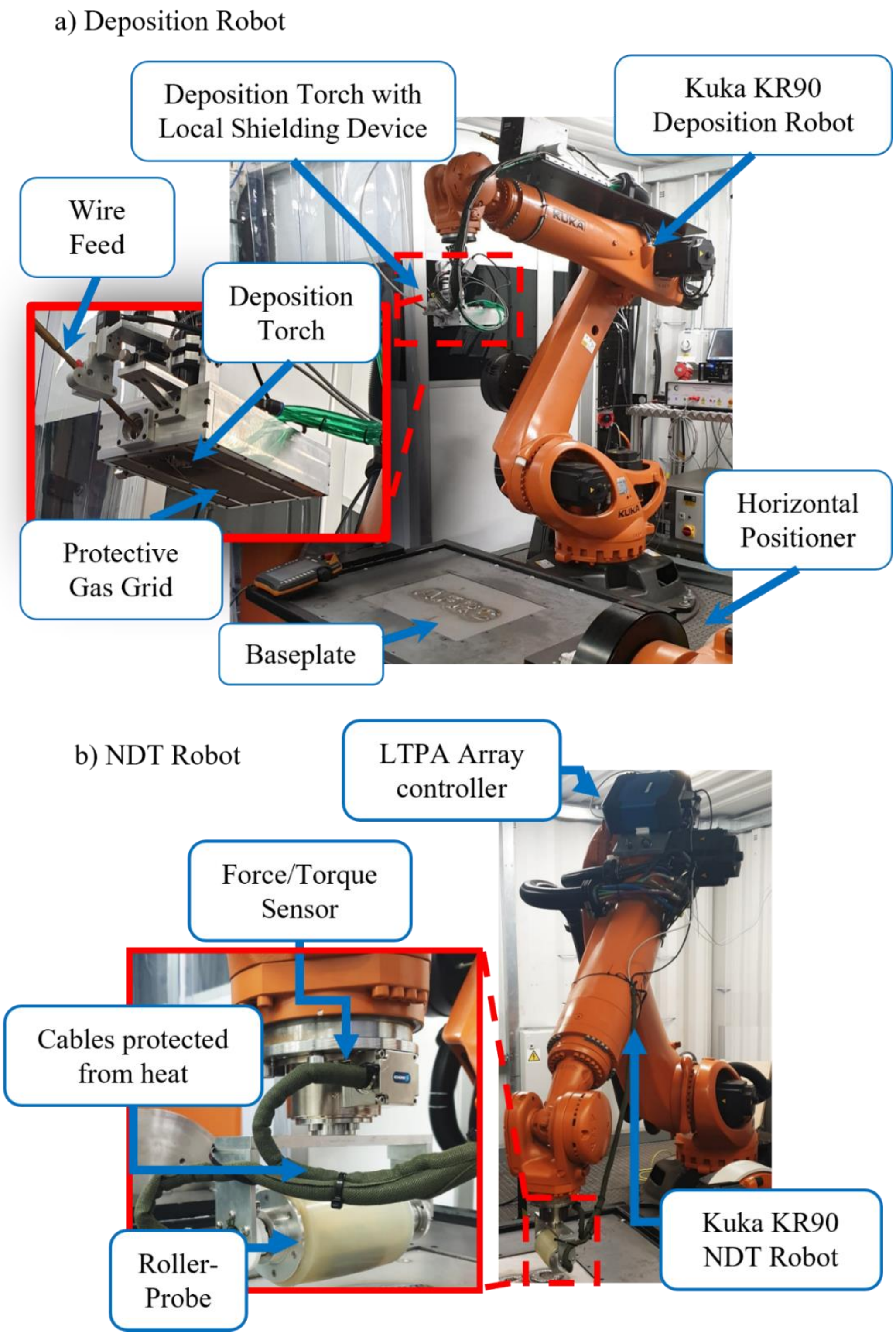

Figure 4.2 Implemented (a) WAAM deposition cell with plasma arc process, and (b) roller-probe based NDT

4.2.2. Software setup

4.2.2.1. Deposition

For this research work, the deposition robot was controlled by WAAMCtrl (WAAM3D, UK) [91] software, streaming the deposition commands (robot paths, deposition parameters) directly to the deposition robot via RSI over an ethernet connection. The tool-path plan was produced using WAAMPlanner Software (WAAM3D, UK) [92], in which the desired component was imported as a CAD, sliced into a set of layers based on the pre-defined layer height, given by the process. The part was then segmented into a set of individual building blocks from which the series of toolpaths were generated. Depending on the variables, such as material, geometry or deposition process, the deposition parameters were given to a WAAMPlanner and the post-processed file was generated, translating the information to a ready-to-stream ".xml" file.

4.2.2.2. NDE Software

The NDE inspection was driven by a software platform developed in the LabVIEW environment [93], which is a tool that enables prototyping using a wide range of tools and software libraries. The Graphic User Interface (GUI), presented in Figure 4.3, was designed as a set of parallel state machines responsible for executing the program in sequence controlling the inspection robot, FT sensor and ultrasound data acquisition in real-time.

The linear robot motion and control used for the in-process NDE work were based on a robotic platform described in [16] and developed for in-process inspection and automated

NDE purposes. During the in-process inspection, real-time adjustments of the inspection robot velocity, acceleration and contact force were enabled for the operator. Position-determined triggers were embedded in the program, enabling automatic and independent approach/retraction and inspection travel speeds. Further, these triggers enabled/disabled the FT sensor-driven motion when needed as well. The Z-axis force controller was used to maintain sufficient contact between the roller-probe and WAAM, while the operator maintained the ability of real-time adjustments.

In this thesis, the Z-axis motion corrections, associated with maintaining a steady force at speed, were calculated by the KRC based on the RSI configuration diagram. The control over the X, Y, A, B and C -axis always remains influenced by the predetermined path planning, while the appropriate motion corrections were calculated within LabVIEW in real-time (every 4 milliseconds) and streamed through the RSI.

Further, taking advantage of the real-time communication with the inspection robot, the position of the inspection robot during an inspection was encoded to each FMC frame acquired. The FMC data were then processed within a MATLAB environment, processed using a SAFT-TFM algorithm package, enabling to obtain positionally accurate results.

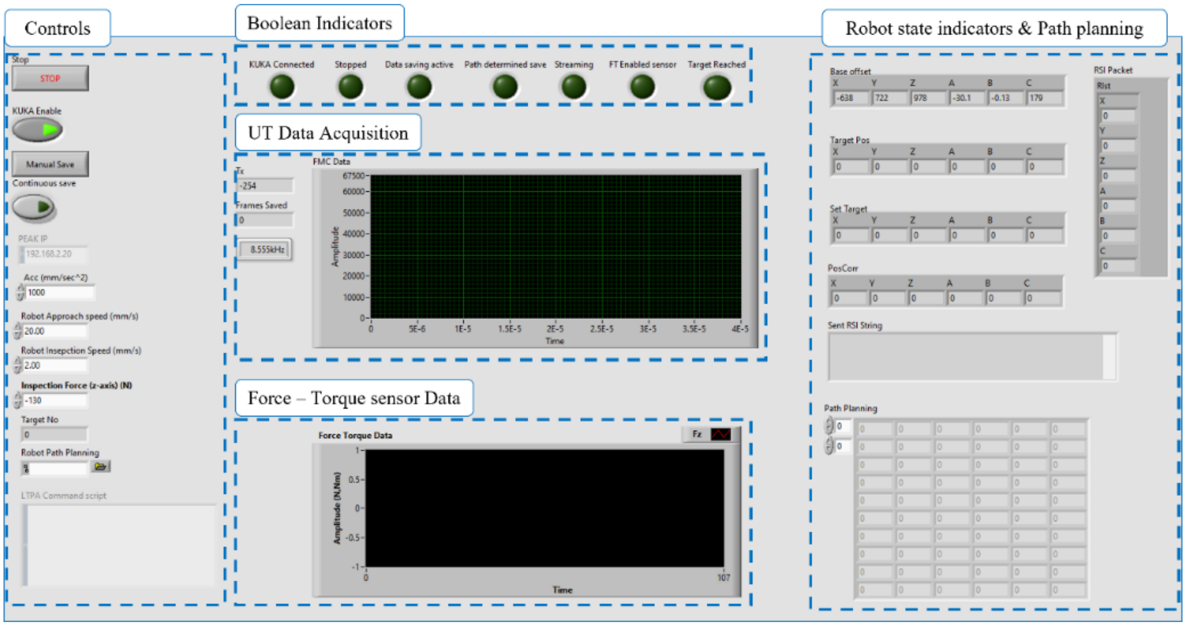

Figure 4.3 LabVIEW GUI for NDE process control and monitoring

4.3. Experimental WAAM Manufacturing

4.3.1. WAAM Path Planning & Deposition Parameters

To demonstrate the capabilities of the WAAM and NDE cell concept, and evaluate its performance in practice, a simple design for a Titanium (Ti-6Al-4V) WAAM component was selected and prepared for fabrication. The experimental WAAM wall was designed to be 300.0 mm in length, 25.0 mm wide and a height of 25.0 mm. However, given the nature of the WAAM process delivering near-net-shape components [4], extra overbuilt material was to be expected. The height of the wall was not considered critically important since the main objective of this work was to evaluate the inspection of WAAM's interior with a specific volume. Therefore, the built process was terminated when the hypothetical component was found sufficiently high for the in-process NDE demonstration to be performed.

The path planning designed in WAAMPlanner, seen in Figure 4.4 below, depicts an oscillating deposition strategy [94], where a single bead, with a zig-zag square pattern, was deposited per each layer of the component. Deposition parameters imported to WAAMPlanner, relevant to this work, can be seen in Table 4.1 below.

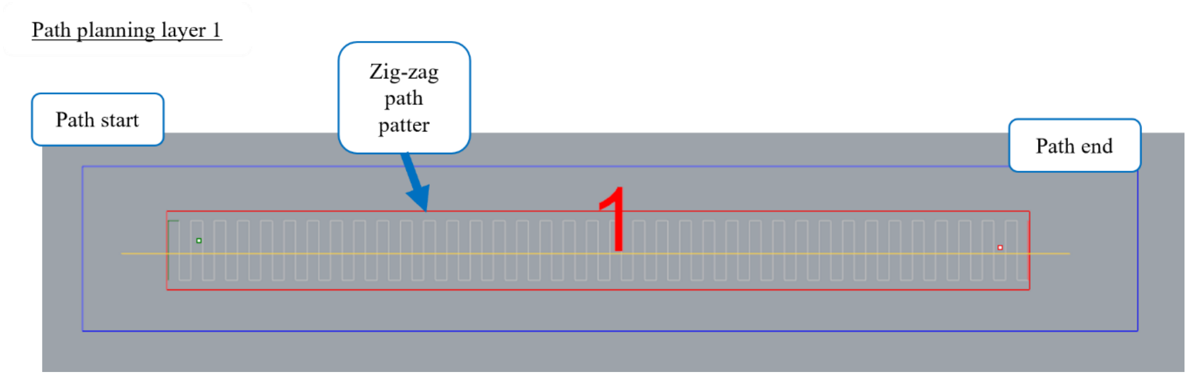

Figure 4.4 Deposition path planning for layer 1 of an experimental WAAM wall

Table 4.1 Deposition parameters

Deposition Parameters	
Current	150 Amps
Wire-feed speed	2.5 m/min
Robot Velocity	0.005 m/s

4.3.2. WAAM Deposition

Figure 4.5 (a) displays a WAAM deposition setup where an experimental straight WAAM wall was built on a Ti-6V-4Al substrate plate, 12.0 mm thick, clamped to the tooling which was mounted on a rotary table of the horizontal positioner. The substrate plate was clamped using welding clamps to prevent bending of the plate caused by heat-induced residual stress [95], commonly associated with arc-based manufacturing processes such as welding [96].

This clamping set-up has created a challenging and restricting working envelope; hence, the initial stage of the WAAM part fabrication was calibration and verification of the path motion by a dry run. At this step of WAAM part fabrication, the robots traveled through the planned deposition paths without an active torch or wire feed. Therefore, the correct positioning of the robot could be assured, knowing that the deposition head would not collide with the clamping. This was extremely important, especially during the deposition of the first few layers, after which the deposition head was high enough not to collide with welding clamps.

Figure 4.5 (b) shows an active deposition of the 1st layer, while the completed pass on the substrate plate is visible on the image (Figure 4.5 (a)). It is worth mentioning, that the height of the first layer was measured to be 3.5 mm.

a) Substrate plate clamping with 1st deposited layer

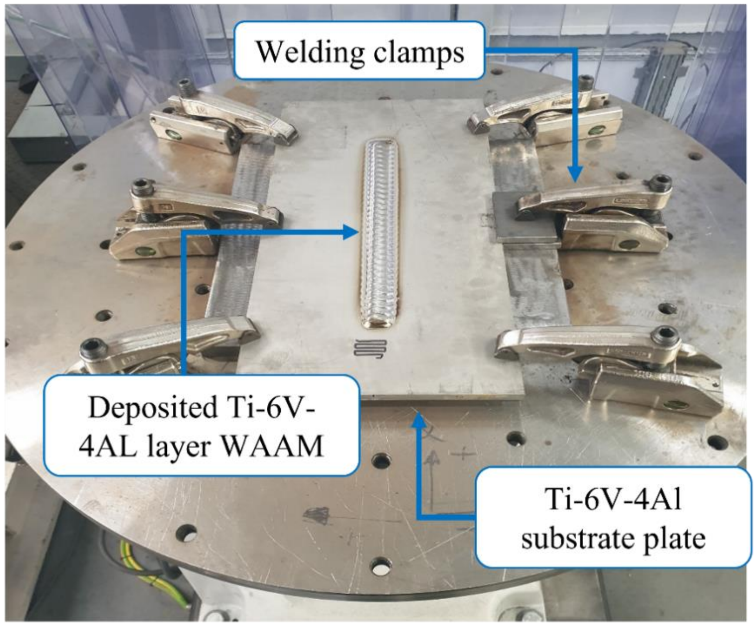

b) Active deposition

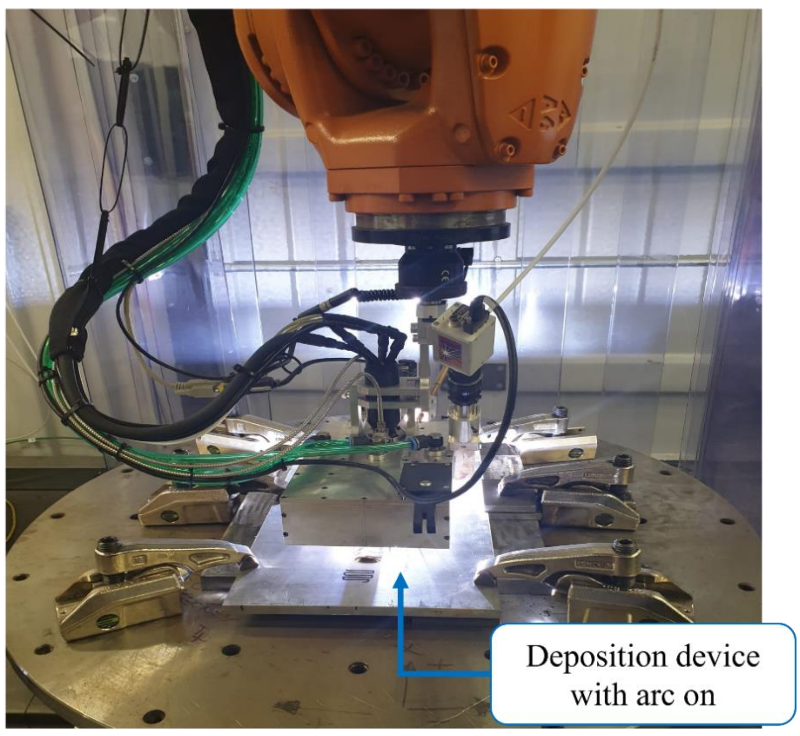

Figure 4.5 (a) Deposition clamping setup and a substrate plate with a deposited 1st layer and (b) deposition process with an active torch

4.3.3. Ultrasound Reflector Planting

To evaluate the in-process NDE defect detection capability, artificial reflectors were embedded into the experimental wall. In this work, tungsten tubes with parameters specified in Table 4.2, were utilized for this purpose. Two tubes were embedded into layer 3 by producing slots using a portable grinding machine. The tubes were located approximately 55 mm from each other. Tube 1 was placed parallel to the wall, in the approximate center of the bead. Tube 2, on the other hand, was embedded in the transverse direction to the wall as seen in Figure 4.6 (a).

Further, Figure 4.6 (b) depicts the wall after layer 4 where the tungsten rods were fully covered by the freshly deposited titanium. No inconsistencies in the surface quality that could cause a potential failure of the building process were observed once layer 4 was completed.

Table 4.2 Tungsten tube parameters

Tungsten tube		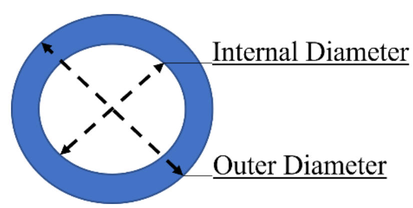
Tube length	30.0 mm	
Internal diameter	1.0 mm	
Outer diameter	3.0 mm	

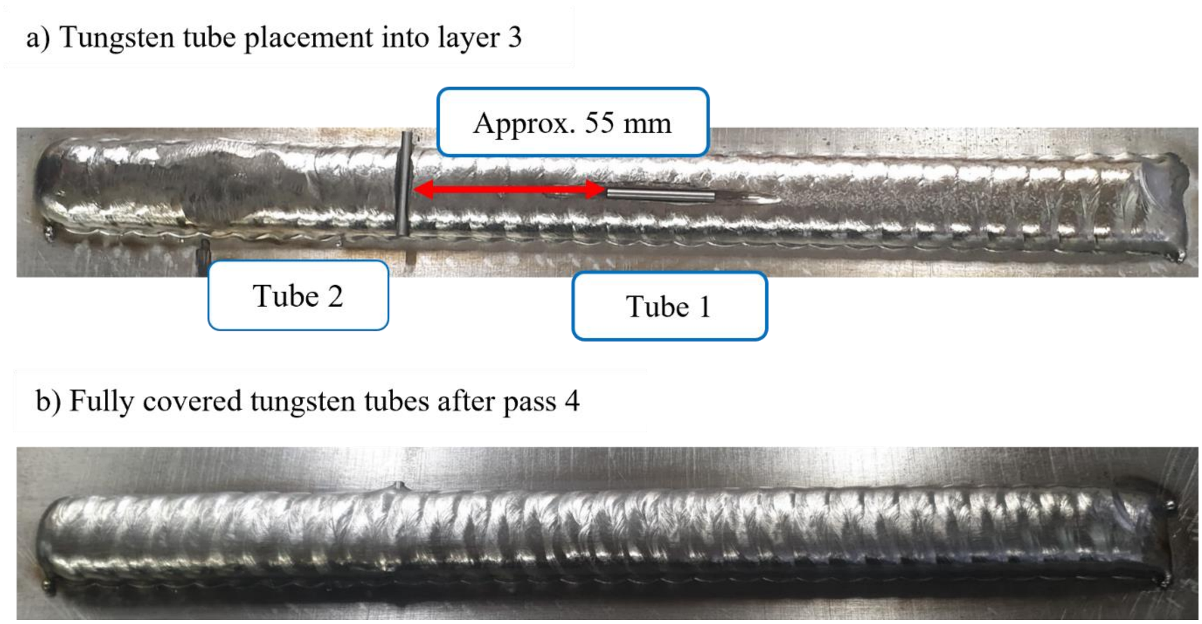

Figure 4.6 a) Tungsten tube embedding into layer 3 and b) subsequently deposited layer 4 covering tubes

4.4. In-process NDE of the Experimental WAAM Wall

4.4.1. Ultrasound Inspection Parameters

Ultrasound FMC data was acquired employing a WAAM roller-probe device featuring a 26 mm high solid delay line fully fixed as a core within the roller-probe. The rolling and contact with the sample were accomplished by a 6 mm thick silicone rubber tyre. The phased array transducer with parameters specified in Table 3.1, was mounted on the top of the delay line.

The FMC data collection was driven by an LTPA phased array controller with 200 V excitation voltage and a reception fixed hardware gain of 60 dB. The time-domain matrix of the A-scans was created by 3000 data samples for each transmit-receive pair at a sampling rate of 50 MHz. To accomplish a data post-processing, following acoustic velocities for longitudinal ultrasound waves were assumed for refraction and time-of-flight solving: I) Delay line = 2480 m/s, II) Rubber = 1006 m/s and III) titanium = 6200m/s. These acoustic velocities were obtained by conducting an ultrasound pulse-echo measurement where each of the roller-probe components (delay line and rubber) and the titanium sample were cut into a cube with dimensions of 10.0 mm.

The titanium cube was placed on the heating blanket and the measurement was performed by heating the cube to the temperatures ranging from room temperature (20 °C) to the temperature corresponding to the maximum temperature roller-probe can withstand (350°C). Once the steady temperature was achieved, an ultrasound A-scan sample was collected using a single element transducer coupled through the piece of high-temperature rubber. Given the surface temperature of 150 °C measured and averaged on the surface, using a hand-held thermometer during the robot's approach towards the sample, the acoustic velocity corresponding to this temperature was used for experimental image processing. It is worth noting, that a single velocity was used to process all FMC frames, given no information about temperatures at the point of data acquisition could be acquired. The thermal gradient compensation and calibration are, however, further discussed in the future work section and are proposed as a topic for upcoming research activities.

4.4.2. In-process NDE

The ultrasound in-process NDE capability was demonstrated by conducting an inspection after the completion of two subsequent layers from layer four which was deposited to cover and embed tungsten tubes. Thus, Figure 4.7 presents a finalized experimental wall that was subjected to the in-process NDE. The WAAM wall, after layer 6 was measured to be around 21 mm in height, 28 mm in width and length of 305 mm, with a layer height equal to approximately 3.5 mm.

Given the requirement to consider a hypothetical possible subsequent deposition to carry on with part building, the integration of the in-process NDE into the build-process by taking advantage of the dwell time was a must. Throughout the deposition of the experimental wall, presented in this work, a dwell time of 9 minutes was set to allow inter-pass cooling as suggested by [97], where optimal inter-pass cooling was investigated for Ti-6Al-4V WAAM built featuring a similar oscillation deposition strategy utilized in this demonstration and experiment. This time was set to avoid the formation of α_{GB} phase grain microstructure and, thus, achieve optimal mechanical properties of this hypothetical component. Moreover, this time was found sufficiently long for in-process NDE to be performed without causing costly delays in the hypothetical production process.

Before the initiation of the NDE, the surface temperature was taken using a handheld thermometer. The surface temperature of the WAAM was measured ranging between 150 - 200 °C along the wall, which was much lower than the operational limit of the roller-probe (resistant up to 350 °C).

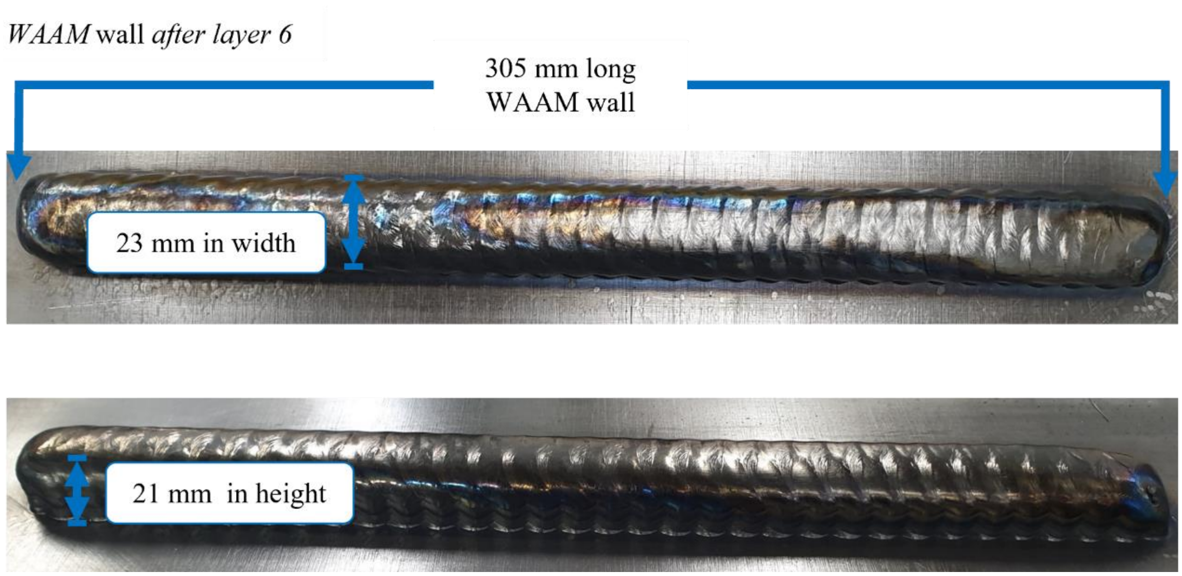

Figure 4.7 Fully completed experimental wall with dimension indications ready for NDE to be applied on

The NDE was commenced within the first 2 minutes of the deposition robot's return to its default home pose. Figure 4.8 presents a step-by-step inspection diagram, where at first, the inspection robot's end-effector approached the wall with a travel speed of 50 mm/s until the position 5.0 mm above the predicted as-built surface of WAAM was reached.

The second stage in the diagram shows a contact establishment with the WAAM specimen. This was accomplished by an automatic trigger that recognized the robot's position (5.0 mm above the expected surface), which was followed by a change of robot speed to an inspection speed (in this work = 2.0 mm/s) and initiation of FT sensor-driven motion. A command to maintain a constant force of 130 N was sent to the inspection robot from LabVIEW via RSI; thus, the Z-axis position correction was no longer managed by a LabVIEW motion framework, but the kinematics corrections were calculated and applied by the KRC. The force applied to the component was set to establish optimal coupling quality and prevent damaging the internal structure of the roller-probe. This was studied in previous experimentation during the roller-probe development stage.

During the descending of the inspection robot on the surface of WAAM, the LabVIEW program was set to wait for 2 seconds, before sending coordinates of the next position. This "wait" command enabled the inspection robot to position itself on the surface with the required set stable force and without further freedoms in the X-Y plane that could result in inconsistent contact with a specimen.

Stage 3 of the inspection was initiated by the LABVIEW program sending coordinates of the next target position (in this scenario = the end of an inspection, +300mm in the X-axis direction) to the inspection robot and enabling encoded FMC data acquisition at speed (2 mm/s). The FMC data was acquired while the inspection robot traveled along the path with a steady force by correcting its Z-axis position to maintain a given force value with the experimental wall.

Once the end of the path was reached, the termination of the inspection was triggered by the change of the inspection robot's Z-axis targeted position located 5.0 mm above the WAAM expected surface. This trigger sent a command to disable the sensor-driven motion and the ultrasound data acquisition. The process was concluded by retracting the inspection robot to its home position according to the path planning.

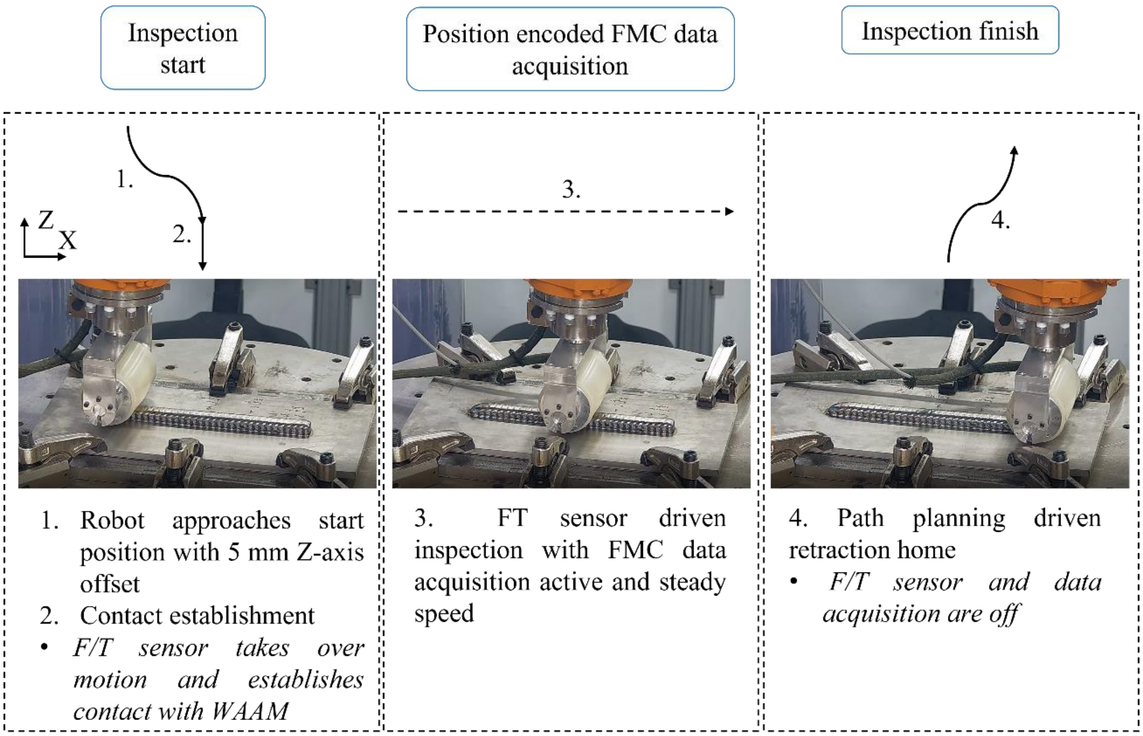

Figure 4.8 Inspection diagram showing a process of robot motion during the inspection

The inspection volume from the experimental wall was set to 300.0 mm, therefore the time elapsed to inspect the component equaled 150 seconds with an additional approximate 60 seconds that included the approach to the specimen and the robot retraction back to a home position. It is worth mentioning, that the entire inspection took significantly less time than set for a dwelling (9 minutes), which complemented the objectives required for in-process NDE of WAAM in this scenario. The total number of positions encoded FMC frames acquired was 200, giving a frame density of 1 per 1.5 mm (FMC sample rate of 0.75Hz).

4.4.3. Ultrasound Data Post-processing: TFM Imaging and C-scan

After the completion of in-process data acquisition, the ultrasound data collected during the inspection were processed using a SAFT-TFM algorithm described in Chapter 3. The TFM frames were computed for a 25.0 mm × 19.0 mm region at 6.0 pixels/mm resolution, which is compatible with the 2 dB amplitude fidelity criterion of ASME V [98]. This window represented an internal volume of the desired component between the baseplate and a region 2.0 mm beneath the surface or just above the interface of layers 5 and 6, where potential defects would be expected. Moreover, this work was focused on the detection of tungsten tubes, therefore there was no interest in detecting and analyzing possible generated true defects from the WAAM process.

To achieve a full C-scan, the computation was initiated by the ultrasound surface reconstruction using a SAFT surface imaging and surface finding algorithm. Afterward, the curves representing the WAAM surface contours were augmented into the 3-layer adaptive TFM algorithm to produce the TFM frames before their normalization. All the TFM frames used to construct the C-scan were normalized to visualize the entire image on the same dB scale. The C-scan was formed by populating a new 2-dimensional array's columns with maximum detected amplitudes from all TFM frame's columns from n number (n = 200) of TFM frames, as explained in background chapter 2.

The size of the C-scan presented in this thesis was set to 150×200 pixels (Number of pixels in the horizontal axis of the TFM frame × the number of frames). The resulting C-scan image was normalized to the peak amplitude and plotted on a dB scale to an averaged noise level (0 to -12 dB), giving the best visual contrast between a signal from tungsten tubes and interference from the background noise levels.

4.5. Ultrasound Data Review and Discussion

In this section, the results of an in-process NDE are presented and discussed. Hence, the outcome of the in-process inspection is depicted in Figure 4.9 (a), where the signal from Tube 1 and Tube 2, with an internal diameter of 1.0 mm were successfully detected. At first glance, stronger signal levels are observed from a longitudinally placed, 30 mm long, Tube 1. It is worth mentioning, that a matching signal length of approximately 30 mm along the inspection travel direction was also well noticeable. Tube 2, embedded in the transverse direction, showed a visually weaker signal strength, where the energy from the tube was represented by a concentrated signal in the centre of the corresponding frames approximately 100 mm from the inspection start point. This loss of signal quality was associated with the local loss of compliance caused by the surface waviness in both longitudinal and traverse directions (measured amplitude at least ± 1 mm). Therefore, a limited signal propagated towards the corners of the sample. To the extent, this loss of SNR was also observed on the longitudinal tungsten tube where the amplitude fluctuated due to surface waviness causing local loss of tyre’s compliance to the WAAM interface. Further losses of SNR could be associated with a lack of compensation for the thermal gradient that affects ultrasound wave velocity during propagation as also pointed out in [17].

Following a visual analysis of the results, a maximum amplitude along the X-axis was presented in Figure 4.9 (b). Based on this plot, an SNR of up to 12 dB was achieved from a scanning of the Tube 1 region while an SNR of 10 dB was seen from the Tube 2 region. Considering a dry-coupling condition these SNR values were found sufficient. Further analysis shows signal strength variations from the Tube 1 signal along with the scan, where an SNR drop of only 4 dB was observed. As mentioned above, these losses of signal amplitude can be associated with possible changes to the contact quality between the rubber tyre and non-flat WAAM.

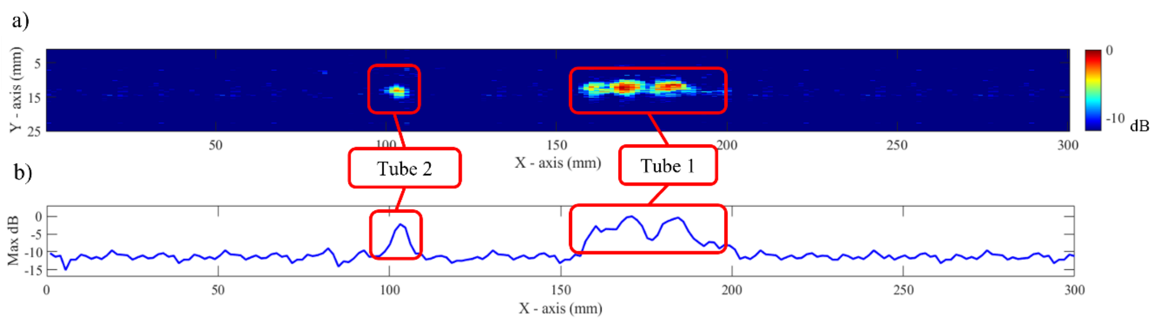

Figure 4.9 Results showing: (a) C-scan generated from frames computed using SAFT-TFM package and (B) plot presenting extracted maximum amplitude along X-axis

4.6. Summary of the Chapter

In this thesis chapter, the design and demonstration of a novel multi-robot cell for WAAM and ultrasound in-process NDE was presented. The architecture, based on two industrial robotic manipulators featuring a deployed plasma arc WAAM process and high-temperature PAUT roller-probe was introduced along with a software control package, merging manufacture and NDE into a single continuous process.

The in-process inspection capability was demonstrated by conducting a dry-coupled ultrasound in-process inspection of the Ti-6Al-4V WAAM wall with embedded tungsten tubes, with an internal diameter of 1.0 mm and planted in parallel and traverse direction to the building direction. Employing FMC data acquisition, an interior image of the experimental wall was computed by deploying a SAFT-TFM package, presented and evaluated in Chapter 3. The results of the in-process inspection showed successfully detected embedded reflectors on a C-Scan image, demonstrating the ability to detect defects just after their creation paving the way for possible in-process repair processes to be deployed in the future.

To summarize, the research presented in this chapter further amplifies the potential WAAM benefits, through the deployment of flexible and automated in-process NDE approaches, as compared to post-manufacturing inspection.

Chapter 5

Investigation of Virtual Source Aperture for Dry-coupled Inspection of As-built WAAM Component

5.1. Introduction

Chapter 3 has introduced an ultrasound imaging concept to overcome coupling challenges with a dry-coupled roller-probe inspection of as-built WAAM components. The introduced SAFT-TFM package enabled the reconstruction of an unknown non-flat interface of WAAM and subsequent ray-tracing towards the interior of the targeted interior volume to inspect for possible flaws through two refractive boundaries. This was accommodated by pre-collection of FMC data, where a single element was excited while the whole aperture was set to receive. However, throughout the experimental work and the in-process inspection work presented in Chapter 4, the following limitations were observed:

- The FMC data was characteristically built up of A-scans for every possible combination of transmitting and receiving elements and stored in a sizable 3-D matrix. For instance, a single FMC dataset collected using a 64-element array inside the roller-probe consists of 4096 A-scans.

- The FMC frame acquisition frequency was negatively influenced as well, which limited the overall inspection speed during the online inspection. Hence, low inspection rates could result from in-process NDE becoming difficult to integrate into the overall built process.
- Moreover, a common element pitch in PAUT is designed to be only a fraction of a millimeter, thus the retrieved signal strength and the energy are often low in single element pulse excitation. This is another limiting factor when considering inspection scenarios through roller-probe's refractive and attenuative layers between the internal components and the arbitrary WAAM surface.

The desire to address these limitations discovered throughout previous research chapters of this thesis has driven the investigation of advanced ultrasound data acquisition methods suitable for dry-coupled roller-probe inspection of WAAM.

In the body of this chapter, the benefits of one such technique called the Virtual Source Aperture (VSA) are assessed in combination with the SAFT-TFM package. The overall aim is to I) strengthen the retrieved signal amplitude by increasing the transmitted ultrasound wave energy that enters the internal volume of WAAM, II) reduce the size of the data frame, and III) increase the data collection frequency, all while maintaining an indistinguishable SNR as compared to conventional FMC-based TFM imaging.

The VSA was first introduced in medical ultrasound applications [68]. Since, the technique has also been developed and utilized in NDE research, where for instance it was optimized, and its effects investigated for inspection of geometrically complicated components in immersion [99-101]. A markedly lower total number of transmitting apertures was employed to match the SNR of FMC-based imaging methods when imaging using a 32-element VSA sub-aperture.

Furthermore, the potential for accurate surface reconstruction, with an average error to the true surface lower than 0.1 mm, was published in [99, 100]. It is important to note, that the ability to accurately reconstruct a surface of a geometrically complex component such as WAAM is a must to accomplish precise ray-tracing [99, 100, 102].

The key advantage of the VSA technique can be realized by the ability to configure large element sub-apertures which can increase the sonification energy within the test piece. This can play a significant role when considering the ultrasound wave propagation through the roller probe, with attenuative internal components delay line (0.2 dB/mm) and tyre (1.7 dB/mm) [80].

Using the VSA data collection approach, the ultrasound beam profile is created from a virtual point above the physical array. Typically, the point is placed above the centre of the sub-aperture with a height equal to the distance between the first element and the centre of the sub-aperture [68]. The sub-aperture is then excited by applying delays to its elements individually which results in a newly formed large beam profile. The signal returning to the array is received by every element within the array forming a matrix of A-scans similar to that of convectional FMC. Subsequently, the data post-processing is accomplished using the DAS algorithm in the same way as the FMC data processing for TFM imaging with the difference that the transmit locations corresponding to the virtual source point of transmitting sub-apertures are used for the ray-tracing computations.

In this chapter, the SAFT-TFM imaging approach is adapted for processing of the alternative VSA acquisition technique and its applicability is investigated via simulation of roller-probe inspection of WAAM components with subsequent experimental dry-coupled inspection verification on a custom-designed reference WAAM block with artificial reflectors.

Further, the experimental work is performed via an as-built surface of the WAAM where the ability to reconstruct a WAAM interface, using SAFT, is analyzed by the comparison to a reference optical scan of the specimen and the reconstruction using a classical FMC acquisition. This is followed by a comparative analysis of the VSA-TFM and the FMC-TFM techniques on WAAM interior imaging capabilities and performances.

Finally, the advantages of the technique are summarized and demonstrated on a mock roller-probe WAAM inspection application.

5.2. Virtual Source Aperture (VSA) Technique and TFM Imaging

5.2.1. VSA Data Acquisition

Considering the VSA technique, the phased array transducer elements are excited in groups with transmission delay laws forming a Virtual Source (VS) above the actual physical aperture. In this work, the virtual point was centered to the arc-shaped wavefront generated, as seen in Figure 5.1.

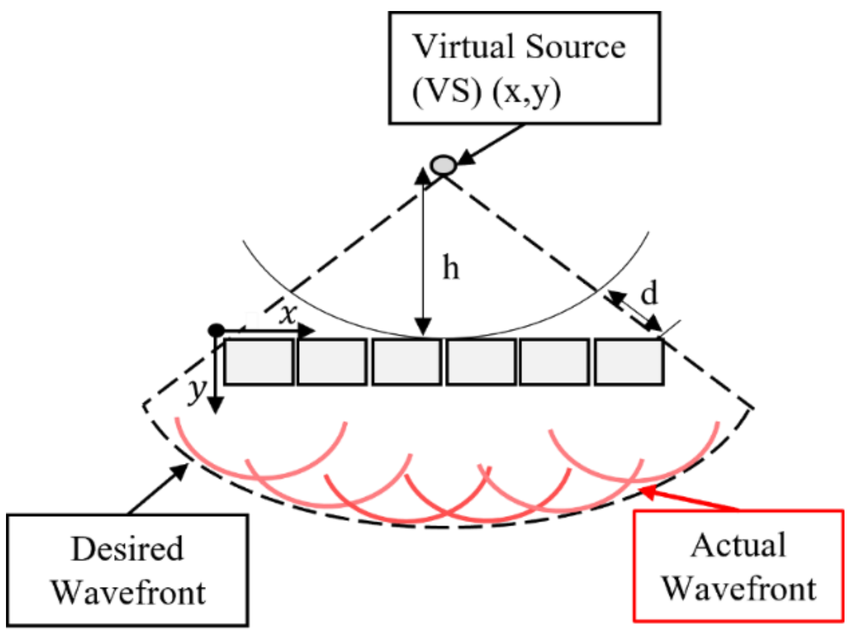

Figure 5.1 Diagram illustrating an example of how the virtual source transmission is created by applying delays to the elements of a sub-aperture of 6.

Since the VS was a simulated point of the centre of the arc from which the desired beam profile was created, the actual transmission was conducted by calculating the delays for the individual elements in the firing sub-aperture. These delays can be calculated by subtracting the vertical path (h) from the path connecting the virtual source point to each element within the sub-aperture. Hence, these delays are calculated by:

$$d_{vsp} = \frac{d}{v_1} = \frac{\sqrt{(x_{rx} - x_v)^2 + {y_v}^2} - h}{v_1} \tag{5.1}$$

Where the d_{vsp} was the delay value calculated for each firing element of the sub-aperture, h was the arc radius from which the delays were calculated, v_1 was the velocity of the first medium where the wave propagates in, and x_{rx} x_v and y_v were the x coordinates of the firing element and virtual source, and the y coordinate of the virtual source, respectively. Once the delays were calculated for the first sub-aperture, they were also be used for the subsequent sub-apertures. This was because the same beam profile was retained as the sub-aperture was shifted across the full aperture of the array by 1 element increments.

5.2.2. VSA – Total Focusing Method

Following the data acquisition, the imaging was accomplished using a TFM algorithm optimized for focusing through three media to FMC-based TFM presented in Chapter 3. To this end, the ToF from the virtual source (x_v, y_v) towards the pixel (x_p , y_p) with consideration of the refraction at two interfaces (x_{i1}, y_{i1}) and (x_{i2}, y_{i2}), as also illustrated in Figure 5.2, were calculated through:

$$T_{(Tv)} = \frac{\sqrt{(x_i - x_v)^2 + (y_i - y_v)^2}}{v_1} + \frac{\sqrt{(x_{i2} - x_i)^2 + (y_{i2} - y_i)^2}}{v_2} + \frac{\sqrt{\left(x_p - x_{i2}\right)^2 + \left(y_p - y_{i2}\right)^2}}{v_3} \tag{5.2}$$

And the ToF for the return journey from the pixel to a single receiving element was given by:

$$T_{(R)} = \frac{\sqrt{(x_{i1} - x_r)^2 + (y_{i1} - y_r)^2}}{v_1} + \frac{\sqrt{(x_{i2} - x_{i1})^2 + (y_{i2} - y_{i1})^2}}{v_2} + \frac{\sqrt{\left(x_p - x_{i2}\right)^2 + \left(y_p - y_{i2}\right)^2}}{v_3} \tag{5.3}$$

Given the transmit and receive ToFs calculated through Equations (5.2) and (5.3), the signal intensity at a pixel *A(P)* resulting from all transmit-receive combinations can be expressed as:

$$A(P) = \sum_{i=1}^{N_V} \sum_{j=1}^{N_e} R_{i,j} \left(T_{T_V(i)} + T_{R(j)} - \frac{h}{v_1}\right) \tag{5.4}$$

Where *A(P)* was the pixel amplitude summed from signals $R_{i,j}$, for every transmit-receive combination. The signals were selected according to a timestamp calculated as a sum of the two journeys between I) VS sub-aperture to pixel ($T_{Tv(i)}$) and II) pixel to receive element ($T_{R(j)}$). Since the wave was generated by the physical transducer sub-aperture and not the hypothetical VS position above the aperture, it was important to subtract the ToF for the height (*h*) from the calculated ToF within the first medium.

The refraction occurring at the interfaces, as illustrated in Figure 5.2, were solved using the same algorithm as presented in Chapter 3. The image-producing logic from the FMC-based TFM was also carried over, with the image being produced utilizing the envelope feature and normalizing on a dB scale.

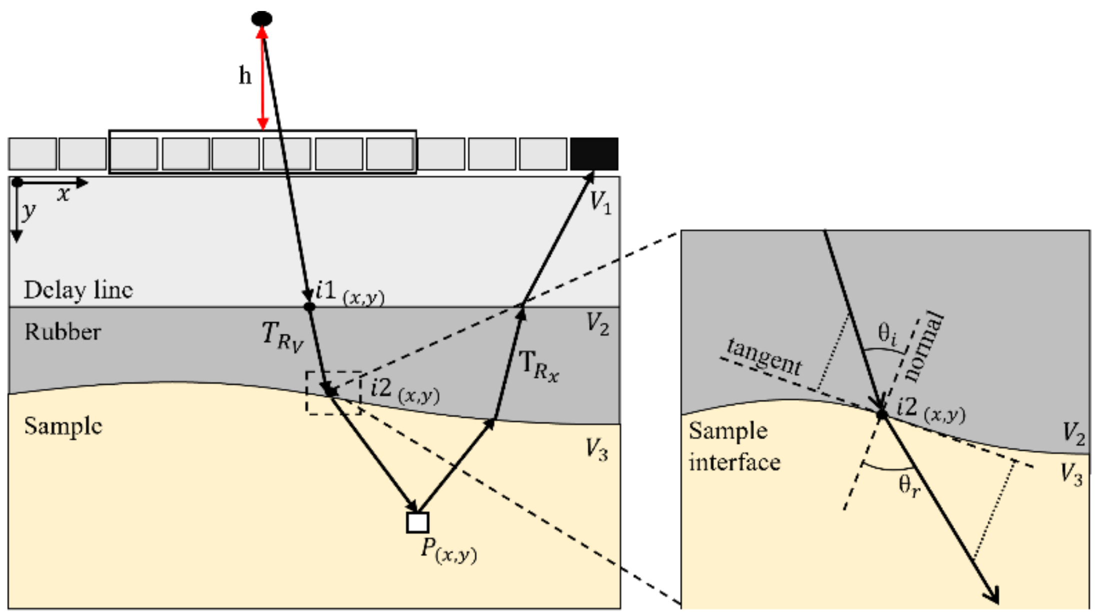

Figure 5.2 Diagram illustrating a raytracing for ToF calculations between a virtual source transmitting sub-aperture, a target pixel, and a receiving element. The ray-tracing is carried out through three media noting the refractions on planar (delay-line/tyre) and non-planar (tyre/WAAM) interfaces

5.2.3. Ultrasound Surface Profile Reconstruction (VSA-SAFT)

As introduced in chapter 3, the surface of the tyre/WAAM interface must be reconstructed to accurately calculate the ToF between the array and the interior of WAAM. While the actual surface extraction from the SAFT image was based on the same logic as to FMC-based SAFT, the different input data (VSA) must be accounted for. To do so, a dual-medium (*i.e.*, delay line and Tyre) algorithm, which was originally developed for FMC-SAFT imaging, was adapted to process the VSA data and image the interior of the tyre interface. A dual-medium DAS SAFT algorithm with angular aperture limit can be expressed by:

$$A_{rubber}(P) = \sum_{i=1}^{N_V} \sum_{j_{min}}^{j_{max}} R_{i,j} \left(T_{R_V(i)} + T_{R(j)} - \frac{h}{v_1}\right) \tag{5.5}$$

where the receive sub-aperture was limited by predefined ranging from an angle $j_{min} = -\alpha$ to angle $j_{max} = \alpha$. This restriction of the contributing receive elements is illustrated in Figure 5.3. The ToFs ($T_{T/R}$) were calculated in the coordinate system (x, y) and were given by:

$$T_{(Tv)} = \frac{\sqrt{(x_1 - x_v)^2 + (y_{i1} - y_v)^2}}{v_1} + \frac{\sqrt{\left(x_p - x_p\right)^2 + \left(y_p - y_{i1}\right)^2}}{v_2} \tag{5.6}$$

$$T_{(R)} = \frac{\sqrt{(x_1 - x_t)^2 + (y_{i1} - y_t)^2}}{v_1} + \frac{\sqrt{\left(x_p - x_{i1}\right)^2 + \left(y_p - y_{i1}\right)^2}}{v_2} \tag{5.7}$$

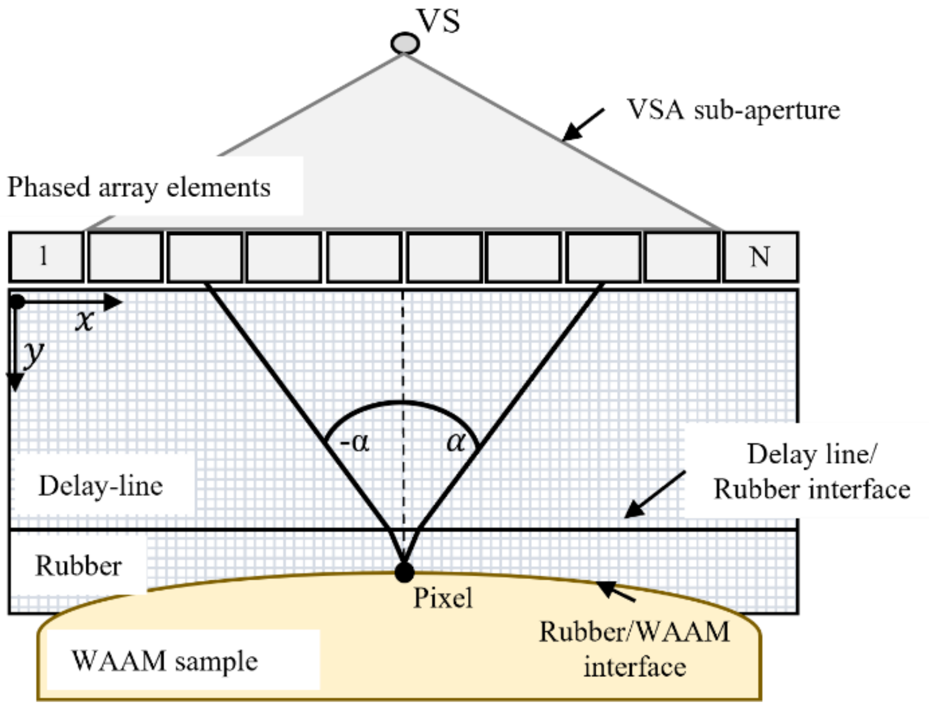

Figure 5.3 Diagram illustrating the phased array elements contributing to the pixel of the SAFT image targeting the tyre/WAAM interface and limited by the angle range of -α to α

The same approach as introduced in Chapter 3 was used to reconstruct the surface curvature of the WAAM, where the global thresholding was applied to detect the points representing the surface through which the 4th order polynomial curve was fitted. This curve was then imported into the final TFM frame computation.

5.3. Experimental Method

5.3.1. Reference Test Specimen

To initially evaluate the VSA technique, a purpose-designed WAAM calibration sample (Block A), shown in Figure 5.4, was designated for the simulation-based and experimental work.

Ti-6Al-4V Block A was deposited using a plasma arc process with a parallel deposition strategy [6] where 3 straight beads were laid next to each other in the same direction. The deposition process parameters are summarized in Table 5.1. The WAAM was protected from oxidation using a local shielding device continuously supplying argon gas onto the hot titanium at a rate of 110 l/minute. Even and odd layers of the components were deposited in opposite directions to avoid the material from being overbuilt at the start edge.

Once the deposition of Block A was completed, a step-shaped section, also depicted in Figure 5.4, was machined out of the WAAM. The ultrasound testing was performed to assure no substantial defects were present in Block A.

Following, a set of reference reflectors in the shape of flat bottom holes, intended for other studies, and a wide range of Side Drilled Holes (SDH) of 1.0 mm in diameter at different depths were produced using an electro-discharge-machining process.

The SDH defects, marked by the red rectangle (Figure 5.4), were selected to assess the performance of the VSA throughout the simulation and experimental work. These four selected SDHs to differ in depth, extending from 6.0 to 15.0 mm, with a 6.0 mm gap between them.

Table 5.1 Deposition parameters of the reference test specimen

Region	***Current [Amps]***	***Travel speed (mm/s)***	***Wire feed speed (mm/s)***
Outer 2 beads	180	3.6	38.3
Core bead	180	3.6	33.3

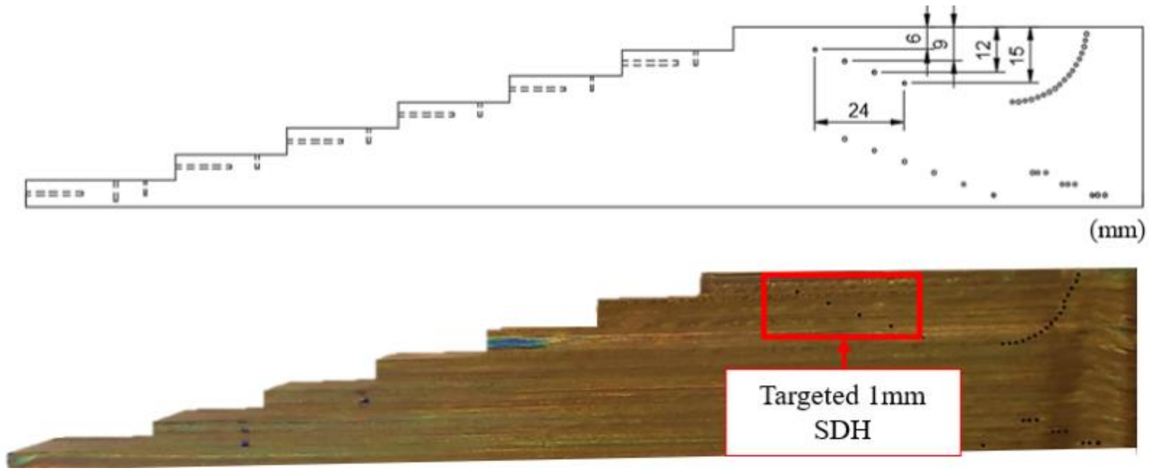

Figure 5.4 Calibration titanium WAAM block (Block A)

5.3.2. Simulation of the VSA versus FMC-Based Imaging

At first, a simulation was conducted to compare the quality of imaging produced from the VSA data and the FMC-based inspection. The simulation was performed in CIVA software (by EXRENDE, France, Version: 2017 SP2) application which has proven reliable for modeling and validating ultrasonic inspection results in different application scenarios [103, 104]. The inspection parameters such as delay line, rubber thickness and PAUT were identical to the experimental roller-probe assembled for this research in terms of geometry and properties. The roller-probe was modeled as a phased array transducer placed on a 26 mm thick delay line and a 6 mm thick rubber interface as seen in Figure 5.5. The defects were chosen for the simulation corresponded to the SDH defects presented in Block A in section 5.3.1. and marked in Figure 5.5. To diminish discrepancies between the real and simulated material properties, the velocity and the attenuation properties of different components were considered in the model. These values were obtained through a pulse-echo measurement of individual components of the roller-probe, including the delay line and the rubber, and the titanium WAAM test specimen at the frequency of 5 MHz in a direction matching the inspection scenario. Table 5.2 summarizes the measured values used in the simulation. The ultrasonic wave interactions with all interfaces and reflectors were enabled in the model for the most accurate simulation of the real-world inspection scenario.

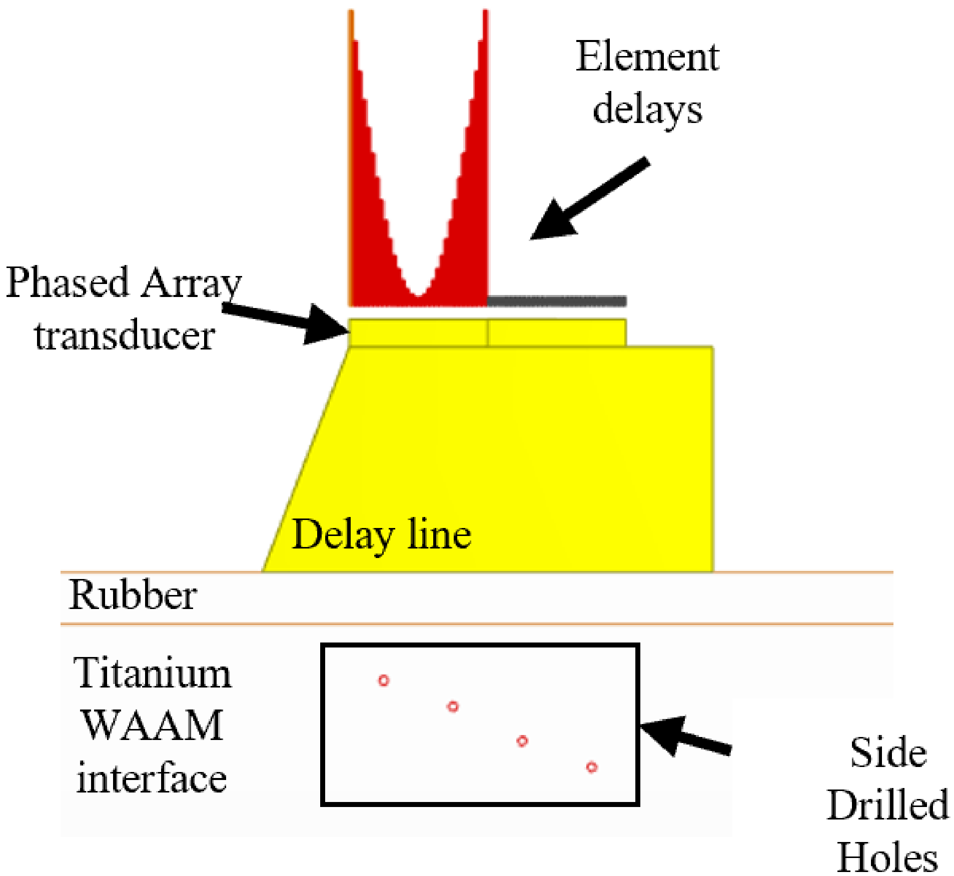

Figure 5.5 Simulation setup in the CIVA interface

Table 5.2 Attenuation data

Material	***Attenuation (dB/mm)***	***Acoustic velocity (m/s)***
Delay line	0.50	2480
Rubber	1.90	1006
Calibration WAAM	0.09	6300

A MATLAB script was developed to calculate delays for individual elements within the VSA sub-aperture, according to Equation 5.1 explained in section 5.2.1., and then the delays were imported into the CIVA as the VSA beamforming was not integrated by default within CIVA software. The acoustic velocities were assigned to domains according to the measured values presented in Table 5.2. Elements were excited at a pulse frequency of 5 MHz using a Hanning signal and 50% bandwidth at -6 dB. A data sampling frequency of 50 MHz was chosen for the acquisition. Once the simulation was concluded, the raw data matrix was exported and processed in MATLAB using the algorithms developed and explained in Sections 5.2.2 and 5.2.3.

5.3.3. Experimental Inspection Hardware Setup

The ultrasonic roller-probe, used during the experiments, was based on a 5 MHz 64-element linear array with specifications presented in Table 3.1. The array was enclosed in a rotary tyre (6 mm thick) and acoustically coupled to a solid delay line (26 mm thick), similarly to in previous chapters (3 and 4). The acoustic velocities for the delay line and rubber are seen in Table 5.2. To achieve a smooth frictionless rolling of the roller-probe, a liquid coupling gel was used to fill the roller-probe.

The ultrasound roller-probe was mounted on a KUKA KR-90 robot allowing for precise delivery and positioning of the sensor on the WAAM component for data collection as seen on Figure 5.6. A Force/Torque sensor (FTN-GAMMA-IP65 SI-130-10, Schunk) was employed to connect the roller-probe to the robot. Provided that, a steady force of 130 N was applied to the WAAM specimen during the inspection. The data were acquired using an LTPA array controller (PEAK NDT, Derby UK) mounted on the robotic arm itself.

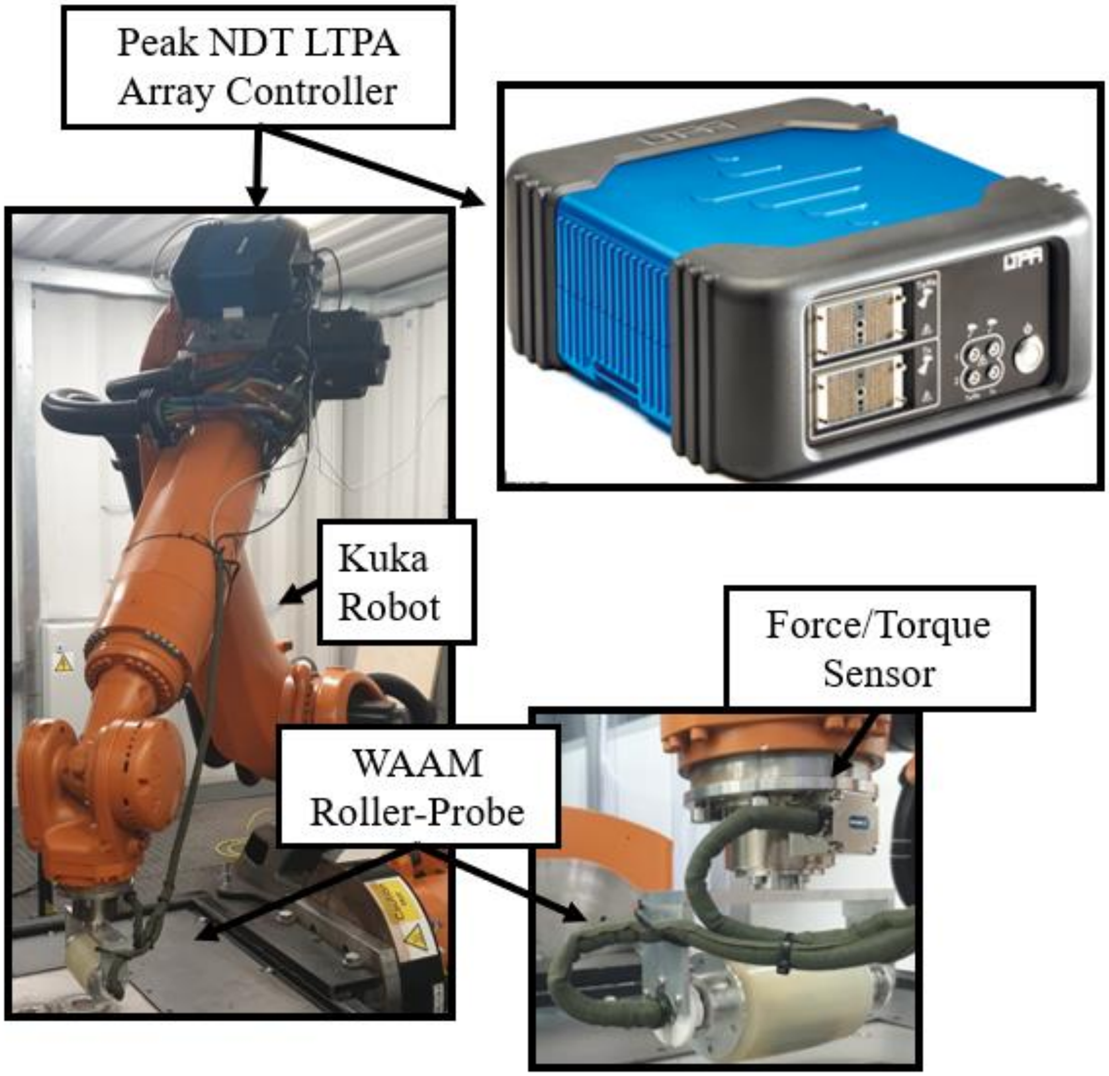

Figure 5.6 Experimental setup showing a KUKA KR 90 robot, ultrasound array controller and the ultrasound WAAM roller-probe

5.3.4. Experimental Data Acquisition and Processing

The 16-bit FMC and VSA data were collected using a sampling frequency of 50 MHz. The excitation voltage was set to 200 V and the duration of the excitation pulse was 100 ns. All data was recorded with a receiver hardware gain of 50 dB.

The VSA sub-aperture employed during the experiments was kept constant at 32 elements with an increment of 1 element giving a total of 33 excitations per set of VSA data. The size of the sub-aperture used throughout this chapter was found to be the best performing configuration and was also indicated by literature [99, 100] as the most suitable for imaging through the interfaces and complex geometries. With the 33 sub-apertures transmitting and all elements receiving, a total of 64×33 A-scans were stored, each containing 3000 samples. The length of the A-scan was found adequately long, reaching below the targeted imaging window. The FMC data used for comparison was acquired using a full aperture of 64 elements, thus, forming a matrix of 64×64 A-scans, each 3000 samples long.

The SAFT surface finding was performed on an image with 10 pixels per image mm, therefore, a pixel grid size of 320×30 pixels. The TFM images were produced using 6 pixels/mm, according to the logic described in Chapter 3, where the adaptive TFM images were formed as a mesh with the size of 132×156 pixels and images formed for the calibration (machined) sample were set to a grid of 192×72 pixels.

5.4. Results and Discussion

5.4.1. Evaluation of VSA on a Calibration Titanium WAAM Sample Through a Machined Surface Using a Modeling Approach and Experiment

First, the application of the VSA was investigated via SDH defects inspection modeling through the machined surface of the Block A. Figures 5.7 (a, b) depicts the resulting images of the inspection simulation based on the FMC and VSA datasets, respectively. Each image was plotted on a -20 dB scale to the image's maximum value.

Clear indications for the four 1.0 mm SDH reflectors were observed in both simulation-based images of Figures 5.9 (a, b). The VSA-TFM image was plotted after normalizing it to the maximum of the FMC-TFM image. The results presented a stronger maximum signal amplitude of up to 2.3 dB for the VSA image where 33 excitations of the 32-element sub-aperture were employed.

The same normalizing procedure was conducted for images from the experimental inspection depicted in Figures 5.7 (c, d). Similar to the simulation case, the experimental VSA-TFM image showed an increase of up to 1.8 dB in the maximum amplitude as compared to the FMC-TFM. However, this increase was accompanied by a higher noise level in the near-surface region. The near-surface noise was not present in the simulation results as the noise could only be introduced at the imaging stage as speckle noise in CIVA and not in the form of scattering A-scan noise on the FMC and VSA raw data. Provided that the imaging process was conducted in MATLAB 2020a and did not have the possibility of introducing the noise to FMC and VSA raw data, the simulation images were produced noise-free.

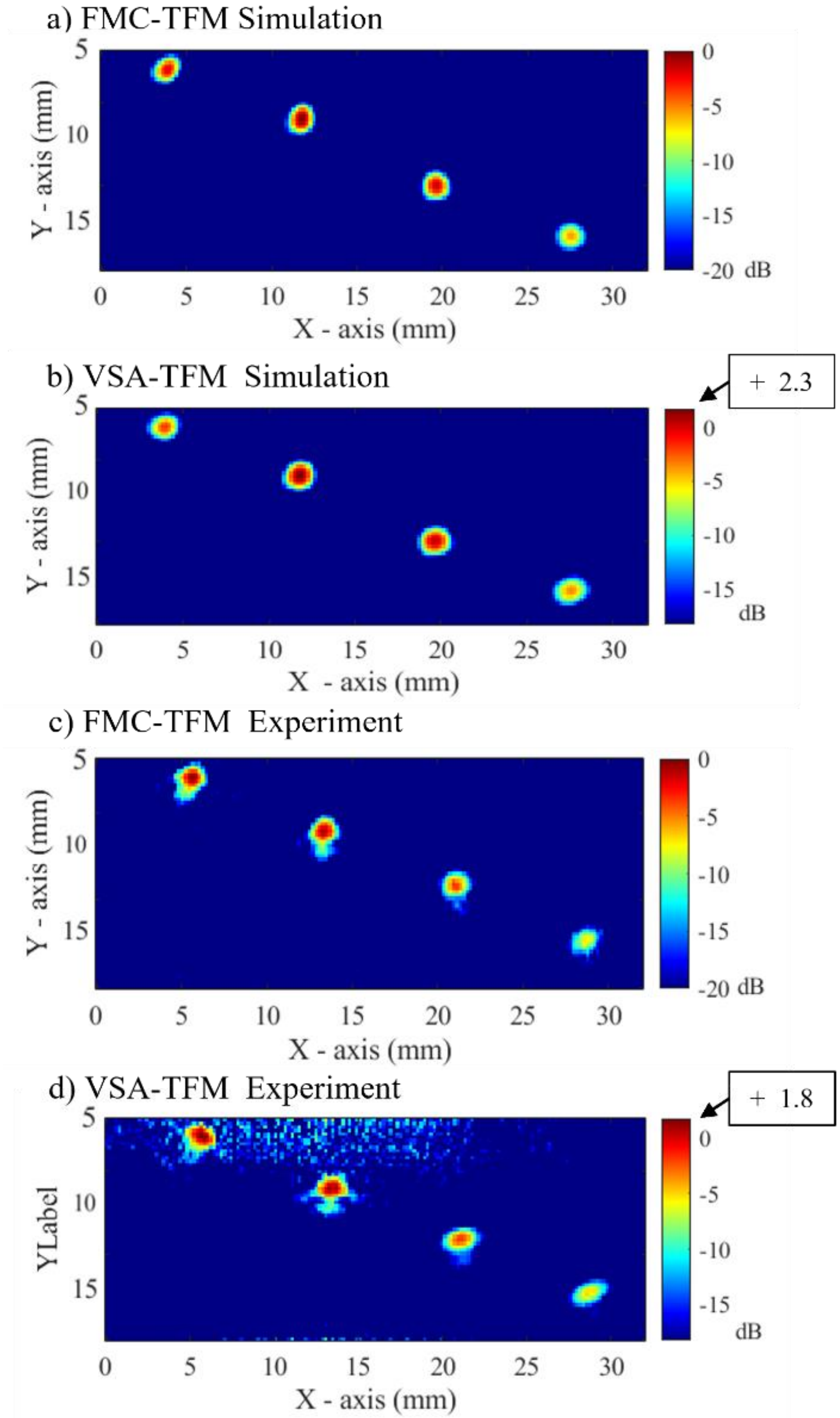

Figure 5.7 TFM imaging results based on the simulated a) FMC and b) VSA data sets as well as experimental c) FMC, and d) VSA data

Furthermore, comparing the SDH defect amplitudes obtained from VSA and FMC data, Figures 5.8 (a, b) display 2 plots where the maximum image intensities in dB along the vertical axis in the simulation and experiment are extracted, respectively. Generally, a good agreement between the maximum amplitudes of the two plots corresponding to simulations and experiments was observed. The variations between retrieved peak amplitudes, from all SDH, by FMC-TFM and VSA-TFM, were summarized in Table 5.4. The values in the Table confirmed the energy strength retrieved from the reflectors was higher by up to 2.5 dB in the simulation and 2.7 dB in the experiment when using the VSA aperture. The lowest amplitude increase was achieved for the near-surface SDH of only 0.8 dB for simulation and 1.8 dB in the experiment while the same increase was observed for the 12.0 mm deep defect. In general, the maximum amplitude levels and the amplitude differences observed between the VSA and FMC plots in the simulation were consistent for all four defects and correlate well to the VSA and FMC experimental amplitude discrepancies.

Moreover, a similar SNR of approximately 20 dB was achieved by both FMC and VSA-based imaging approaches, which complimented the goals of this work. As can be seen from Figure 5.8, the noise baseline for the simulations was lower which is the result of noise-free raw data used in the imaging.

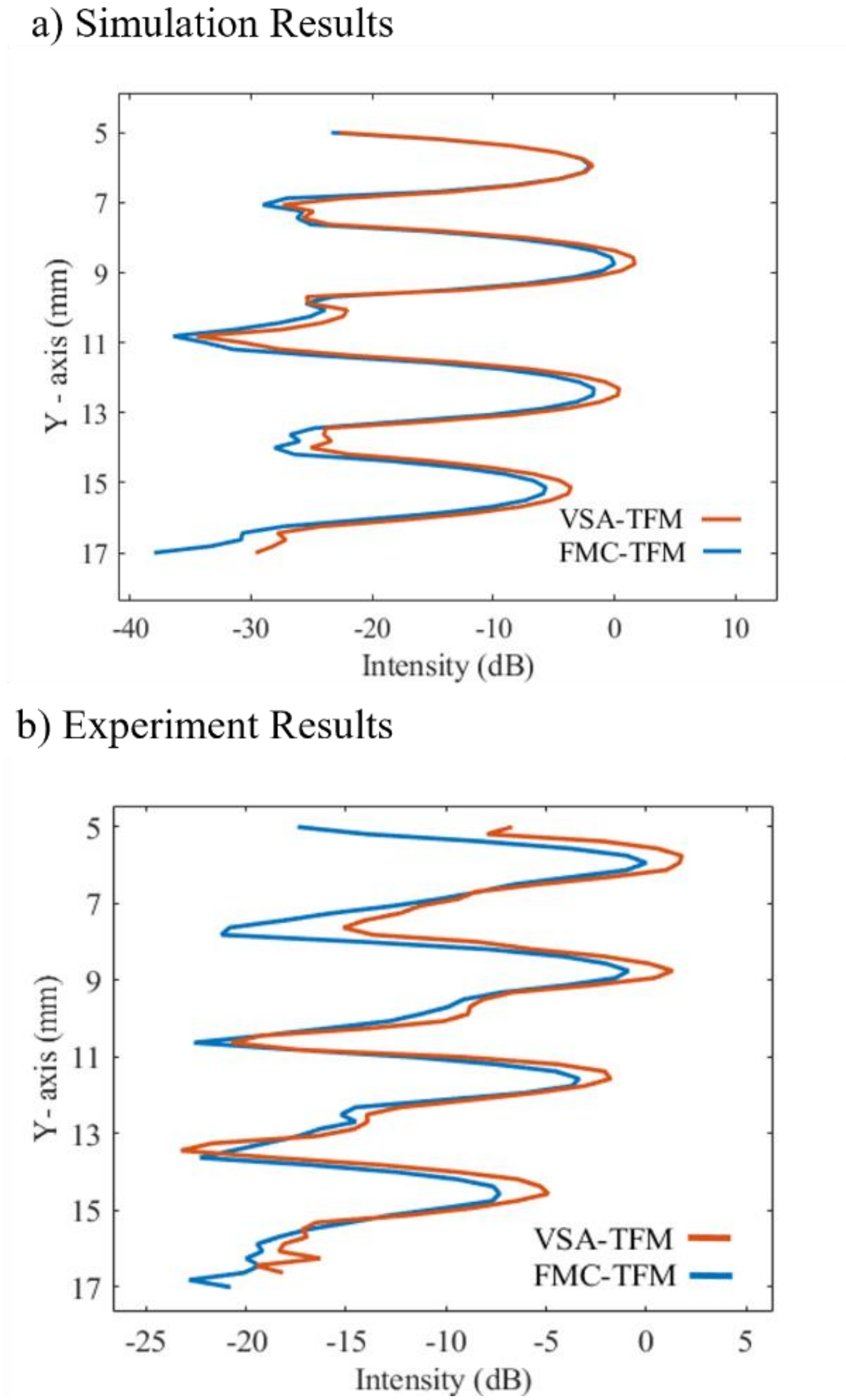

Figure 5.8 Plots showing maximum vertical intensities of the defects VSA-TFM and FMC-TFM images obtained through a) simulation and b) experiment

Table 5.3 Signal strength of individual SDH in the Block A

Defect Depth (mm)	***FMC Modelling (dB)***	***VSA Modelling (dB)***	***FMC Experiment (dB)***	***VSA Experiment (dB)***
6.0	- 0.7	0.1	0	+ 1.8
9.0	0	+ 2.3	- 0.9	+ 1.3
12.0	-3.5	+ 0.9	- 3.5	- 1.7
15.0	-9.1	-6.4	- 7.3	- 4.8

5.4.2. Evaluation of VSA on WAAM Inspection Through an As-built Surface

5.4.2.1. As-built WAAM Sample

After successful verification of the proposed VSA technique on inspection through the machined surface, the experiments were also carried out through an as-built surface of a manufactured Ti-6Al-4V WAAM wall (Block B).

Block B, depicted in Figure 5.9, was built using a plasma arc WAAM process, where each layer approximately 35 mm wide was deposited by a single oscillating bead [20]. Five layers were deposited to the height of approximately 15 mm for this component.

The evaluation of the VSA technique was conducted by inspection of Block B containing three SDH defects with 1.0 mm in diameter. The holes were drilled approximately 20 mm deep into the sample while each SDH was placed directly 5 mm below the peak of the surface contour.

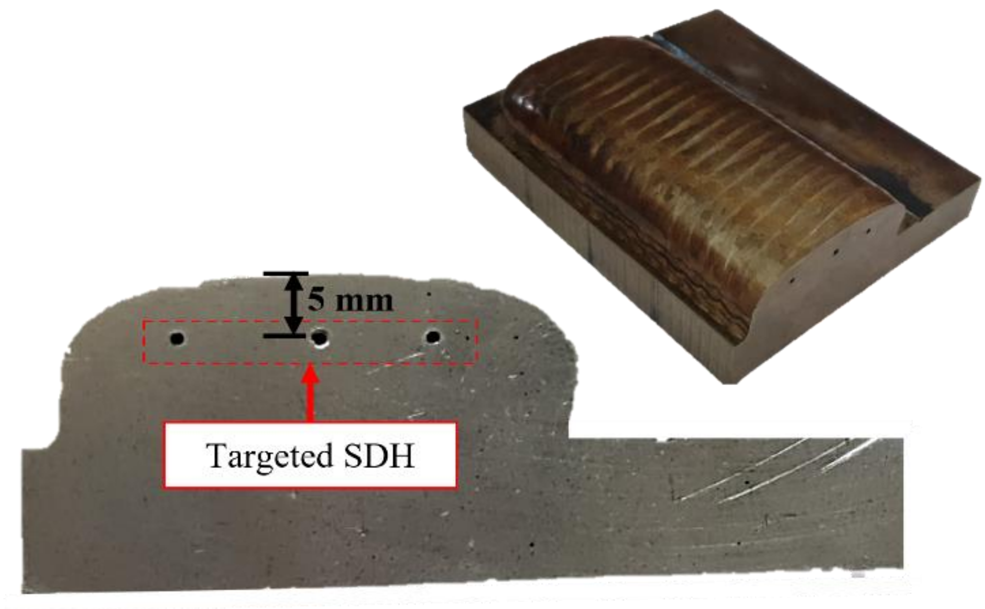

Figure 5.9 Titanium WAAM sample with 1 mm SDHs used for experimental work through the as-built surface

5.4.2.2. Investigation of virtual source aperture data for surface reconstruction

In this section, the application of VSA data for ultrasound surface reconstruction was evaluated. The results were compared with the FMC-SAFT surface reconstruction approach and a true surface of the WAAM obtained via a non-contact metrology laser scan, performed using a laser profiler with a vertical accuracy of 12 µm [86].

The SAFT angle limitation that was applied to FMC-SAFT, as described in the background section 3.2.3., was set to $\alpha = \pm 7.5°$ as in Chapter 3. These limits were changed for the receiving elements of the VSA-SAFT to ± 5°, where tighter limits were found to perform more accurately. The surface finding amplitude threshold was found to adequately filter noise when set to -10 dB from the maximum, for FMC-SAFT and -15 dB for VSA-SAFT. The surface images were plotted in a 0 to -30 dB scale where the features were best represented with the noise largely omitted in the image.

Pixels with the highest amplitude were identified in each column of the image as a point representing the surface profile as can be seen in Figure 5.10. A curve was fitted through the pixels with maximum amplitudes in each FMC-SAFT and VSA-SAFT image representing the non-planar WAAM upper surface. There are also two distinct indications from the tyre/air interface at the two corners of the tyre/WAAM interface where the contact with the WAAM surface ends. These indications are stronger in amplitude due to the larger impedance mismatch of rubber and air; hence easily identifiable. In light of this, the part of the curve contained between these two corner indications can be readily extracted and used for WAAM interior TFM imaging in the later sections. Comparing the two profiles reconstructed by FMC-SAFT and VSA-SAFT to a laser reference scan, a strong agreement between the 3 curves was observed in Figure 5.11 (a).

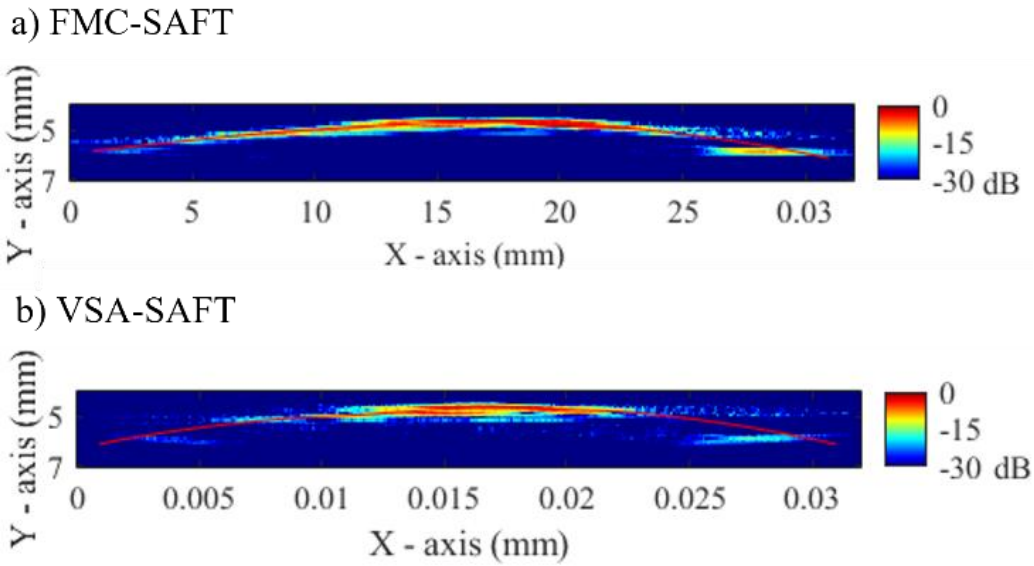

Figure 5.10 Surface reconstruction images: a) FMC-SAFT and b) VSA-SAFT

However, to accurately measure the deviation (error) $\Delta_{average}$ of the FMC-SAFT and VSA-SAFT reconstructed surface with reference to the true surface, the estimation error for each of the two techniques was obtained through:

$$\Delta_{average} = \frac{1}{p}\sum_{p=1}^{p=n} |S_{Opt}^{p} - S_{UT}^{p}| \tag{5.8}$$

Where the S_{Opt}^{p} and S_{UT}^{p} are the Y-axis surface points obtained by the laser and the ultrasound technique, respectively, and n (n = 300) is the total number of points p. The comparison was only made on the segment of the surface where both curves coexisted.

Figure 5.11 (b) shows an error distribution along the X-axis when comparing the curve to the true surface. By averaging the error between a VSA-SAFT to the true surface using

Equation 5.8, the $\Delta_{average}$ was calculated to be 0.0481 mm while the FMC-SAFT showed a slightly lower $\Delta_{average}$ of 0.0420 mm.

However, in both cases, the average error was less than a quarter of the wavelength (λ = 0.2 mm) in the second (rubber) medium and titanium ($\lambda \approx$ 1.2 mm) at the selected frequency. This was a crucial finding as an error value larger than a quarter of the wavelength could have a detrimental effect on the final TFM image summation causing the defect distortion and the loss of coherence [99].

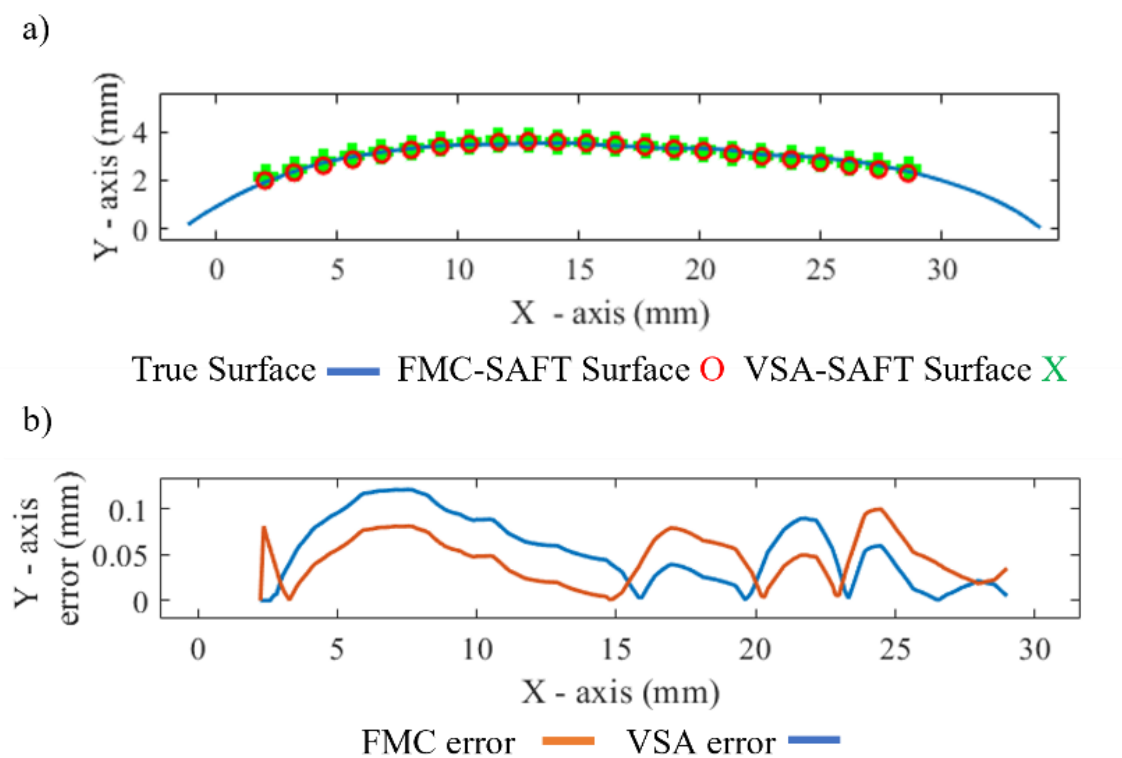

Figure 5.11 (a) Assessing the surface reconstruction accuracy of VSA-SAFT and FMC-SAFT as compared to the optical scan results and (b) surface reconstruction errors produced through the two methods

5.4.2.3. Evaluation of the VSA-TFM Imaging on the As-built WAAM Component with 1 mm SDH Defects.

After the successful surface profile detection, they were factored in the TFM algorithm to form the fully focused interior WAAM images through both VSA-TFM and FMC-TFM as illustrated in Figures 5.12 (a, b), respectively. The FMC-TFM and VSA-TFM were normalized to the maximum of the VSA-TFM signal corresponding to the centre SDH reflector. Both images were presented on a dB scale ranging between the maximum amplitude of the centre reflector and -20 dB of this amplitude. This enabled focusing the analysis on the signal retrieved from the SDH reflectors rather than a subsurface noise level present in the images. Since the maximum signal intensity from the subsurface noise was found stronger than the amplitude of the centre SDH, in both images, a large portion of the surface signal was seen saturated due to its presence above the dB scale threshold.

The reference FMC-TFM, showed clear indications from the three SDHs, with a peak amplitude at - 4.7 dB, however, the SDH on the right-hand side of the image had a weaker signal amplitude, at - 9.1 dB, as compared to the rest of them. The VSA-TFM image was presented in Figure 5.12 (a). All three defects were detectable in the image with comparably equal strength, ranging between – 4.8 dB and -7.5 dB, from all three reflectors. However, the subsurface noise was stronger as well, which was the result of increased UT beam energy in the VSA and thus the stronger reflections at the tyre/WAAM interface.

Following the visual analysis of the images, Figure 13 was plotted to show the signal intensity map of the SDH defects along the X-axis created from a region 4 mm beneath the surface reflections to the depth of a baseplate interface (15 mm below the surface). To analyze and compare the signal strength retrieved from this region, the FMC-TFM plot was renormalized to a maximum of the defect region in VSA-TFM. This facilitated the comparison of the signal strength retrieved from all the SDH defects to the detected peak.

A balanced SNR of approximately 18 dB was achieved for the defects located at the center and left in the FMC-TFM image while the defect on the right-hand side showed an SNR of around 15 dB. A similar level of SNR at approximately 20 dB for the centre defect and 18dB for the left-hand side defect was observed in the VSA-TFM image, however, in contrast to the previous case, the defect on the right also displayed the SNR level of 18 dB. Table 5.5 shows the signal levels of SDHs in both VSA and FMC TFM images where higher peak signals were achieved in the VSA-TFM by 2.55 dB, 4.69 dB and 6.42 dB for left, center and right SDHs, respectively. It is worth noting, that the naturally occurring material noise levels have increased as well without negatively affecting the SNR.

Additionally, the images in Figure 5.12 displayed a back wall echo of Block B and a near-wall reflection that creates a characteristic dead zone limiting the detectability of defects near the surface. A stronger surface signal zone was visible in the VSA-TFM image reaching approximately 3.5 mm, while for the FMC-TFM image this area produces less interference for the defect signals as it shrinks to around 2 mm in depth and mostly concentrates in the corners.

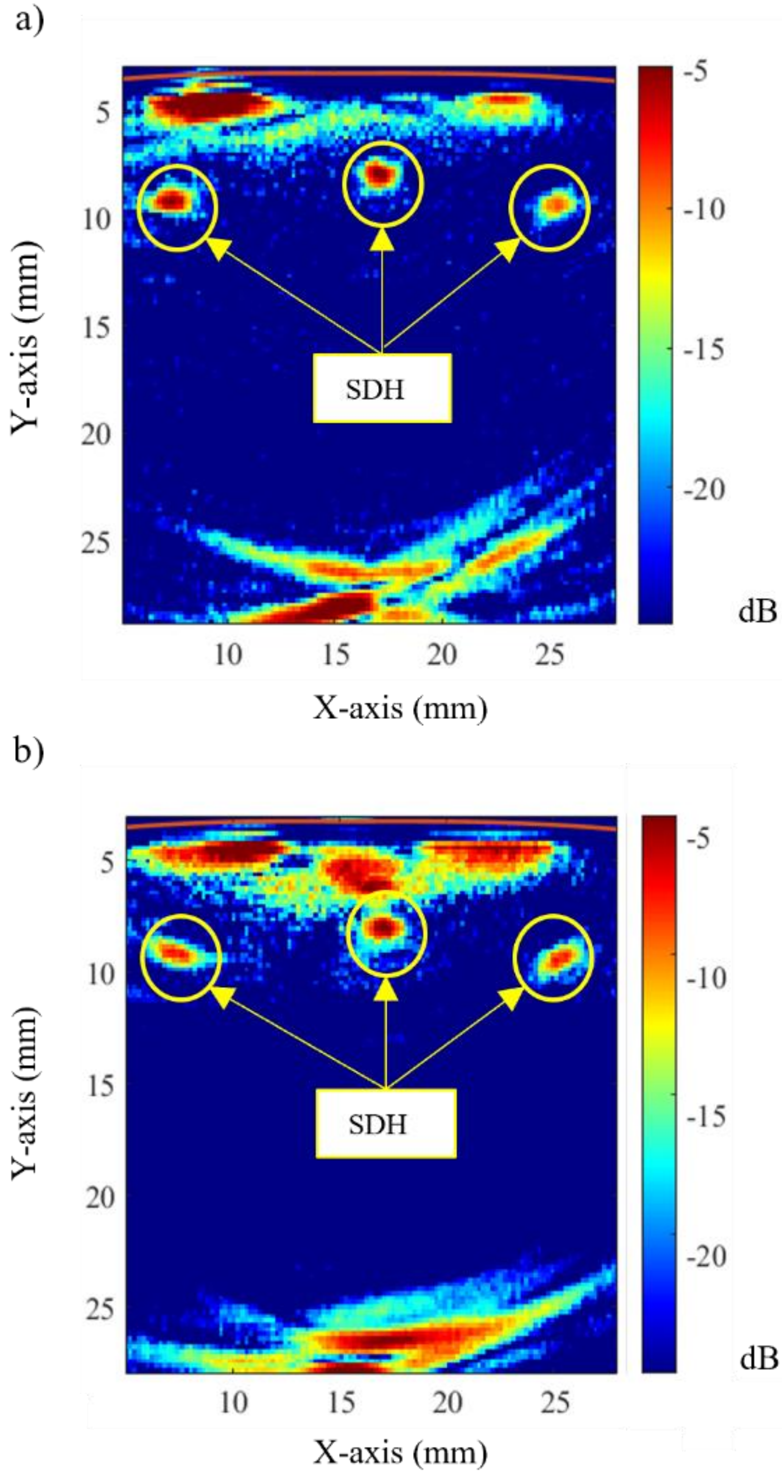

Figure 5.12 a) VSA-TFM and b) FMC-TFM images capturing the interior of the Block B with 3 SDHs

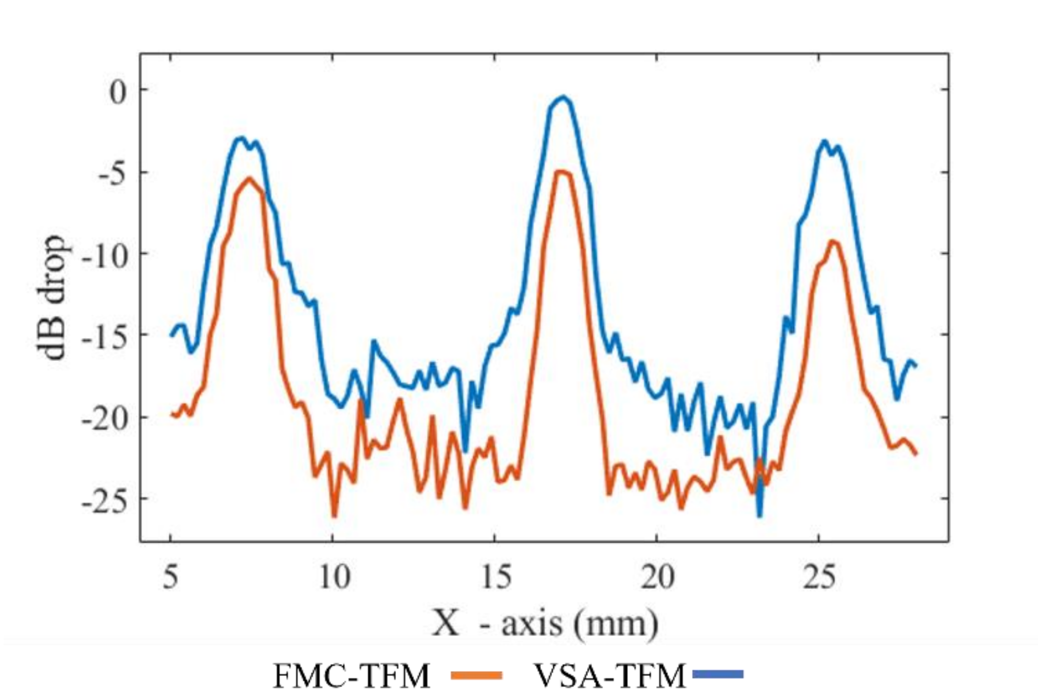

Figure 5.13 plot showing the maximum horizontal intensity of the SDH defects indications in VSA-TFM (blue) and FMC-TFM (orange) images

Table 5.4 Signal strength of the SDHs in Block B

Defect position	***FMC Experiment (dB)***	***VSA Experiment (dB)***
left	-5.06	-2.51
centre	-4.69	0.00
right	- 9.12	-2.70

5.4.3. Benefits of the VSA-TFM imaging for the Inspection Automation

When considering the use of ultrasound arrays for automated inspections, the operator should be aware of the data frame rates as these can dictate the speed of inspection. The maximum theoretical frame rate is constrained by the acquisition time, which is given by the number of excitations (sub-apertures), the time it takes for the ultrasonic wave to propagate through the 3 media (2 media inside the roller-probe + inspected WAAM) or a time of the wave decay below to a sufficiently low level after which it no longer interacts with newly emitted wave and its reception. Since the material properties and the wave propagation time of flights is constant, the number of excitations and receptions can be reduced to increase the frame rate. Therefore, employing the VSA acquisition offers a significant advantage over the conventional FMC data acquisition owing to the reduced number of excitations required in the VSA. During the experimental work, the acquisition speed of the VSA was observed to be almost twice the speed of the FMC data acquisition. Furthermore, the VSA frame data size of 13.3 MB was achieved, which is a reduction of almost 37% as compared to the FMC frame size of 21.3 MB. The data in this work were stored in .mat file format.

In this work, the data was acquired using a program developed within the LabVIEW environment. During the experiment, the frame rates of 3.1 Hz and 1.6 Hz were achieved by the VSA and the FMC, respectively. Therefore, in an example WAAM wall inspection scenario where the sample is 2 meters long and post-deposition robotic inspection is carried out using a stable scanning speed of 10 mm/s, the VSA technique would enable the system to collect almost twice as the number of frames as collected by the FMC during the inspection, summarized in Table 5.6. This also implied that an increased frame density could be achieved through VSA while using the same scan speed, which is critical in terms of enhancing the detection probability.

Table 5.5 Comparison of inspection parameters achieved by VSA and FMC

Method	***Frames/WAAM at 10 mm/s***	***Frames/mm***
VSA	620	6.2
FMC	320	3.2

To realize the largest inspection increment size (resolution) required during an automated scan and yet sufficiently fine to not skip/lose any subsurface defects, a simulation, presented in Figure 5.14, was conducted to show the width of the ultrasound beam transmitted into the WAAM. The beam width was measured using the 6 dB drop method [105] from the maximum beam amplitude of 8.4 mm for the roller-probe configuration during the inspection of titanium WAAM (simulation parameters explained in section 5.3.2). This focal width indicated the longest allowable distance between two consecutive frames that would have still provided full coverage of the WAAM interior with an ultrasound beam during the robotic scan. To maintain a frame density of approximately 4 mm, considering a sufficient overlap of 50 percent, Table 5.7 showed a possibility to double the inspection speed as compared to FMC data acquisition, where the inspection speed would be also significantly reduced to almost half as well. This improvement reaching close to 50 % in scanning speed could result in a considerably reduced time of inspection and therefore, simplified NDT integration into the built process.

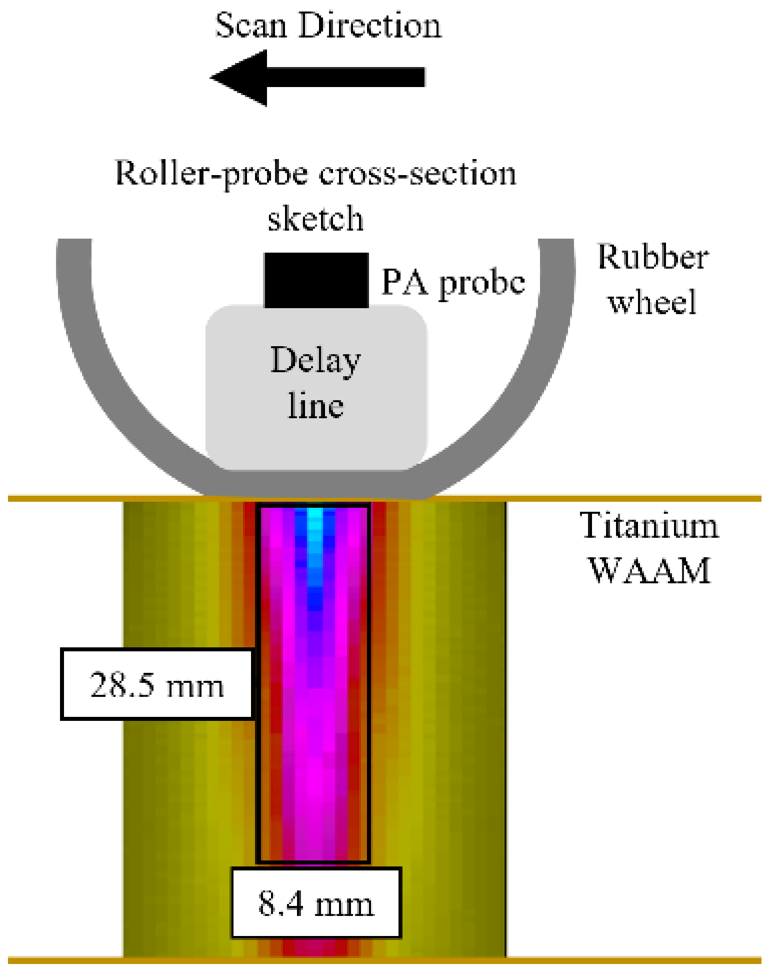

Figure 5.14 Simulation of the beam profile in inspection travel direction, providing information about the beam coverage

In this chapter, the imaging stage was integrated and implemented in MATLAB 2020a. The processing time was evaluated on setup with two Intel Xeon 6482R processors with a clock speed of 3 GHz and 192 GB of Random-Access Memory. The elapsed time for the SAFT algorithm to estimate the surface contour was 1.8 seconds since ray-tracing and ToF's were pre-loaded into the system. The full adaptive TFM algorithm for both VSA-TFM and FMC-TFM was measured to be 131 seconds.

Table 5.6 Comparison of inspection parameters achieved by VSA and FMC

Method	***Max. scanning speed (mm/s)***	***Time of Inspection (seconds)***
VSA	12.4	161.3
FMC	6.4	312.5

5.5. Summary of the Chapter

This chapter presented an adaptation and deployment of a raw data acquisition called the virtual source aperture technique, evaluated with a post-processing algorithm package based on SAFT surface reconstruction and three-layer adaptive TFM imaging for a dry coupled roller-probe inspection of as-built WAAM components.

The applicability of the VSA was first evaluated by simulation and experimental validation of a typical inspection performed on a custom-designed Ti-6Al-4V calibration WAAM block. The comparison of simulation and experiment confirmed the increase in energy levels enabled by VSA to be at least 0.8 dB and 1.5 dB respectively within the WAAM component with comparable SNR levels.

Furthermore, the experimental mock inspection of an as-built WAAM sample through its non-planar surface was conducted to demonstrate the potential to reconstruct the surface using VSA and subsequently, compute a precise interior image of the wall. The experimental work was conducted on a Ti-6Al-4V WAAM wall with three 1.0 mm SDH reflectors.

During the inspection, an accurate VSA-SAFT surface estimation was obtained, in a close match to FMC-SAFT-based reconstruction. Comparing the derived surface profile with that measured by a laser scanner demonstrated an accuracy better than the required threshold of $\lambda/4$.

Using an obtained surface profile, the interior image was computed, showing successfully detected SDH defects with an increased signal strength of up to 6.42 dB as compared to the FMC-based TFM image. While comparable overall SNR levels were achieved, the VSA-TFM image achieved significantly higher SNR for the defect on the right of the center as compared to its FMC counterpart.

Lastly, it can be concluded that the VSA in combination with the SAFT-TFM imaging package offers the potential to reduce the data size by 37.5 %, due to a markedly lower number of transmissions, while also increasing the potential inspection speed by 48% when compared to the previously reported FMC-TFM approach. While the imaging performance is similar, the advantage of the speed and data size reduction can simplify the integration of the inspection during the build process.

Chapter 6

Conclusions and Future Work

Chapters 3, 4 and 5 introduced novel research in the field of automated ultrasound NDE of as-built WAAM components. In this chapter, suggested future steps, with a relationship to the presented work, are introduced and discussed to further enhance this research area of in-process NDE of metal additive manufacture. Finally, the general overview is given summarizing the accomplishments presented in this thesis.

6.1. Suggested Future work

6.1.1. Multi-Layer Ultrasonic Imaging of As-Built Wire + Arc Additive Manufactured Components – Chapter 3

For the in-situ deployment of this SAFT-TFM algorithm package, the key future goal is to investigate the effect of the temperature gradients within the deposited WAAM component on ultrasonic wave propagation (velocity, refraction, and attenuation). This will provide a basis on which the subsequent development of adaptive compensation algorithms can be carried out, further enhancing the defect detection accuracy and sensitivity. The velocity calibration and compensation for the anisotropic materials are also sought to be developed, allowing for precise ray-tracing within the components.

Moreover, the surface obtained from individual frames can be linked together to enable 3-dimensional reconstruction which can be used for ray-tracing enabled to achieve higher imaging and ToF accuracy.

In this thesis, the speed of the algorithm was not the prime concern. Hence, the algorithm package was not yet optimized for a high frame rate. To achieve high-speed computation of TFM images, further modifications must be investigated to employ the computing power of Graphics Processing Units (GPU). This work will, however, also require a programming language migration to one suitable for such a purpose. Optimizing for GPU usage can offer the advantage of splitting the execution on a much higher number of cores compared to a low number of CPU cores, which is not possible within the MATLAB environment.

6.1.2. Multi-Robot Cell for Wire + Arc Additive Manufacture and Sensor-enabled In-process Ultrasound Non-Destructive Evaluation

The suggested future step in the in-process NDE of WAAM is the improvement of the transduction during automated deployment of the roller-probe on WAAM. Although the system was proven effective to detect a tungsten tube reflector as small as 1 mm, placed in longitudinal and traverse direction, more constant levels of SNRs during the inspection of the same sized reflector will be sought to be achieved during scanning to enable the establishment of a flaw sizing calibration procedure. This can be achieved by further utilizing the robot’s ability to maintain orientation normal to the surface in cooperation with torque data provided by the FT sensor. Moreover, alternative tire materials should be investigated to improve compliance with the highly complex surface of WAAM.

The roller-probe deployment should be also investigated and evaluated in various in-process NDE scenarios such as I) during inspection of geometrically complex WAAM sections (curves, bends, or T-junctions), where the roller-probe is challenged to maintain orientation normal to the WAAM surface direction, and II) investigate complex co-operation between WAAM deposition robot and NDE robot which can enable the deployment of the NDE while the active deposition is in progress elsewhere.

6.2.3. Increasing the Speed of Automated Ultrasonic Inspection of As-built WAAM Components by the Adoption of Virtual Source Aperture - Chapter 5

Future research should seek to aim to increase the SNR of the detected defects by employing advanced techniques such as coded excitation. The suggested research direction involves also investigating and adopting plane-wave imaging. Smart adaptive virtual source beamforming could also enable steering of the beam to the desired location within the built volume.

Further, the speed of the inspection can be enhanced with the use of additional hardware, such as laser scanners following the torch, to enable the pre-computation of ray-tracing and ToFs which can then be fed into the data acquisition/beamforming process for more rapid imaging.

6.2. General Overview

In the fast-growing sector of smart manufacturing, there is a high demand for the integration of quality assurance into the production chain. Convectional NDE has been mainly conducted in a separate stage of metal AM parts deposition, after the full completion and often after the post-processing of the components. This could significantly limit the possibility of cost and time-efficient repair and therefore negatively impact the overall cost-effectiveness of the process.

This thesis intended to address these limitations and has contributed to the field of automated ultrasonic inspection of metal AM components, especially WAAM.

The first novelty was achieved by exploring the possibility to utilize advanced ultrasound data acquisition and ultrasound post-processing imaging techniques developed for the novel high-temperature dry-coupled in-process ultrasound roller-probe inspection of WAAM components.

When considering the deployment of an ultrasound NDE on the as-built and hot component of WAAM, the challenge of conforming the probe to the surface of the component and the ability to sustain the heat must be overcome. This challenge was tackled by developing novel ultrasound phased array transducer roller-probes capable of withstanding this hostile condition by dry-coupling to the surface of WAAM using high-temperature resistant polymers and solid core delay lines. However, the issue of ultrasound wave refraction at two interfaces with one unpredictably curved was created. The work addressing this challenge was introduced and presented in Chapter 3, which showed the capability to detect fragmented LoF defects as small as 5 × 0.5 × 0.5 mm (W × L × H) within the built volume of the Ti-6Al-4V WAAM component.

A key advancement, opening a possibility to accurately detect defects within the volume of the WAAM components, was achieved by the development of an ultrasound FMC data post-processing package based on SAFT surface finding and a 3-layer adaptive TFM algorithm.

Further, to efficiently deploy such an ultrasonic roller-probe NDE approach, where the coupling to an unpredictably rough surface condition is necessary, a sufficient sensor-enabled intelligent robotic system is required. Such as system, however, not only addresses the problem of NDE integration but directly responds to the needs of industry 4.0. The work to address this was introduced and presented in Chapter 4, which showed the WAAM & ultrasound NDE cell and its capability to detect embedded flaws with a diameter of 1 mm.

While the WAAM process was driven by its default path planning program, the NDE was enabled via a robot kinematics package with integrated force-torque sensing capabilities enabling smooth rolling on WAAM at a constant force. Therefore, for the first time, the dry coupled roller-probe was deployed, within a process dwell time set for inter-layer cooling, on a hot and as-built Ti-6Al-4V WAAM component with artificially embedded tungsten reflectors.

To further advance the benefits of the automated and in-process roller-probe inspection approach, the challenges of I) large data size, II) low inspection speed, and III) lower ultrasound energy levels at reception, were sought to be tackled. This was accomplished by taking advantage of a phased array transducer and its large number of elements. Using an adopted VSA data acquisition technique, the work presented in Chapter 5, showed the capability to detect 1 mm SDH defects. While the imaging performance was comparable to convectional FMC-based inspection, the data size was reduced significantly while the potential maximum inspection speed was almost doubled. An increase in retrieved energy from the interior of the sample was observed as well.

To summarize this research, a solid foundation to unlock autonomous in-process NDE of WAAM has been laid. With the addition of the proposed future goals, an automated quality assured manufacturing of high-value components can be achieved, directly responding to the demands from the ongoing industrial revolution (4.0) and sectors such as aerospace, nuclear or transportation.

References

[1] "Metal Additive Manufacture Market." https://additive-manufacturing-report.com/additive-manufacturing-market/ (accessed 17/01/2022.

[2] P. Zawadzki and K. Żywicki, "Smart product design and production control for effective mass customization in the Industry 4.0 concept," *Management and production engineering review*, 2016.

[3] T. DebRoy *et al.*, "Scientific, technological and economic issues in metal printing and their solutions," *Nature materials*, vol. 18, no. 10, pp. 1026-1032, 2019.

[4] S. W. Williams, F. Martina, A. C. Addison, J. Ding, G. Pardal, and P. Colegrove, "Wire+ arc additive manufacturing," *Materials Science and Technology*, vol. 32, no. 7, pp. 641-647, 2016.

[5] P. Colegrove, A. McAndrew, J. Ding, F. Martina, P. Kurzynski, and S. Williams, "System architectures for large scale wire+ arc Additive Manufacture," in *10th International Conference on Trends in Welding Research*, 2016.

[6] X. Xu, J. Ding, S. Ganguly, C. Diao, and S. Williams, "Preliminary investigation of building strategies of maraging steel bulk material using wire+ arc additive manufacture," *J Mater Eng Perform*, vol. 28, no. 2, pp. 594-600, 2019.

[7] X. Xu, J. Ding, S. Ganguly, C. Diao, and S. Williams, "Oxide accumulation effects on wire+ arc layer-by-layer additive manufacture process," *J Mater Process Tech*, vol. 252, pp. 739-750, 2018.

[8] B. Wu *et al.*, "A review of the wire arc additive manufacturing of metals: properties, defects and quality improvement," *Journal of Manufacturing Processes*, vol. 35, pp. 127-139, 2018.

[9] P. J. Shull, *Nondestructive evaluation: theory, techniques, and applications*. CRC press, 2002.

[10] A. Lopez, R. Bacelar, I. Pires, T. G. Santos, J. P. Sousa, and L. Quintino, "Non-destructive testing application of radiography and ultrasound for wire and arc additive manufacturing," *Additive Manufacturing*, vol. 21, pp. 298-306, 2018.

[11] A. B. Lopez, J. Santos, J. P. Sousa, T. G. Santos, and L. Quintino, "Phased Array Ultrasonic Inspection of Metal Additive Manufacturing Parts," *Journal of Nondestructive Evaluation*, vol. 38, no. 3, p. 62, 2019.

[12] E. Mohseni *et al.*, "Ultrasonic phased array inspection of wire plus arc additive manufactured (WAAM) titanium samples," in *58th Annual British Conference on Non-Destructive Testing*, 2019.

[13] Y. Javadi *et al.*, "Continuous monitoring of an intentionally-manufactured crack using an automated welding and in-process inspection system," *Mater Design*, p. 108655, 2020.

[14] N. Knezović and B. Dolšak, "In-process non-destructive ultrasonic testing application during wire plus arc additive manufacturing," *Advances in Production Engineering & Management*, vol. 13, no. 2, pp. 158-168, 2018.

[15] G. Dobie, R. Summan, S. G. Pierce, W. Galbraith, and G. Hayward, "A noncontact ultrasonic platform for structural inspection," *IEEE Sensors Journal*, vol. 11, no. 10, pp. 2458-2468, 2011.

[16] M. Vasilev *et al.*, "Sensor-enabled multi-robot system for automated welding and in-process ultrasonic nde," *Sensors*, vol. 21, no. 15, p. 5077, 2021.

[17] Y. Javadi *et al.*, "In-process calibration of a non-destructive testing system used for in-process inspection of multi-pass welding," *Mater Design*, vol. 195, p. 108981, 2020.

[18] Olympus-ims.com. "Ultrasonic phased array wedge for inspecting high-temperature parts up to 150°C." Olympus-ims.com. https://www.olympus-ims.com/en/applications/ultrasonic-phased-array-wedge-for-inspecting-high-temperature-parts-up-to-150c/#:~:text=As%20phased%20array%20probes%20heat,temperature%20of%2060%20%C2%B0C. (accessed 16/11/2020, 2020).

[19] I. O. f. Standardization, *Additive Manufacturing: General: Principles: Terminology*. ISO, 2015.

[20] A. Paolini, S. Kollmannsberger, and E. Rank, "Additive manufacturing in construction: a review on processes, applications, and digital planning methods, Addit. Manuf. 30 (2019) 100894," ed, 2019.

[21] I. Gibson, D. Rosen, and B. Stucker, "Powder bed fusion processes," in *Additive manufacturing technologies*: Springer, 2015, pp. 107-145.

[22] D. Herzog, V. Seyda, E. Wycisk, and C. Emmelmann, "Additive manufacturing of metals," *Acta Mater,* vol. 117, pp. 371-392, 2016.

[23] S. Sun, M. Brandt, and M. Easton, "Powder bed fusion processes: An overview," *Laser Additive Manufacturing,* pp. 55-77, 2017.

[24] D.-G. Ahn, "Directed energy deposition (DED) process: State of the art," *International Journal of Precision Engineering and Manufacturing-Green Technology,* vol. 8, no. 2, pp. 703-742, 2021.

[25] I. Gibson, D. Rosen, and B. Stucker, "Directed energy deposition processes," in *Additive manufacturing technologies*: Springer, 2015, pp. 245-268.

[26] K. Derekar, "A review of wire arc additive manufacturing and advances in wire arc additive manufacturing of aluminium," *Materials science and technology,* vol. 34, no. 8, pp. 895-916, 2018.

[27] J. Z. Li, M. R. Alkahari, N. A. B. Rosli, R. Hasan, M. N. Sudin, and F. R. Ramli, "Review of wire arc additive manufacturing for 3D metal printing," *International Journal of Automation Technology,* vol. 13, no. 3, pp. 346-353, 2019.

[28] F. Martina, J. Mehnen, S. W. Williams, P. Colegrove, and F. Wang, "Investigation of the benefits of plasma deposition for the additive layer manufacture of Ti–6Al–4V," *J Mater Process Tech*, vol. 212, no. 6, pp. 1377-1386, 2012.

[29] C. Wu, L. Wang, W. Ren, and X. Zhang, "Plasma arc welding: Process, sensing, control and modeling," *Journal of manufacturing processes*, vol. 16, no. 1, pp. 74-85, 2014.

[30] A. Caballero, J. Ding, Y. Bandari, and S. Williams, "Oxidation of Ti-6Al-4V during wire and arc additive manufacture," *3D Printing and Additive Manufacturing*, vol. 6, no. 2, pp. 91-98, 2019.

[31] J. Ding, P. Colegrove, F. Martina, S. Williams, R. Wiktorowicz, and M. Palt, "Development of a laminar flow local shielding device for wire+ arc additive manufacture," *J Mater Process Tech*, vol. 226, pp. 99-105, 2015.

[32] G. A. LEVCUN and C. S. MAHENDRA, "Computed Radiography in the Pacific Northwest: Benefits, Drawbacks, and Requirements," *AMMTIAC Quarterly*, pp. 11-14, 2007.

[33] N. Kourra *et al.*, "Computed tomography metrological examination of additive manufactured acetabular hip prosthesis cups," *Additive Manufacturing*, vol. 22, pp. 146-152, 2018.

[34] J. Mireles, S. Ridwan, P. A. Morton, A. Hinojos, and R. B. Wicker, "Analysis and correction of defects within parts fabricated using powder bed fusion technology," *Surface Topography: Metrology and Properties*, vol. 3, no. 3, p. 034002, 2015.

[35] S. Naito, S. Yamamoto, and S. Yamamoto, "Novel X-ray backscatter technique for detecting crack below deposit," in *7th International Conference on NDE in Relation to Structural Integrity for Nuclear and Pressurized Components*, 2010.

[36] J. García-Martín, J. Gómez-Gil, and E. Vázquez-Sánchez, "Non-destructive techniques based on eddy current testing," *Sensors*, vol. 11, no. 3, pp. 2525-2565, 2011.

[37] J. B. Bento, A. Lopez, I. Pires, L. Quintino, and T. G. Santos, "Non-destructive testing for wire+ arc additive manufacturing of aluminium parts," *Additive Manufacturing*, vol. 29, p. 100782, 2019.

[38] W. Du, Q. Bai, Y. Wang, and B. Zhang, "Eddy current detection of subsurface defects for additive/subtractive hybrid manufacturing," *The International Journal of Advanced Manufacturing Technology*, vol. 95, no. 9, pp. 3185-3195, 2018.

[39] G. Bertotti, "Physical interpretation of eddy current losses in ferromagnetic materials. I. Theoretical considerations," *Journal of applied Physics*, vol. 57, no. 6, pp. 2110-2117, 1985.

[40] X. Chen *et al.*, "A review on wire-arc additive manufacturing: typical defects, detection approaches, and multisensor data fusion-based model," *The International Journal of Advanced Manufacturing Technology*, vol. 117, no. 3, pp. 707-727, 2021.

[41] Y. Gao *et al.*, "Towards superior fatigue crack growth resistance of TC4-DT alloy by in-situ rolled wire-arc additive manufacturing," *Journal of Materials Research and Technology,* vol. 15, pp. 1395-1407, 2021.

[42] E. D'Accardi, S. Altenburg, C. Maierhofer, D. Palumbo, and U. Galietti, "Detection of Typical Metal Additive Manufacturing Defects by the Application of Thermographic Techniques," *Multidisciplinary Digital Publishing Institute Proceedings,* vol. 27, no. 1, p. 24, 2019.

[43] A. Lopez, R. Bacelar, I. Pires, T. Santos, and L. Quintino, "Mapping of non-destructive techniques for inspection of wire and arc additive manufacturing," in *Proceedings of the 7th International Conference on Mechanics and Materials in Design, Portugal*, 2017, pp. 1829-1844.

[44] Y. Javadi *et al.*, "Intentional weld defect process: from manufacturing by robotic welding machine to inspection using TFM phased array," in *AIP Conference Proceedings*, 2019, vol. 2102, no. 1: AIP Publishing LLC, p. 040011.

[45] M. Willcox and G. Downes, "A brief description of NDT techniques," *Toronto: NDT Equipment Limited,* 2003.

[46] Y. Javadi *et al.*, "In-process inspection of multi-pass robotic welding," *Review of Progress in Quantitative Nondestructive Evaluation,* 2019.

[47] D. Pieris *et al.*, "Laser Induced Phased Arrays (LIPA) to detect nested features in additively manufactured components," *Mater Design,* vol. 187, p. 108412, 2020.

[48] Y. Zeng, X. Wang, X. Qin, L. Hua, and M. Xu, "Laser Ultrasonic inspection of a Wire+ Arc Additive Manufactured (WAAM) sample with artificial defects," *Ultrasonics*, p. 106273, 2020.

[49] C. Bakre, M. Hassanian, and C. Lissenden, "Influence of surface roughness from additive manufacturing on laser ultrasonics measurements," in *AIP Conference Proceedings*, 2019, vol. 2102, no. 1: AIP Publishing LLC, p. 020009.

[50] D. Chimenti, "Review of air-coupled ultrasonic materials characterization," *Ultrasonics*, vol. 54, no. 7, pp. 1804-1816, 2014.

[51] J. Tomlinson, A. Wagg, and M. Whittle, "Ultrasonic inspection of austenitic welds," 1980.

[52] E. Mohseni *et al.*, "Ultrasonic phased array inspection of wire plus arc additive manufactured (WAAM) titanium samples," in *58th Annual British Conference on Non-Destructive Testing*, 2019.

[53] Y. Javadi *et al.*, "Ultrasonic phased array inspection of a Wire+ Arc Additive Manufactured (WAAM) sample with intentionally embedded defects," *Additive Manufacturing*, vol. 29, p. 100806, 2019.

[54] J. A. Jensen, "Medical ultrasound imaging," *Progress in biophysics and molecular biology*, vol. 93, no. 1-3, pp. 153-165, 2007.

[55] V. Paidi, H. Fleyeh, J. Håkansson, and R. G. Nyberg, "Smart parking sensors, technologies and applications for open parking lots: a review," *IET Intelligent Transport Systems*, vol. 12, no. 8, pp. 735-741, 2018.

[56] K. S. Suslick and G. J. Price, "Applications of ultrasound to materials chemistry," *Annual Review of Materials Science,* vol. 29, no. 1, pp. 295-326, 1999.

[57] S. Iyer, S. K. Sinha, M. K. Pedrick, and B. R. Tittmann, "Evaluation of ultrasonic inspection and imaging systems for concrete pipes," *Automation in construction,* vol. 22, pp. 149-164, 2012.

[58] E. Mohseni *et al.,* "A high temperature phased array ultrasonic roller probe designed for dry-coupled in-process inspection of wire+ arc additive manufacturing," in *47th Annual Review of Progress in Quantitative Nondestructive Evaluation*, 2020.

[59] A. Ehrard, H. Wuestenberg, E. Schulz, and E. Mundry, "Practical applications of longitudinal creeping waves in NDT with ultrasound and practical experiences with creeping wave probes," CEA Centre d'Etudes Nucleaires de Saclay, 1982.

[60] D. Ensminger, *Ultrasonics: fundamentals, technology, applications, revised and expanded*. CRC Press, 1988.

[61] A. McNab and M. Campbell, "Ultrasonic phased arrays for nondestructive testing," *NDT international,* vol. 20, no. 6, pp. 333-337, 1987.

[62] J. Cruza, J. Camacho, and C. Fritsch, "Plane-wave phase-coherence imaging for NDE," *NDT & E International,* vol. 87, pp. 31-37, 2017.

[63] S. Cochran, "Ultrasonics Part 12. Fundamentals of ultrasonic phased arrays," *Insight-Non-Destructive Testing and Condition Monitoring,* vol. 48, no. 4, pp. 212-217, 2006.

[64] C. Mineo *et al.*, "Flexible integration of robotics, ultrasonics and metrology for the inspection of aerospace components," in *AIP conference proceedings*, 2017, vol. 1806, no. 1: AIP Publishing LLC, p. 020026.

[65] C. Holmes, B. W. Drinkwater, and P. D. Wilcox, "Post-processing of the full matrix of ultrasonic transmit–receive array data for non-destructive evaluation," *NDT & e International*, vol. 38, no. 8, pp. 701-711, 2005.

[66] C. Holmes, B. Drinkwater, and P. Wilcox, "The post-processing of ultrasonic array data using the total focusing method," *Insight-Non-Destructive Testing and Condition Monitoring*, vol. 46, no. 11, pp. 677-680, 2004.

[67] W. Kerr, S. Pierce, and P. Rowe, "Investigation of synthetic aperture methods in ultrasound surface imaging using elementary surface types," *Ultrasonics*, vol. 72, pp. 165-176, 2016.

[68] C. H. Frazier and W. D. O'Brien, "Synthetic aperture techniques with a virtual source element," *IEEE transactions on ultrasonics, ferroelectrics, and frequency control*, vol. 45, no. 1, pp. 196-207, 1998.

[69] E. Cuevas, M. Lopez, M. García, and K. R. Ibérica, "Ultrasonic techniques and industrial robots: natural evolution of inspection systems," in *4th International Symposium on NDT in Aerospace, Berlin (Germany)*, 2012.

[70] K. AG, "https://www.kuka.com/-/media/kukadownloads/imported/9cb8e311bfd744b4b0eab25ca883f6d3/kuka_robotics_low_payloads.pdf?rev=cbf117123ca142dda4c7abe9ba0a3e64&hash=2EC50

752C478393CC7DD0E76F272BC59," 2018. [Online]. Available: https://www.kuka.com/-/media/kukadownloads/imported/9cb8e311bfd744b4b0eab25ca883f6d3/kuka_robotics_low_payloads.pdf?rev=cbf117123ca142dda4c7abe9ba0a3e64&hash=2EC50752C478393CC7DD0E76F272BC59.

[71] A. Chabot, N. Laroche, E. Carcreff, M. Rauch, and J.-Y. Hascoët, "Towards defect monitoring for metallic additive manufacturing components using phased array ultrasonic testing," *Journal of Intelligent Manufacturing*, pp. 1-11, 2019.

[72] X. Xiong, H. Zhang, and G. Wang, "Metal direct prototyping by using hybrid plasma deposition and milling," *J Mater Process Tech*, vol. 209, no. 1, pp. 124-130, 2009.

[73] H. Lockett, J. Ding, S. Williams, and F. Martina, "Design for Wire+ Arc Additive Manufacture: design rules and build orientation selection," *Journal of Engineering Design*, vol. 28, no. 7-9, pp. 568-598, 2017.

[74] F. Hagglund, M. Robson, M. J. Troughton, W. Spicer, and I. R. Pinson, "A novel phased array ultrasonic testing (PAUT) system for on-site inspection of welded joints in plastic pipes," in *Proceedings of the 11th European Conference on Non-Destructive Testing (ECNDT), Prague, Czech Republic*, 2014, pp. 6-10.

[75] T. Stratoudaki, Y. Javadi, W. Kerr, P. D. Wilcox, D. Pieris, and M. Clark, "Laser induced phased arrays for remote ultrasonic imaging of additive manufactured

components," in *57th Annual Conference of the British Institute of Non-Destructive Testing, NDT 2018*, 2018, pp. 174-182.

[76] D. Lines *et al.*, "Using coded excitation to maintain signal to noise for FMC+ TFM on attenuating materials," in *2019 IEEE International Ultrasonics Symposium (IUS)*, 2019: IEEE, pp. 635-638.

[77] B. Drinkwater, R. Dwyer-Joyce, and P. Cawley, "A study of the transmission of ultrasound across solid–rubber interfaces," *The Journal of the Acoustical Society of America,* vol. 101, no. 2, pp. 970-981, 1997.

[78] B. Drinkwater and P. Cawley, "AN ULTRASONIC WHEEL PROBE AL TERNA TIVE TO LIQUID COUPLING," 1994.

[79] C. Mineo *et al.*, "Fast ultrasonic phased array inspection of complex geometries delivered through robotic manipulators and high speed data acquisition instrumentation," in *2016 IEEE International Ultrasonics Symposium (IUS)*, 2016: IEEE, pp. 1-4.

[80] R. K. Vithanage *et al.*, "A phased array ultrasound roller probe for automated in-process/interpass inspection of multipass welds," *IEEE Transactions on Industrial Electronics,* 2020.

[81] C. Fan and B. W. Drinkwater, "Comparison between beamforming and super resolution imaging algorithms for non-destructive evaluation," in *AIP Conference Proceedings*, 2014, vol. 1581, no. 1: American Institute of Physics, pp. 171-178.

[82] X.-l. Han, W.-t. Wu, P. Li, and J. Lin, "Application of ultrasonic phased array total focusing method in weld inspection using an inclined wedge," in *Proceedings of the 2014 Symposium on Piezoelectricity, Acoustic Waves, and Device Applications*, 2014: IEEE, pp. 114-117.

[83] L. Le Jeune, S. Robert, P. Dumas, A. Membre, and C. Prada, "Adaptive ultrasonic imaging with the total focusing method for inspection of complex components immersed in water," in *AIP Conference proceedings*, 2015, vol. 1650, no. 1: American Institute of Physics, pp. 1037-1046.

[84] G. P.-A. Nicolas Badeau, Alain Le Duff. "Use of the Total Focusing Method with the Envelope Feature." https://www.olympus-ims.com/en/resources/white-papers/use-of-the-total-focusing-method-with-the-envelope-feature/ (accessed [accessed 9 April 2020.

[85] M. Parrilla, J. Brizuela, J. Camacho, A. Ibanez, P. Nevado, and C. Fritsch, "Dynamic focusing through arbitrary geometry interfaces," in *2008 IEEE Ultrasonics Symposium*, 2008: IEEE, pp. 1195-1198.

[86] "Compact laser scanner for automation & robotics." https://www.micro-epsilon.co.uk/2D_3D/laser-scanner/scanCONTROL-2600/ (accessed 11/02, 2021).

[87] R. Zimermann *et al.*, "Implementation of an ultrasonic total focusing method for inspection of unmachined wire+ arc additive manufacturing components through multiple interfaces," *47th Annual Review of Progress in Quantitative Nondestructive Evaluation*, 2020.

[88] P. Ciorau, J. Coulas, and T. Armitt, "A contribution to length sizing of weld flaws using conventional, PAUT and TOFD ultrasonic techniques," *NDT. net,* no. 11, 2011.

[89] M. Kaczmarek, B. Piwakowski, and R. Drelich, "Noncontact ultrasonic nondestructive techniques: state of the art and their use in civil engineering," *Journal of Infrastructure Systems,* vol. 23, no. 1, p. B4016003, 2017.

[90] "KUKA.RobotSensorInterface 4.0. 2018." https://www.kuka.com/en-gb/products/robotics-systems/software/system-software/kuka_systemsoftware (accessed 19/01/2022.

[91] "WAAMctrl." https://waam3d.com/software/control-suite (accessed 18/01/2022.

[92] "WAAMPlanner." https://waam3d.com/software/planner (accessed 17/01/2022.

[93] "“What is LabVIEW?”." https://www.ni.com/en-gb/shop/labview.html (accessed 17/01/2022.

[94] E. Aldalur, F. Veiga, A. Suárez, J. Bilbao, and A. Lamikiz, "High deposition wire arc additive manufacturing of mild steel: Strategies and heat input effect on microstructure and mechanical properties," *Journal of Manufacturing Processes,* vol. 58, pp. 615-626, 2020.

[95] P. A. Colegrove *et al.*, "Microstructure and residual stress improvement in wire and arc additively manufactured parts through high-pressure rolling," *J Mater Process Tech,* vol. 213, no. 10, pp. 1782-1791, 2013.

[96] Y. Javadi, M. Akhlaghi, and M. A. Najafabadi, "Using finite element and ultrasonic method to evaluate welding longitudinal residual stress through the thickness in austenitic stainless steel plates," *Mater Design,* vol. 45, pp. 628-642, 2013.

[97] L. Vázquez, N. Rodríguez, I. Rodríguez, E. Alberdi, and P. Álvarez, "Influence of interpass cooling conditions on microstructure and tensile properties of Ti-6Al-4V parts manufactured by WAAM," *Welding in the World,* vol. 64, no. 8, pp. 1377-1388, 2020.

[98] D. Lines *et al.*, "Modelling of echo amplitude fidelity for transducer bandwidth and TFM pixel resolution," in *47th Annual Review of Progress in Quantitative Nondestructive Evaluation*, 2020.

[99] E. Hoyle, M. Sutcliffe, P. Charlton, and J. Rees, "Virtual source aperture imaging with auto-focusing of unknown complex geometry through dual layered media," *NDT & E International,* vol. 98, pp. 55-62, 2018.

[100] E. Hoyle, M. Sutcliffe, P. Charlton, and J. Rees, "Virtual Source Aperture with Real Time Focussing of Known Geometry Through Dual Layered Media," in *BINDT 56th Annual Conference 3B5 (freely available on Researchgate)*, 2017.

[101] J. Camacho and J. F. Cruza, "Auto-focused virtual source imaging with arbitrarily shaped interfaces," *IEEE transactions on ultrasonics, ferroelectrics, and frequency control,* vol. 62, no. 11, pp. 1944-1956, 2015.

[102] R. E. Malkin, A. C. Franklin, R. L. Bevan, H. Kikura, and B. W. Drinkwater, "Surface reconstruction accuracy using ultrasonic arrays: Application to non-destructive testing," *NDT & E International*, vol. 96, pp. 26-34, 2018.

[103] P. DUBOIS, S. LONNE, F. JENSON, and S. MAHAUT, "Simulation of Ultrasonic, Eddy Current and Radiographic Techniques within the CIVA Software Platform," in *10th European Conference on Non–Destructive Testing, Moscow*, 2010.

[104] F. Foucher and P. Dubois, "Applications and recent evolutions of the CIVA Simulation Platform," in *18th World Conference on Nondestructive Testing*, 2012, pp. 16-20.

[105] X. Wang, J. He, W. Guo, and X. Guan, "Three-dimensional damage quantification of low velocity impact damage in thin composite plates using phased-array ultrasound," *Ultrasonics*, vol. 110, p. 106264, 2021.